

AD _____

Award Number: DAMD17-98-1-8156

TITLE: Energy- and Intensity-Modulated Electron Beam for Breast
Cancer

PRINCIPAL INVESTIGATOR: Chang Ming Ma, Ph.D.

CONTRACTING ORGANIZATION: Stanford University
Stanford, California 94305-5401

REPORT DATE: October 2000

TYPE OF REPORT: Annual

PREPARED FOR: U.S. Army Medical Research and Materiel Command
Fort Detrick, Maryland 21702-5012

DISTRIBUTION STATEMENT: Approved for public release;
Distribution unlimited

The views, opinions and/or findings contained in this report are those of the author(s) and should not be construed as an official Department of the Army position, policy or decision unless so designated by other documentation.

20010531 032

REPORT DOCUMENTATION PAGE			Form Approved OMB No. 074-0188	
Public reporting burden for this collection of information is estimated to average 1 hour per response, including the time for reviewing instructions, searching existing data sources, gathering and maintaining the data needed, and completing and reviewing this collection of information. Send comments regarding this burden estimate or any other aspect of this collection of information, including suggestions for reducing this burden to Washington Headquarters Services, Directorate for Information Operations and Reports, 1215 Jefferson Davis Highway, Suite 1204, Arlington, VA 22202-4302, and to the Office of Management and Budget, Paperwork Reduction Project (0704-0188), Washington, DC 20503				
1. AGENCY USE ONLY (Leave blank)	2. REPORT DATE October 2000	3. REPORT TYPE AND DATES COVERED Annual (01 Oct 99 - 30 Sep 00)		
4. TITLE AND SUBTITLE Energy-And Intensity-Modulated Electron Beams for Breast Cancer Treatment		5. FUNDING NUMBERS DAMD17-98-1-8156		
6. AUTHOR(S) Chang Ming Ma, Ph.D.				
7. PERFORMING ORGANIZATION NAME(S) AND ADDRESS(ES) Stanford University Stanford, California 94305 e-mail: cma@Reyes.stanford.edu		8. PERFORMING ORGANIZATION REPORT NUMBER		
9. SPONSORING / MONITORING AGENCY NAME(S) AND ADDRESS(ES) U.S. Army Medical Research and Materiel Command Fort Detrick, Maryland 21702-5012		10. SPONSORING / MONITORING AGENCY REPORT NUMBER		
11. SUPPLEMENTARY NOTES				
12a. DISTRIBUTION / AVAILABILITY STATEMENT Approved for public release distribution unlimited			12b. DISTRIBUTION CODE	
13. ABSTRACT (Maximum 200 Words) In this project, we investigate energy- and intensity-modulated radiotherapy (EIMRT) for breast cancer to deliver dose distributions that closely match the target volume and minimize the dose to critical normal structures. We have worked on the following tasks: (1) to characterize electron beams from Helium-filled accelerators for EIMRT, (2) to develop optimization algorithms for EIMRT using these electron beams, (3) to verify these optimized dose distributions using the Monte Carlo simulation technique, and (4) to compare the optimized dose plans obtained by EIMRT with conventional treatment plans and those obtained by photon intensity-modulated radiotherapy (IMRT). During the second year research, we have performed accurate Monte Carlo simulations of the electron beams in He-filled accelerators and also investigated the effect of magnetic field modulation. Our results demonstrated that electron beams could be modulated more effectively using an electron MLC and a 1.5 T magnetic field to deliver superior dose distributions for EIMRT. We have tested different algorithms for "Inverse treatment planning" to optimize breast treatment plans for EIMRT. The results confirmed that EIMRT is superior to photon IMRT and much more effective than conventional tangential photon treatments. Further studies will be performed to verify the dose plans for realistic patients. The outcome will determine whether EIMRT offers a significant advantage over conventional photon/electron treatment and over photon IMRT.				
14. SUBJECT TERMS Breast Cancer			15. NUMBER OF PAGES 105	
			16. PRICE CODE	
17. SECURITY CLASSIFICATION OF REPORT Unclassified	18. SECURITY CLASSIFICATION OF THIS PAGE Unclassified	19. SECURITY CLASSIFICATION OF ABSTRACT Unclassified	20. LIMITATION OF ABSTRACT Unlimited	

Table of Contents

COVER.....	1
STANDARD FORM (SF) 298	2
TABLE OF CONTENTS	3
INTRODUCTION.....	4
BODY.....	4
KEY RESEARCH ACCOMPLISHMENTS	11
REPORTABLE OUTCOMES	12
CONCLUSIONS.....	14
REFERENCES.....	15
APPENDICES.....	17
<i>List of Figures quoted in the body of text:</i>	17
<i>List of manuscripts submitted with this report:</i>	23

Introduction

This project is aimed at exploring energy- and intensity-modulated electron beams for breast cancer treatment to deliver optimized conformal radiotherapy dose distributions that closely match the target volume and minimize the dose to critical normal structures. We have proposed to work on the following tasks: (1) to characterize electron beams from Helium-filled accelerators, (2) to develop optimization algorithms for energy- and intensity-modulated radiotherapy (EIMRT) using these electron beams, (3) to verify these optimized dose distributions using the Monte Carlo simulation technique, and (4) to compare the optimized dose plans obtained by EIMRT with conventional treatment plans and those obtained by photon intensity-modulated radiotherapy (IMRT).

Body

Although photon beams have been an effective modality for breast cancer treatment in radiation therapy the following problems (or potential areas of improvement) remain: (1) the inclusion of the lung and sometimes of a small volume of the heart in the high-dose volume due to tumor location, patient size or in the case of chest-wall treatments; (2) lower dose near the skin surface due to lack of electron build-up in a photon beam; and (3) high exit or scatter dose to the normal structures such as the lung and heart, and more importantly the contralateral breast, which may be a major cause for the occurrence of secondary cancer in the contralateral breast for women under the age of 45.

Recent development of computer-controlled medical linear accelerators along with improved treatment planning techniques, may provide new solutions in the delivery and control of external beam radiation through beam-intensity modulation¹⁻⁹. It is expected that using photon IMRT, the problem (1) above may be significantly improved but (2) will remain and (3) may become more serious as treatment time increases with the number of fields used (increased leakage or scattering dose). With modulated electron beams¹⁰⁻¹⁵, on the other hand, problem (1) may also be significantly improved and problems (2) and (3) can be completely eliminated due to the nature of electron beams.

In this project we proposed to study He-filled accelerators equipped with computer-controlled multi-leaf collimators and the Monte Carlo treatment planning technique for energy- and intensity-modulated electron beams for breast cancer to significantly improve the dose uniformity in the target volume, to

exclude the lung and heart from the high or moderate dose volume and to eliminate the scatter dose to the lung, the heart and the contralateral breast to reduce complications and late effects associated with breast cancer radiotherapy. The purpose of this study is to determine the degree of feasibility of using electron EIMRT to improve breast cancer treatment.

This project has 4 specific aims: (1) To perform Monte Carlo beam simulation; (2) To develop an optimization algorithm for EIMCRT; (3) To perform Monte Carlo dose verifications; and (4) To evaluate the optimized treatment plans.

We report on the research accomplishments associated with the tasks outlined in the approved "Statement of Work" below for our research between Oct. 1, 1999 and Sept. 30, 2000:

1. Install optimization software for clinical treatment planning system

We have developed a software interface called MCCALC to perform treatment planning optimization for clinical applications. The interface provides a graphics user interface (GUI) for the user to input optimization parameters and to acquire patient CT and contour information from a clinical treatment planning system (FOCUS, CMS, Inc). The computation of the beamlet dose distributions will be performed on a networked parallel computer system using the Monte Carlo method that we have established based on previous work¹⁶⁻²³ and the results will be used for the optimization process. The final intensity maps for each treatment field will be sent back to the clinical treatment planning system to beam delivery using custom made electron cutouts or using computer controlled electron multileaf collimator (eMLC). More detailed descriptions of the optimization algorithm and its implementation have been reported in a publication²⁴ and here we only describe briefly for completion.

A fast iterative optimization algorithm has been developed for electron beam optimization. The algorithm has been tested for both electron treatment planning optimization and photon beam optimization. The beamlet dimensions will be specified through the RTP module, based on the MLC leaf width. For the Varian MLC, the beamlet size will be variable between 10mm x 1mm and 10mm x 10mm. The beamlet profile will be different depending on the location of the beamlet (its slight spatial dependence on the accelerator head scatter, beam flatness and SSD variation). This will be automatically included when using the simulated phase-space data as source input. The MCDOSE code (see below) has been modified for the dose calculations in the patient. The beam incident

angles and patient CT data will be obtained from the RTP system. Each beamlet will require 1 – 10 million phase space photons depending on the dimensions of the beamlet. For a typical IMRT case with 9 gantry angles, the beamlet calculation (for 1 – 10 thousand beamlets) will be completed in a few minutes on the PC network after the variance reduction techniques are implemented.

The optimization procedure consists of the following two stages. First, the planner inputs the patient geometry and defines the treatment setup, such as the beam energy, number and orientations of beams, etc. The target volume and the critical structures are defined by the clinician. The planner also determines the size of the beamlets and number of dose or constraint points placed inside the target or critical structures, according to the patient anatomy, the required computation accuracy and the available computation time. Each broad beam is divided into beamlets and the dose and constraint points are uniformly and randomly placed inside the corresponding area. Then a reference monitor unit is assigned to each open rectangular beam and the dose deposition coefficients, which is defined as the dose contribution from a beamlet to a point, are calculated using MCDOSE and a conventional dose calculation model for comparison. Second, using the calculated dose deposition coefficients as input, the optimal intensity profile for each beam is achieved by the optimization process using an objective function. The results of the optimization process are the intensity profiles for the individual gantry angles (photon fields).

The results of the optimization calculation are the beam intensity maps at each gantry angle and then they can be used to generate leaf-setting sequences using a leaf sequencing algorithm. The final dose calculation will be performed again using MCDOSE. The effect associated with leaf and jaw movement will be accounted for in these calculations. We have been evaluating different leaf sequencing algorithms suitable for both “stop and shoot” and dynamic delivery. A new algorithm also synchronizes the leaf sequences to remove the “tongue and groove” effect. The results showed that the difference in the beam delivery time using a dynamic MLC between “stop and shoot” (including beam-off time for leaf movement) and dynamic delivery was clinically insignificant. We will install a leaf sequence algorithm for our project which uses the stop and shoot algorithm and also synchronizes the leaf’s movement to remove the “tongue and groove” effect. We will further work on other MLCs when the leaf sequence file format becomes available for operation with electron beams.

2. Investigate suitable objective functions for electron beam optimization

We have installed several objective functions for the optimizer used for electron beam EIMRT. We have selected a dose based objective function with soft constraints using dose volume histogram information. With this final selection decided, the optimization can be performed by using a dose based penalty function method and the center-of-mass method to minimize the augmented objective function. An improved conjugate vector method can also be used. For the target area, a quadratic form of objective function is specified. In addition, two target dose-uniformity constraints are used to ensure a uniform target dose distribution and to distinguish the clinical importance of cold and hot spots. For the critical structures, maximum-dose constraint and several levels of dose-volume constraints are assigned to each structure. For each objective function and constraint, an importance weight relative to the target objective function is assigned. All the constraints are mathematically transformed to the penalty functions of quadratic forms. The augmented objective function, which should be minimized, is a combination of the original objective functions and all penalty functions. The detailed methods have been reported in our publications²⁴ and the applications have been presented.

3. Verify electron EIMRT using EGS4/MCDOSE

We have developed a Monte Carlo EGS4¹⁶ user code MCDOSE²⁵ for electron beamlet and treatment plan dose calculations. Good agreement was achieved between the MCDOSE results and measurements²⁴⁻²⁸. Features of MCDOSE include a multiple-source model to reconstruct the beam phase space²⁶, inclusion of beam modifiers such as jaws, wedges, blocks, compensators and electron cutouts in the patient simulation, the implementation of several variance reduction techniques, and suitable for both conventional and intensity modulated radiation therapy (IMRT) treatment planing. Before MCDOSE is used reliably for dose calculation in clinic, it must be properly validated. The clinical validations for beam modifiers and dose calculation are presented. A comparison of the dose distribution with 45-degree wedge in a water phantom made between MCDOSE and EGS4/BEAM/DOSXYZ^{17,19,20} demonstrates that MCDOSE can give accurate result with wedge (Fig. 1). The dose distributions for a blocked 10x10 15MV photon beam in a water phantom are also compared between them. They agree very well. The comparison of Electron cutout factors between MCDOSE and measurements show a good agreement too. After applying variance reduction techniques in MCDOSE, the agreement of dose distributions in specifically designed inhomogeneous phantoms between MCDOSE and DOSXYZ is within the statistical uncertainty of 0.5% (Figs. 2-4).

All these results demonstrate that MCDOSE is accurate for routine dose calculation in radiotherapy treatment planning. The heterogeneity correction factors calculated by MCDOSE for layered-lung or layered-bone phantoms were consistent with results from measurement to within 1%. Due to the elegant variance reduction techniques, MCDOSE is also faster than EGS4/DOSXYZ²⁰ dose calculation by a factor of up to 30. A nine field IMRT planning can be done in 1-4 hours on a personal computer, including pre- and post-optimization dose calculation²⁵.

Initial schedule included the implementation of the PEREGRINE code system for this study. This was not done because of the delay of the commercial availability of the PEREGRINE system and the complication of the commercialization of the PEREGRINE system. The system has been exclusively licensed to the NOMOS, Corp. and it is no longer available as a free software. Instead, we have developed the MCDOSE system, which is based on the EGS4 system, which is free for research and education use. The MCDOSE code has been validated against the DOSXYZ code and proved to be equally accurate but about 20 times faster in computation speed. Therefore we have replaced the PEREGRINE software with MCDOSE for this study.

4. Verify photon IMRT using EGS4/MCDOSE

To verify the IMRT dose distributions calculated by the commercial treatment optimization system (CORVUS, NOMOS Corp.) we have modified the MCDOSE code to compute the dose from the leaf sequence files from the commercial system. First we performed calculations for a homogeneous PMMA phantom. Since CORVUS calculates dose to water while PMMA is not water equivalent it is important to establish a conversion scheme so that the measured ionization in the PMMA phantom can be converted to dose to water in order to verify the dose distributions computed by CORVUS. The Monte Carlo method computes both dose to water and dose to PMMA and the results can be used to study the energy fluence perturbation correction factor for the PMMA phantom (compared to a water phantom). IMRT plans have been computed using a water phantom and the PMMA phantom (all have the same dimensions) by CORVUS and Monte Carlo and the results were compared to measurements. For example, for a 9 field IMRT plan with 15 MV beams, the difference between the calculated and measured dose was 1.4% for the water phantom and 1.6% for the PMMA phantom. In general, the difference between the measured and calculated values was within 4% with an estimated measurement uncertainty of about 3% and Monte Carlo calculation uncertainty of 2%.

We have also computed dose distributions in heterogeneous PMMA phantoms with either lung or bone inserts. Figure 5 shows the dose distributions calculated by Monte Carlo for a 15 MV beam plan and Table I shows the measured and calculated dose values in the heterogeneous phantom for both 4 and 15 MV beam plans. The two plans were generated using our Monte Carlo based inverse planning system using the same parameters except for the beam energy. The Monte Carlo calculated values differed from the measured values by less than 1% for both 4 and 15 MV beam plans while the CORVUS values differed from the measured values by 1% for the 4 MV plan and 5% for the 15 MV plan. Similar agreement was obtained for other phantom configurations and beam energies. It is concluded that the Monte Carlo method is more accurate in predicting the dose in heterogeneous phantoms for IMRT dose verification and can be used to validate the dose distributions for IMRT as part of the QA procedure²⁷.

TABLE I
Dose at measurement point o as shown in Fig. 5.

Beam energy	Monte Carlo	CORVUS	Measurement
4 MV	2.177 Gy	2.201 Gy	2.177 Gy
15 MV	2.146 Gy	2.276 Gy	2.161 Gy

5. Investigate beam characteristics of electron beams modulated by magnetic fields

From our previous studies, it seems clear that an electron MLC will be able to deliver modulated electron fields accurately and therefore He-filled accelerator design may not be necessary (but will further improve the characteristics if implemented). We also set out to study other means to improve the electron dose distributions for modulated electron beam therapy for breast cancer. We have achieved some preliminary results and based on these results we have put out another DOD grant application to investigate the feasibility of using magnetic fields to modulate the beam at depth to reduce the dose to the distal organs such as the lung (see below). We have published a paper on this subject²⁸ and we briefly describe our results in the following paragraphs.

In this study, Monte Carlo simulations were employed to study the characteristics of the electron beams of a clinical linear accelerator in the presence of 1.5 and 3.0 T transverse magnetic fields and to assess the possibility of using magnetic fields in conjunction with modulated electron radiation therapy (MERT). The starting depth of the magnetic field was varied over several centimeters. It was found

that peak doses of as much as 2.7 times the surface dose could be achieved with a 1.5 T magnetic field. The magnetic field was shown to reduce the 80% and 20% dose drop-off distance by 50% to 80%. The distance between the 80% dose levels of the pseudo-Bragg peak induced by the magnetic field was found to be extremely narrow, generally less than 1 cm. However, by modulating the energy and intensity of the electron fields while simultaneously moving the magnetic field, a homogeneous dose distribution with low surface dose and a sharp dose fall-off was generated. Heterogeneities are shown to change the effective range of the electron beams, but not eliminate the advantages of a sharp depth-dose drop-off or high peak-to-surface dose ratio. This suggests the applicability of MERT with magnetic fields in heterogeneous media. The results of this study demonstrate the ability to use magnetic fields in MERT to produce highly desirable dose distributions.

Monte Carlo calculations were performed in which electrons were constrained to travel down the same initial axis, i.e. a pencil beam. These results clearly show the curvature of the electron beam dose distribution generally along the expected track. By superposition of many pencil beams along the lateral axis, it is clear that Bragg-peak-like dose peaks can be constructed. Narrow fields, defined by 3 x 3 cm² Cerrobend cutouts on 6 x 6 cm² applicators, were also simulated. What is apparent is that there is a significant shift of the dose peak off the central axis. These data are presented primarily as a demonstration of the effects of the magnetic field, i.e. the curvature of the beam and the formation of a dose peak. However, it is difficult to make any definitive statements regarding depth-dose distributions because of the lack of equilibrium, as discussed below.

Previous discussions of MERT have considered the use of fields with non-uniform energies and intensity distributions. Here, the technique is extended to the use of multiple magnetic field positions, i.e. a single port may include a 20 MeV field with a magnetic field beginning at 3.0 cm depth for a certain number of monitor units, and then another 20 MeV field with the magnetic field located at a depth of 5.0 cm delivered down the same axis, etc. It is instructive to compare this methodology with the more familiar method used in proton beam therapy. In that system, physical blocks of different thicknesses are used to shift the Bragg peak to different depths, and intensity modulation is provided by allowing the beam to dwell on a given modulator for a variable time period. In this case, the only difference is the means of moving the pseudo-Bragg peak, that is, by moving the magnetic field. Beam intensity is modulated simply by changing the number of monitor units delivered with the magnetic field at a given position. It was believed that, as with the proton beam, useful fields can be constructed

while maintaining the desirable depth-dose drop-off and low skin dose. We have used magnetic fields modulated electron beamlets for optimization and generate treatment plans for a realistic breast treatment plan. Figure 6 show the isodose distributions and the dose volume histogram data for the two plans, one with magnetic fields and the other without. It is very clear that magnetic field modulated electron beams show much better target conformity and normal tissue sparing. Based on these results, we have submitted an “IDEA” proposal to further investigate this novel method, and if funded we hope to improvement breast MERT significantly.

We can demonstrate how this works as follows. A simple one-dimensional optimization routine was utilized to generate two fields. In one case, a target profile was generated where the dose would rise linearly from 50% at the surface (relative to the maximum along the profiled axis) to 100% at 1.0 cm, then drop to zero at 6.2 cm. The optimized solution was solved numerically, and a linear combination of the 1.5 T fields was generated to match the target values in a least-squares sense. The results are shown in figure 7. Using the terminology from section 3.3, the width of the treatment region, 80/80, was found to be 5.0 cm, followed by a 80/20 drop-off of 0.77 cm. Between the depths of 1.6 cm and 5.6 cm, the dose was homogeneous to within 5 4% of the average dose. For more detailed descriptions of the magnetic field modulation please see reference [28].

Key Research Accomplishments

We have accomplished the following tasks:

- *Develop fast iterative optimization algorithms:* A fast iterative optimization algorithm has been developed for electron beam optimization. The algorithm has been tested for both electron treatment planning optimization and photon beam optimization.
- *Install and test different objective function for electron beam optimization:* We have installed several objective functions for the optimizer used for electron beam EIMRT. We have selected a dose based objective function with soft constraints using dose volume histogram information.
- *Study the characteristics of electron beam modulation using magnetic fields:* We have studied the characteristics of small field electron beams modulated by an electron MLC and 0.5-3.0 T magnetic fields. We have studied beam optimization using these modulated electron beamlets.

- *Verify electron beam IMRT using EGS4/MCDOSE:* We have developed an EGS4 user code called MCDOSE to calculate dose distribution for electron treatment planning. We have compared the dose distributions calculated using MCDOSE and those by DOSXYZ and achieved good agreement (within 1% of maximum dose).
- *Verify photon IMRT using EGS4/MCDOSE:* We have used MCDOSE to calculate dose distribution for photon IMRT treatment planning. We have compared the dose distributions calculated using MCDOSE and measurements and achieved good agreement (within 3% of maximum dose).

Reportable Outcomes

Peer-reviewed papers resulting from or supported in part by this grant:

- C.M. Ma, T. Pawlicki, M.C. Lee, S.B. Jiang, J.S. Li, J. Deng, E. Mok, B. Yi, G. Luxton and A.L. Boyer, Energy- and intensity-modulated electron beams for radiotherapy, *Phys. Med. Biol.* (2000) 45: 2293-2311
- J.S. Li, T. Pawlicki, J. Deng, S.B. Jiang, E. Mok and C.M. Ma, Validation of a Monte Carlo dose calculation tool for radiotherapy treatment planning, *Phys. Med. Biol.* (2000) 45: 2969-2985
- S.B. Jiang, A. Kapur and C.M. Ma, Electron beam modelling and commissioning for Monte Carlo treatment planning, *Med. Phys.* (2000) 27:180-191
- C.M. Ma, T. Pawlicki, S.B. Jiang, E. Mok, A. Kapur, L. Xing, L. Ma and A.L. Boyer, Monte Carlo verification of IMRT dose distributions from a commercial treatment planning optimization system, *Phys. Med. Biol.*, (2000) 45:2483-2495
- M. C. Lee and C.M. Ma, Monte Carlo characterization of clinical electron beams in transverse magnetic fields, *Phys. Med. Biol.* (2000) 45:2947-2967

Meeting abstracts resulting from or supported in part by this grant:

- C.M. Ma, JS Li, T Pawlicki, SB Jiang and J Deng, MCDOSE – a Monte Carlo dose calculation tool for radiation therapy treatment planning, *Proc. of the XIII International Conference on the Use of Computer in Radiation Therapy (ICCR)*, Eds: W Schlegel and T Bortfeld (Springer-Verlag, Heidelberg) 2000. 123-125
- C.M. Ma, T Pawlicki, MC Lee, SB Jiang, JS Li, J Deng, E Mok and AL Boyer, Modulated electron beams for treatment of breast cancer, Oral presentation at the XIII International Conference on the

Use of Computer in Radiation Therapy (ICCR), Heidelberg, Germany, May 22 - 25, 2000.
Proceedings to be published at the meeting.

- C.M. Ma, Monte Carlo methods in electron beams treatment planning, invited talk at the 41st Annual Meeting of the *American Association of Physicists in Medicine*, Nashville, TN, July 24-29, 1999. Med. Phys., 26(1999 AAPM Annual Meeting Program) 1999.
- J. Deng, S.B. Jiang, T. Pawlicki, J. Li and C.M. Ma, Electron beam commissioning for Monte Carlo dose calculation, ICCR 2000.
- C.M. Ma, T Pawlicki, SB Jiang, JS Li, Deng, D Findley, E Mok and AL Boyer, Implementation of a Monte Carlo dose calculation module in the FOCUS treatment planning system, CMS' FOCUS 2000 User's Symposium, St. Louis, MO, April 10-11, 2000.
- J. S. Li, T. Pawlicki, J. Deng, S.B. Jiang, A. Kapur, E. Mok and C.M. Ma, Clinical validation of a Monte Carlo dose calculation code for radiotherapy treatment planning (abstract), Med. Phys. 26, 1083
- J. S. Li, T. Pawlicki, J. Deng, S.B. Jiang and C.M. Ma, Simulation of Beam Modifiers for Monte Carlo Treatment Planning, submitted to ICCR 2000
- S. B. Jiang, A. Kapur, and C.M. Ma, Electron beam modeling and commissioning for Monte Carlo treatment planning, Med. Phys. 26, 1084 (1999) (abstract), AAPM Annual Meeting (Nashville).

Funding applied for based on work resulting from or supported in part by this grant:

1. US Army Breast Cancer Research Program: Postdoctoral Training Grant (PI: S.B. Jiang; Mentor: C.-M. Ma): Investigation of an electron MLC for energy and intensity modulated electron beam radiotherapy of breast cancer (awarded in 2000)
2. US Army Breast Cancer Research Program: Postdoctoral Training Grant (PI: T. Pawlicky; Mentor: C.-M. Ma): Effect of organ motion and patient setup uncertainty on the treatment of breast cancer with energy and intensity modulated electron beam radiotherapy (awarded in 2000)
3. US Army Breast Cancer Research Program: Predoctoral Training Grant (PI: Michael C. Lee; Mentor: C.-M. Ma): Beam verification for modulated electron radiation therapy treatment of breast cancer (submitted in 2000)
4. US Army Breast Cancer Research Program: Idea Grant (PI: C.-M. Ma): Electron beam modulation using magnetic fields for breast cancer treatment (submitted in 2000)

Conclusions

We have made significant progress during our second-year investigation. We have successfully performed the tasks scheduled in the "Statement of Work". We have developed optimization algorithms for comparisons of the optimized treatment plans with photon IMRT or electron EIMRT. We have installed and investigated suitable objective functions for electron beam optimization. We have verified electron EIMRT and photon IMRT using the EGS4/MCDOSE system and compared dose distributions for conventional treatment modalities. We also studied the effect of magnetic fields on modulation of electron beam profile and depth dose curves for EIMRT of breast cancer.

"So what?"

Our second year results have provided evidence to support the hypothesis of this proposal that by using computer-controlled, specially designed multi-leaf collimators for electron beams and the Monte Carlo treatment planning technique, energy- and intensity-modulated electron beams may be optimized to significantly improve the dose uniformity in the target volume, to reduce the dose to the critical structures nearby and therefore reduce the late effects associated with breast cancer radiotherapy. Further studies as scheduled in the "Statement of Work" are needed to investigate treatment plans for realistic breast cases generated using different beam modalities. We shall be able to finally determine the degree of feasibility of using electron EIMRT to improve breast cancer treatment.

References

1. R Boesecke, G Becker, K Alandt, *et al.* Modification of a three-dimensional treatment planning system for the use of multileaf collimators in conformation radiotherapy. *Radioth. and Oncol.* 21:261-268, 1991.
2. AL Boyer, TG Ochrn, CE Nyerick and TJ Waldron. Clinical dosimetry for implementation of a multileaf collimator. *Med. Phys.* 19:1255-1261, 1992.
3. A Brahme. Optimal setting of multileaf collimators in stationary beam radiation therapy. *Strahlenther. Onkol.* 164:343-350, 1988.
4. DJ Convery and M E Rosenbloom. The generation of intensity-modulated fields for conformal radiotherapy by dynamic collimation. *Phys. Med. Biol.*, 37:1359-1374, 1992.
5. WD Powlis, A Smith, E Cheng, *et al.* Initiation of multileaf collimator conformal radiation therapy. *Int. J. Radiat. Oncol. Biol. Phys.* 25:171-179, 1993.
6. JM Galvin, X Chen, and RM Smith. Combining multileaf fields to modulate fluence distributions. *Int. J. Radiat. Oncol. Biol. Phys.* 27:697-705, 1993.
7. T Bortfeld, A L Boyer, W Schlegel, D L Kahler, and T J Waldron. Realization and verification of three-dimensional conformation radiotherapy with modulated fields. *Int. J. Radiat. Oncol. Biol. Phys.* 30:899-908, 1994.
8. CX Yu, M J Symons, MN Du, AA Martinez, and J Wong. A method for implementing dynamic photon beam intensity modulation using independent jaws and multileaf collimator. *Phys. Med. Biol.*, 40:769-787, 1995.
9. R Mohan, X Wang, A Jackson, T Bortfeld, A L Boyer, G J Kutcher, S A Leibel, Z Fuks, and CC Ling. The potential and limitations of the inverse radiotherapy technique. *Radiotherapy and Oncology*, 32: 0232-248, 1994.
10. S Hyodynmaa, A Gastafsson and A Brame. Optimization of conformal electron beam therapy using energy- and fluence-modulated beams, *Med. Phys.*, 23: 659-666, 1996.
11. EP Lief, A Larsson and JL Humm. Electron dose profile shaping by modulation of a scanning elementary beam, *Med. Phys.*, 23: 33-44, 1996.
12. B Zackrisson and M Karlsson, Matching of electron beams for conformal therapy of target volumes at moderate depths, *Radiotherapy and Oncology*, 39: 261-270, 1996.
13. MG Karlsson, M Karlsson, CM Ma and A Satherberg, MLC-collimated electron beams – a Monte Carlo based optimization, *World Congress on Med. Phys.* (Nice, France) 1997 submitted
14. AAPM TG-21, A protocol for the determination of absorbed dose from high-energy photons and

- electrons, *Med. Phys.*, 10: 741, 1983.
15. C-M Ma, E Mok, A Kapur and D Findley, Improvement of small-field electron beam dosimetry by Monte Carlo simulations *Proc. XIIth ICCR* (Salt Lake City, Utah) 159-162, 1997.
 16. R. Nelson, H Hirayama and DWO Rogers. *The EGS4 code system*, Stanford Linear Accelerator Center Report SLAC-265 (SLAC, Stanford, CA) 1985.
 17. DWO Rogers, BA Faddegon, GX Ding, CM Ma, J Wei and TR Mackie, BEAM: a Monte Carlo code to simulate radiotherapy treatment units, *Med. Phys.* 22:503-525, 1995.
 18. A Kapur, C-M Ma, E Mok, D Findley, Characterization of small field electron beams for radiotherapy by Monte Carlo simulations, *Proc. XIIth ICCR* (Salt Lake City, Utah) 157-158, 1997.
 19. C-M Ma , BA Faddegon, DWO Rogers and TR Mackie, Accurate characterization of the Monte Carlo calculated electron beams for radiotherapy, *Med. Phys.*, 24:401-417, 1997.
 20. C-M Ma, PJ Reckwerdt, M Holmes, DWO Rogers and B Geiser, *DOSXYZ Users Manual*, national Research Council of Canada report PIRS-509B (NRCC, Ottawa, Canada) 1995.
 21. C.-M. Ma, E. Mok, A. Kapur, T. Pawlicki, D. Findley, S. Brain, K. Forster and A.L. Boyer, Clinical implementation of a Monte Carlo treatment planning system, *Med. Phys.* 26: 2133-43 (1999)
 22. C.-M. Ma and S.B. Jiang, Topical review: Monte Carlo modeling of electron beams from medical accelerators, *Phys. Med. Biol.*, (1999) 44: R167-212
 23. A. Kapur and C.-M. Ma, Stopping-powers for clinical electron beams for a scatter-foil linear accelerator, *Phys. Med. Biol.*, 45:2321-41 (1999)
 24. C.-M. Ma, T. Pawlicki, M.C. Lee, S.B. Jiang, J.S. Li, J. Deng, E. Mok, B. Yi, G. Luxton and A.L. Boyer, Energy- and intensity-modulated electron beams for radiotherapy, *Phys. Med. Biol.* (2000) 45: 2293-2311
 25. J.S. Li, T. Pawlicki, J. Deng, S.B. Jiang, E. Mok and C.-M. Ma, Validation of a Monte Carlo dose calculation tool for radiotherapy treatment planning, *Phys. Med. Biol.* (2000) 45: 2969-2985
 26. S.B. Jiang, A. Kapur and C.-M. Ma, Electron beam modelling and commissioning for Monte Carlo treatment planning, *Med. Phys.* (2000) 27:180-191
 27. C.-M. Ma, T. Pawlicki, S.B. Jiang, E. Mok, A. Kapur, L. Xing, L. Ma and A.L. Boyer, Monte Carlo verification of IMRT dose distributions from a commercial treatment planning optimization system, *Phys. Med. Biol.*, (2000) 45:2483-2495
 28. M. C. Lee and C.-M. Ma, Monte Carlo characterization of clinical electron beams in transverse magnetic fields, *Phys. Med. Biol.* (2000) 45:2947-2967

Appendices

List of Figures quoted in the body of text:

Figure 1 Comparisons of the lateral dose profiles at different depths in a water phantom between MCDOSE and EGS4/BEAM plus DOSXYZ. A 45° wedge were simulated for a 15MV photon beam, the field size was $10\text{cm} \times 10\text{cm}$ defined at 100SSD.

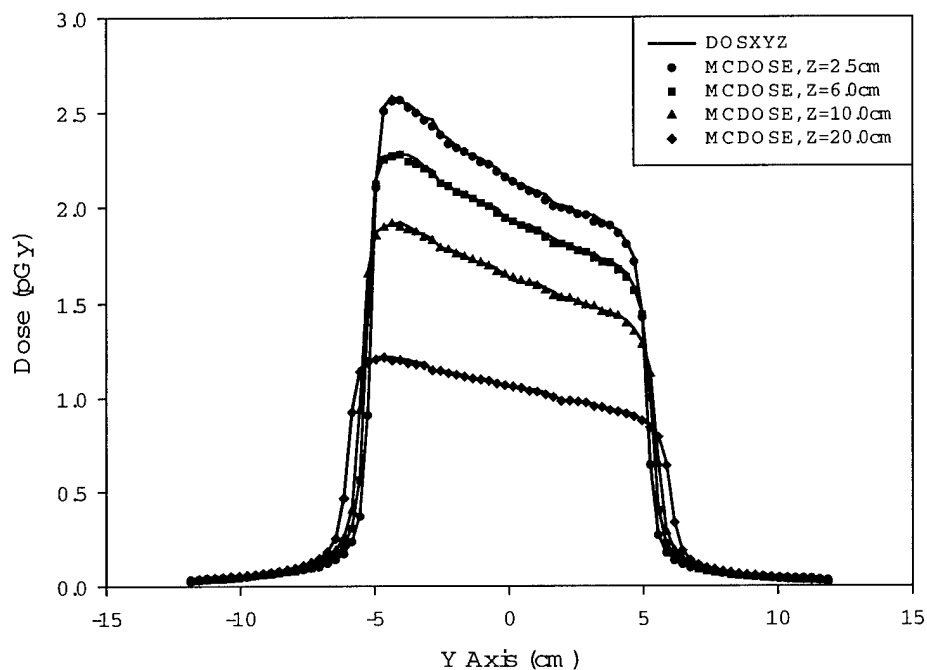
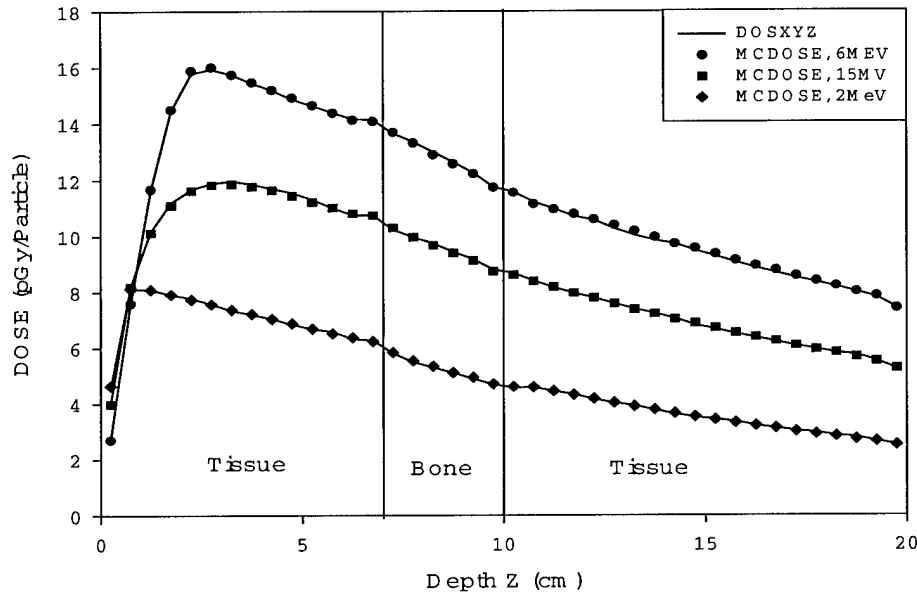
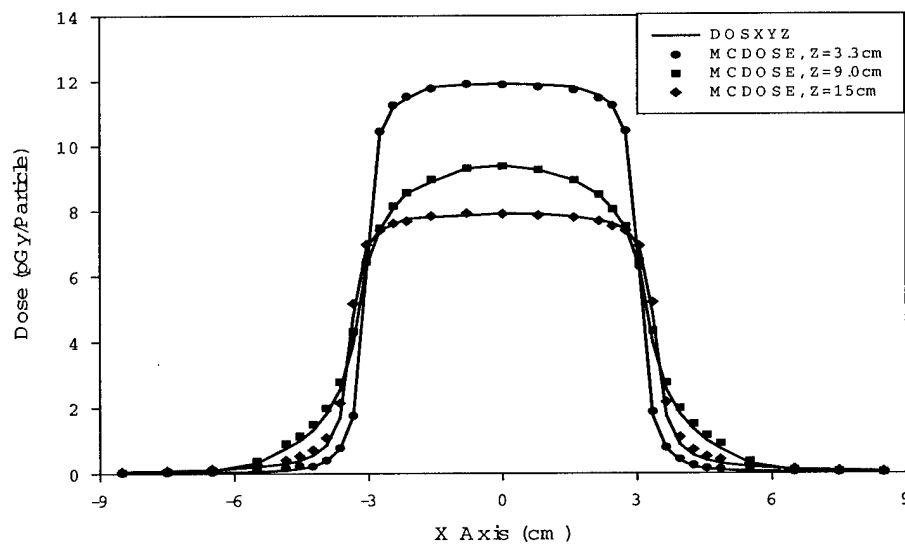


Figure 2 Depth dose curves (a) in a Tissue-Lung-Tissue phantom calculated by DOSXYZ and MCDOSE for 6MeV, 15MV and 2MeV photon beams with field size 6 cm x 6 cm defined at 100SSD and lateral dose profiles at depths of 3.3cm, 9.0cm and 15.0cm for 15MV photon beam (b). From depth of 9.0cm to 12.5cm, it was material of lung from -5.0cm to 5.0cm in X dimension and from -2.0cm to 2.0cm in Y dimension.

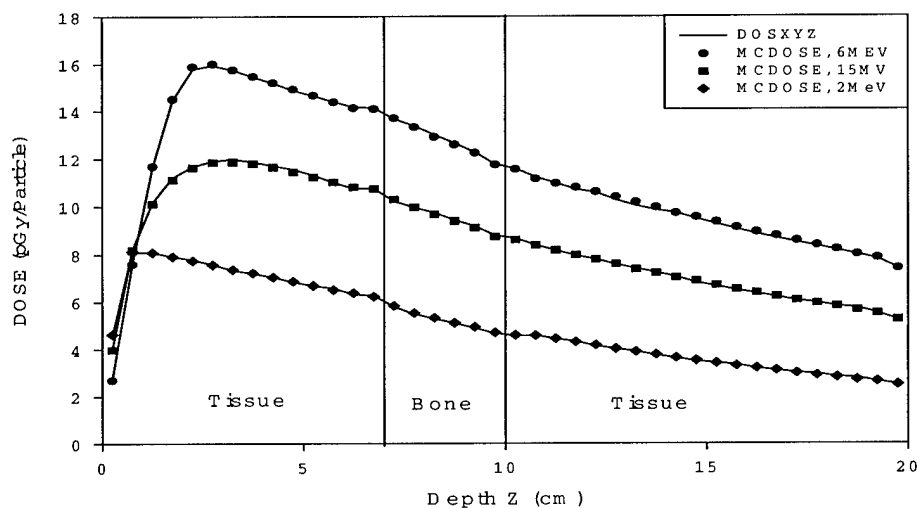


(a)

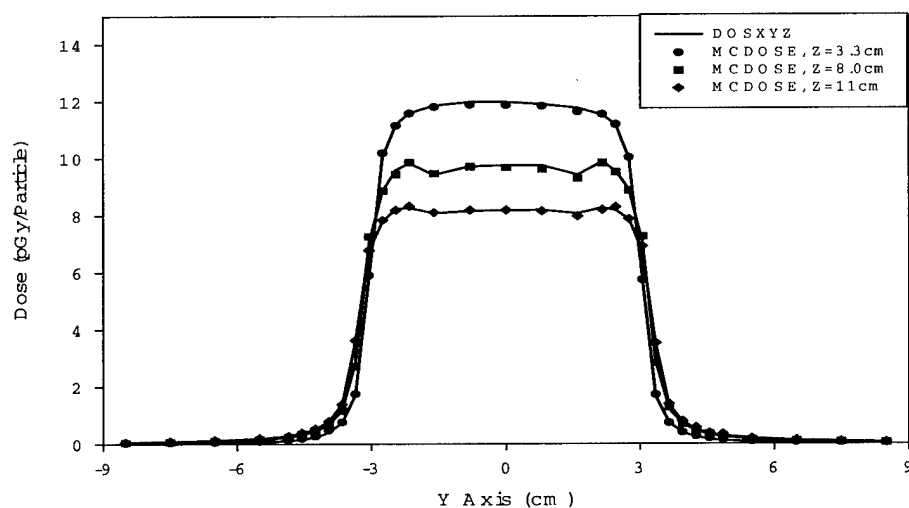


(b)

Fig. 3 Depth dose curves (a) in a Tissue-Bone-Tissue phantom calculated by DOSXYZ and MCDOSE for 6MeV, 15MV and 2MeV photon beams with field size 6 cm \times 6 cm defined at 100SSD and lateral dose profiles at depths of 3.3cm, 8.0cm and 11.0cm for 15MV photon beam (b). From depth of 7.0cm to 10.0cm, it was material of bone from -2.0 cm to 2.0 cm in Y dimension and from -5.0 cm to 5.0 cm in X dimension.



(a)



(b)

Figure 4 The beam eye views of the dose distributions at DMAX in a water phantom for a 10cm x 10cm 12MeV electron beam. The beam was modified using an electron cutout with a butterfly-shaped opening. The simulation results of BEAM (thin lines) and MCDOSE (thick lines) are shown.

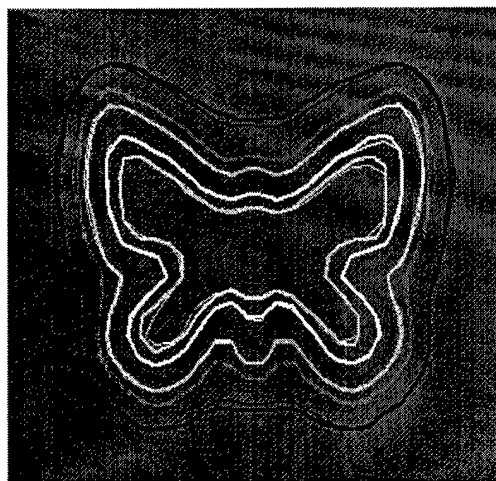


Figure 5 Dose distribution for a hypothetical target in the PMMA phantom with bone insert calculated by Monte Carlo. Nine 15 MV photon beams were used. The dose at the center of the target was measured using an ion chamber.

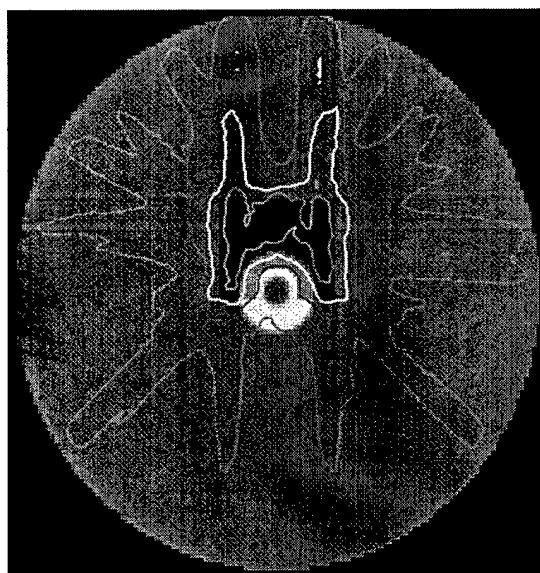
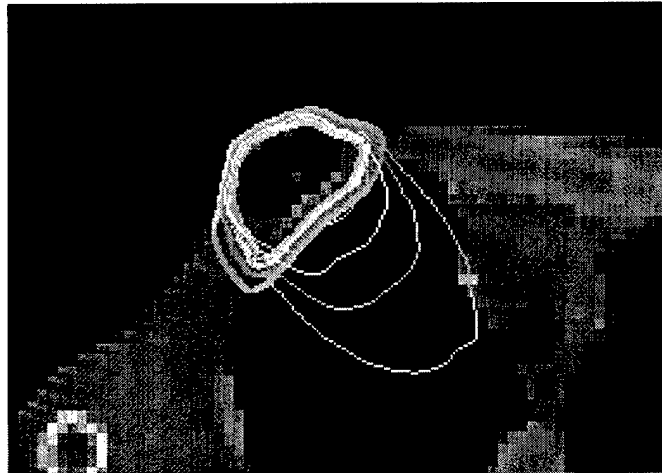
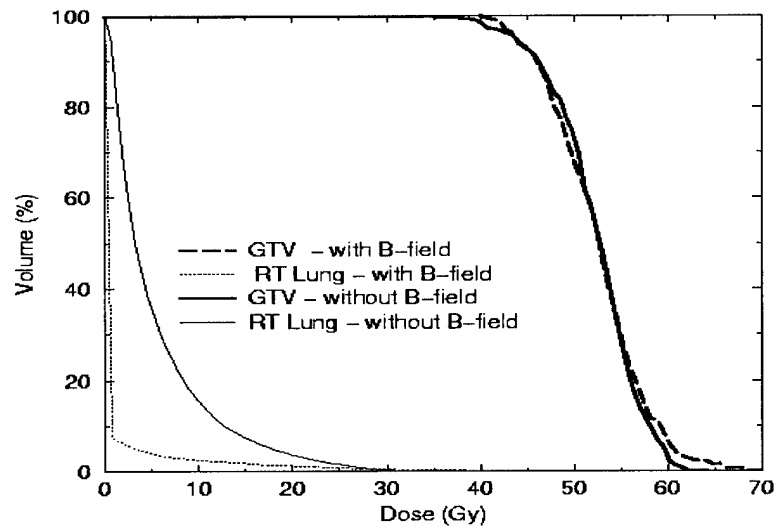


Figure 6 (a) Isodose curves for a breast treatment plan. Thick lines are optimized dose distributions for MERT with 1.5 T magnetic fields and thin lines are MERT without magnetic fields. The target coverage is similar but the dose to the lung behind the target is almost completely removed with the “soft collimation” using a magnetic field. (b) dose volume histograms for the two plans shown in (a).



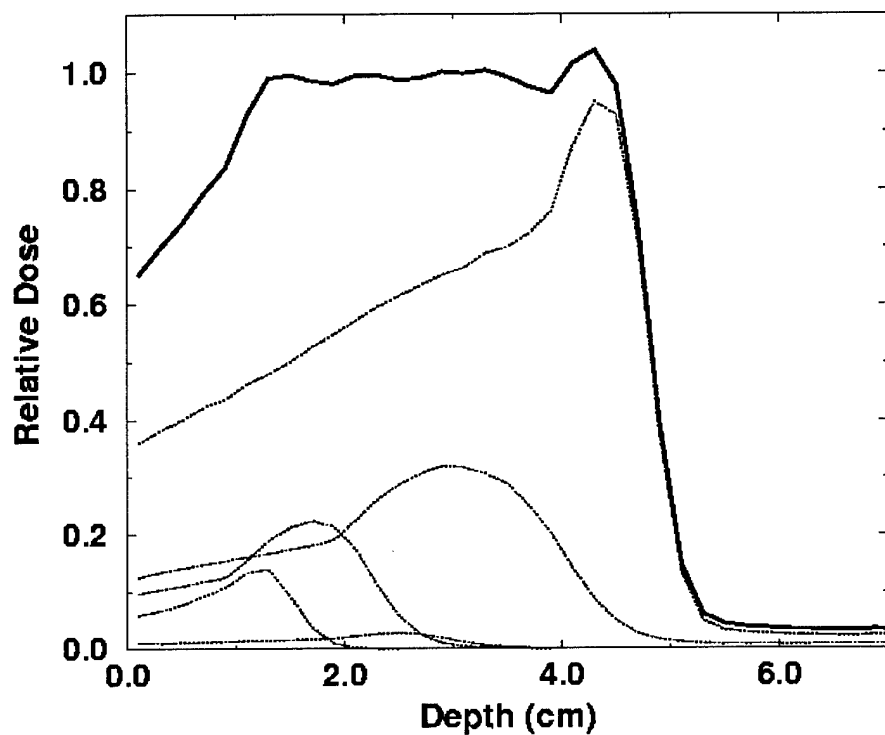
(a)

DVH Data



(b)

Figure 7 Central-axis depth-dose curves demonstrating how linear combinations of 10 x10 cm² electron beams in magnetic fields, with different intensities and magnetic field placements, can be used to create homogeneous dose distributions. The dose curves were for the 1.5 T optimization.



List of manuscripts submitted with this report:

1. C.-M. Ma, T. Pawlicki, M.C. Lee, S.B. Jiang, J.S. Li, J. Deng, E. Mok, B. Yi, G. Luxton and A.L. Boyer, Energy- and intensity-modulated electron beams for radiotherapy, *Phys. Med. Biol.* (2000) 45: 2293-2311
2. J.S. Li, T. Pawlicki, J. Deng, S.B. Jiang, E. Mok and C.-M. Ma, Validation of a Monte Carlo dose calculation tool for radiotherapy treatment planning, *Phys. Med. Biol.* (2000) 45: 2969-2985
3. S.B. Jiang, A. Kapur and C.-M. Ma, Electron beam modelling and commissioning for Monte Carlo treatment planning, *Med. Phys.* (2000) 27:180-191
4. C.-M. Ma, T. Pawlicki, S.B. Jiang, E. Mok, A. Kapur, L. Xing, L. Ma and A.L. Boyer, Monte Carlo verification of IMRT dose distributions from a commercial treatment planning optimization system, *Phys. Med. Biol.*, (2000) 45:2483-2495
5. M. C. Lee and C.-M. Ma, Monte Carlo characterization of clinical electron beams in transverse magnetic fields, *Phys. Med. Biol.* (2000) 45:2947-2967

Energy and intensity modulated electron beams for radiotherapy

C-M Ma, T Pawlicki, M C Lee, S B Jiang, J S Li, J Deng, B Yi, E Mok and A L Boyer

Department of Radiation Oncology, Stanford University School of Medicine, Stanford, CA 94305-5304, USA

E-mail: cma@reyes.stanford.edu

Received 5 January 2000, in final form 10 April 2000

Abstract. This work investigates the feasibility of optimizing energy- and intensity-modulated electron beams for radiation therapy. A multileaf collimator (MLC) specially designed for modulated electron radiotherapy (MERT) was investigated both experimentally and by Monte Carlo simulations. An inverse-planning system based on Monte Carlo dose calculations was developed to optimize electron beam energy and intensity to achieve dose conformity for target volumes near the surface. The results showed that an MLC with 5 mm leaf widths could produce complex field shapes for MERT. Electron intra- and inter-leaf leakage had negligible effects on the dose distributions delivered with the MLC, even at shallow depths. Focused leaf ends reduced the electron scattering contributions to the dose compared with straight leaf ends. As anticipated, moving the MLC position toward the patient surface reduced the penumbra significantly. There were significant differences in the beamlet distributions calculated by an analytic 3-D pencil beam algorithm and the Monte Carlo method. The Monte Carlo calculated beamlet distributions were essential to the accuracy of the MERT dose distribution in cases involving large air gaps, oblique incidence and heterogeneous treatment targets (at the tissue–bone and bone–lung interfaces). To demonstrate the potential of MERT for target dose coverage and normal tissue sparing for treatment of superficial targets, treatment plans for a hypothetical treatment were compared using photon beams and MERT.

(Some figures in this article are in colour only in the electronic version; see www.iop.org)

1. Introduction

Photon beams have been an effective modality for breast cancer treatment in radiation therapy. Although such conventional treatment with tangential photon fields has been successful, the following two problems (or potential areas of improvement) remain:

- (a) The inclusion of the lung and other normal tissues, and sometimes of a small volume of the heart, in the high-dose volume due to tumour location, patient size or in the case of chest-wall treatments.
- (b) High exit or scatter dose to the normal structures such as the lung, the heart and the contralateral breast.

Advances in the state of the art of computer-controlled medical linear accelerators have recently become available that, along with newly developed treatment planning techniques, may provide significant improvements in the delivery and control of external beam radiation through beam-intensity modulation (Boesecke *et al* 1988, Brahme 1988, Convery and

Rosenbloom 1992, Leibel *et al* 1992, Webb 1992, 1997, LoSasso *et al* 1993, Powlis *et al* 1993, Chui *et al* 1994, Mageras *et al* 1994, Brewster *et al* 1995, Fraass *et al* 1995, Kutcher *et al* 1995, Mackie *et al* 1995, McShan *et al* 1995, Ling *et al* 1996, Boyer *et al* 1997). It is expected that using photon IMRT, the problem (a) above may be significantly improved but (b) may become more serious as treatment time increases with the number of fields/segments used (increased leakage or scattering dose). Using the modulated electron radiotherapy (MERT) technique (Lief *et al* 1996, Hyödynmaa *et al* 1996, Zackrisson and Karlsson 1996, Åsell *et al* 1997, Ebert and Hoban 1997, Karlsson *et al* 1998, 1999), on the other hand, problem (a) may also be significantly improved and problem (b) may almost be eliminated due to the nature of the electron beams.

In the optimization process of MERT, dose conformity along the beam direction can be achieved by modulating the electron incident energy, making use of the sharp dose fall-off feature. A drawback is its large penumbra at large depths. Traditionally, electron beams are shaped using a cutout (or blocks) and beam penetration/intensity may be modified using a bolus. However, it is time-consuming to make such beam modifiers and the treatment time would be significantly increased if such beam modifiers are used for MERT. Efforts have been made to use computer-controlled MLC for electron beam modulation. The recent results by Karlsson *et al* (1999) showed that by replacing the air in the treatment head with a low-cost, custom-made helium balloon, the beam penumbral width (20/80) was reduced from 18 to 11 mm at 80 cm SSD. The beam characteristics are affected by the position of the MLC. However, by replacing the air between the MLC and the patient with a helium balloon, the beam penumbra become almost the same as that achieved by electron beam-shaping with an electron applicator that extends to the patient skin surface (Karlsson *et al* 1999). This means that many of the techniques so far developed with computer-controlled MLC and our experience with MLC photon beam modulation can be adopted for use with MERT.

The calculation of dose distributions for electron beam radiotherapy planning is challenging because electron scattering is strongly affected by changes in density and composition in the patients. The 3D pencil beam algorithm (Hogstrom *et al* 1981) is a fast analytical algorithm which has been adopted by most treatment planning systems. However, it has limitations with small irregular electron fields and in the presence of inhomogeneities (Cygler *et al* 1987, Bielajew *et al* 1987, Mah *et al* 1989, Mackie *et al* 1994, Ma *et al* 1999). The Monte Carlo simulation has been demonstrated to be a viable option for such complex situations, and also the only way to take into account back-scattering from denser materials in a patient (e.g. bone or metal inserts) (Shortt *et al* 1986, Cygler *et al* 1987, Mackie *et al* 1994, Kawrokwaw *et al* 1996, Mohan 1997, Kapur 1999, Ma *et al* 1999). The EGS4/BEAM system was developed for the simulation of radiotherapy beams from various radiotherapy treatment units, such medical accelerators (Rogers *et al* 1995). Excellent agreement (1–3%) has been achieved between the Monte Carlo dose distributions calculated using the simulated particle phase-space data and measurements (Rogers *et al* 1995, Kapur *et al* 1998, Zhang *et al* 1999, Ma *et al* 1999). We have installed a Monte Carlo patient dose calculation tool on a clinical treatment planning system (Ma *et al* 1999) and used Monte Carlo for treatment planning and dose delivery validation. This has reduced the uncertainty of the accelerator output for small irregular field electron beams from up to 10% to about 3% (Ma *et al* 1997, Kapur *et al* 1998).

Conformal radiotherapy was initially used to limit the normal tissue dose by conforming the treatment field to the beam's-eye-view projection of the target volume (Takahashi 1965). For photon beams, the MLC was used to collimate the fields and later to modulate the beam intensity in the field (Boesecke *et al* 1988, Brahme 1988, Convery and Rosenbloom 1992, Leibel *et al* 1992, Webb 1992, 1997, LoSasso *et al* 1993, Powlis *et al* 1993, Chui *et al* 1994, Mageras *et al* 1994, Brewster *et al* 1995, Kutcher *et al* 1995, Mackie *et al* 1995,

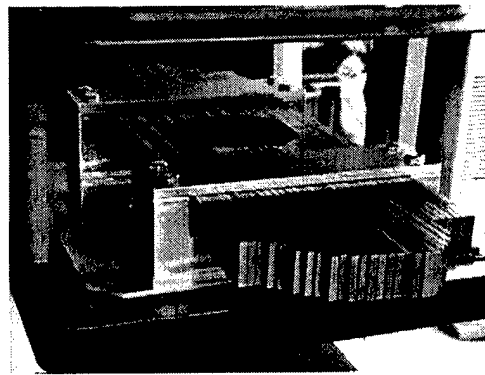


Figure 1. A prototype of an electron MLC mounted on the bottom scraper of a 25 cm \times 25 cm applicator on a Varian Clinac 2100C accelerator. The MLC has 30 pairs of steel leaves and the leaf positions are fixed by the tightening screws.

McShan *et al* 1995, Ling *et al* 1996, Boyer *et al* 1997). There have been a few studies on electron conformal therapy. Tailoring dose distributions using electron beams requires substantial beam manipulation, due to their scattering characteristics. Such manipulation is already possible with radiation sources such as microtrons where preferential energy selection and magnetically scanned pencil beams are possible (Lief *et al* 1996). Both intensity- and energy/intensity-modulated electron beams have been investigated to conform the dose to the target near the surface (Lief *et al* 1996, Hyödynmaa *et al* 1996, Zackrisson and Karlsson 1996, Ebert and Hoban 1997, Karlsson *et al* 1998). More recent work has studied the combination of photon IMRT and MERT for targets at greater depth (Karlsson *et al* 1999). Using the helium-balloon technique together with a computer-controlled MLC, it may be possible to deliver a set of intensity-modulated beams with different energies and incident angles.

In this work, we investigate the feasibility of optimizing energy- and intensity-modulated electron beams for radiotherapy treatment. We report here our Monte Carlo studies of a multileaf collimator specially designed for MERT and some preliminary experimental results. We also report on the dose calculation algorithms and their effects on treatment plan optimization for MERT. We will discuss the differences in the beam characteristics between a photon MLC and an electron MLC. We will compare the dose distributions between a conventional tangential photon treatment plan and a MERT treatment plan for a hypothetical breast treatment to demonstrate the potential of MERT for target dose coverage and normal tissue sparing.

2. Materials and method

2.1. The prototype electron MLC

We have developed a prototype manual-driven electron MLC for the beam delivery for MERT. As shown in figure 1, the electron MLC consists of 30 steel leaf pairs, which were made from the off-the-shelf steel bars for convenience and cost-effectiveness. Each leaf is 0.476 cm wide, 20 cm long and 2.54 cm thick with straight edges and ends. The leaves were mounted on a steel frame, which can be attached to the bottom scraper of a 25 cm \times 25 cm electron applicator on a Varian Clinac 2100C (Varian Oncology Systems, Palo Alto, CA). The leaves can slide in

the steel frame and the leaf positions can be easily set using a pre-cut cardboard for a beam segment. The field shape is maintained by tightening the screws from the side. The largest radiation field available using the electron MLC was 15.7 cm \times 15.7 cm projected at 100 cm source-surface distance (SSD).

Because of the existing electronic device for inserting the electron cutout, the leaves could not be placed at the last scraper level without modifying the existing applicator geometry. Instead, the steel frame was inserted using the electron cutout mount and the leaves were placed immediately above the last scraper. This resulted in a slightly greater air gap (7 cm) between the bottom of the electron MLC leaves and the phantom surface (assuming a 97 cm SSD) compared with that of an electron cutout (5 cm for a 100 cm SSD). The projected leaf width for a 5 cm air gap is 0.5 cm, while for a 7 cm air gap the projected leaf width is 0.51 cm (e.g. for the current configuration at 97 cm SSD). Further modifications are needed to the electron applicator geometry in order to lower the electron MLC leaves. The ideal location for the MLC leaves is the last scraper since electron cutouts will no longer be needed if an electron MLC is in place.

Film measurement was performed to study the characteristics of the electron beams collimated by the electron MLC. The film was calibrated following the AAPM TG-25 recommendations (AAPM 1991) and the exposures were taken by placing film at different depths in a solid water phantom. The film was scanned using a film scanner which has a spatial resolution of about 0.15 cm.

2.2. The Monte Carlo beam simulation

We have used the EGS4 (Nelson *et al* 1985) user code BEAM for the accelerator head simulation. Detailed descriptions of the software can be found in Rogers *et al* (1995). A detailed description of the clinical implementation of the Monte Carlo method at the Stanford Medical Center was given in a previous publication (Ma *et al* 1999).

For this work, we have used the previously simulated Monte Carlo beam data for 6, 12 and 20 MeV electron beams from a Varian Clinac 2100C linear accelerator and for 6 MV photon beams from a 2300CD accelerator (Varian Oncology Systems, Palo Alto, CA). The dimensions and materials for the accelerator components were incorporated according to the manufacturer's specifications. Electron beams emerging from the vacuum exit window were assumed to be monoenergetic and monodirectional with a beam radius of 0.1–0.2 cm (Kapur *et al* 1998). The energy cutoffs for electron transport in the accelerator simulation (ECUT and AE) were 700 keV (kinetic + rest mass) and for photon transport (PCUT and AP) 10 keV. The electron transport step length was confined such that the maximum fractional energy loss per electron step is 4% (i.e. ESTEPE = 0.04). The ICRU recommended compositions and stopping power values were used for the materials in the accelerator simulations (ICRU 1984). The phase-space data were scored at a plane either immediately above the photon MLC or above the lowest scraper. The number of particles was about 2–30 million in an electron beam file and about 50 million in a photon file.

Field shaping by the photon MLC or electron MLC was further simulated using the BEAM component module MLC. MLC could simulate either straight or 'double focused' leaf edges and ends. In this work, we have simulated electron beams collimated by a photon MLC with both straight and double focused MLC leaf shapes. The leaves were 7.5 cm thick and made of tungsten. The leaf center was 49 cm from the isocentre. The intervening air in the accelerator and between the MLC and the isocentre was in some cases replaced with helium to investigate the effect of electron scattering in the air. In the simulations of the electron beams collimated by an electron MLC, the leaves were placed on the bottom scraper of a 25 cm \times 25 cm applicator

with a 7 cm air gap between the bottom surface of the MLC and the isocentre. Tungsten leaves of 1.5 cm thickness with straight edges and ends were used in all the simulations and the phase space data were used in the subsequent dose calculations except for the leaf leakage study where different leaf materials and thicknesses were investigated for the electron MLC.

2.3. The Monte Carlo dose calculation

The EGS4 user code, MCDOSE (Ma *et al* 1999), was used in this work for the dose calculations. MCDOSE was designed for dose calculations in a 3D rectilinear voxel geometry. Voxel dimensions were completely variable in all three directions. Every voxel (volume element) could be assigned to a different material. The cross-section data for the materials used were available in a pre-processed PEGS4 cross-section data file. The mass density of the material in a MCDOSE calculation was varied based on the patient's CT data although the density effect corrections for the stopping powers of the material remain unchanged (Ma *et al* 1999). The voxel dimensions and materials were defined in a MCDOSE input file together with the transport parameters such as the energy cutoffs (ECUT and PCUT), the maximum fractional energy loss per electron step (ESTEPE), and the parameters required by PRESTA (Bielajew and Rogers 1987). Several variance reduction techniques have been implemented in the MCDOSE code to improve the calculation efficiency. These include photon interaction forcing, particle splitting, Russian roulette, electron range rejection and region rejection, particle track displacement and rotation, and correlated sampling. Detailed descriptions of these techniques have been given elsewhere (Rogers and Bielajew 1990, Ma and Nahum 1993, Rogers *et al* 1995, Kawrakow *et al* 1996, Keall and Hoban 1996, Ma *et al* 1999).

For patient dose calculations, the simulation phantom was built from the patient's CT data with up to $128 \times 128 \times 128$ voxels (uniform in any dimension). The side of a voxel varied from 0.2 to 0.4 cm. A separate program was developed to convert the patient's CT data from the FOCUS treatment planning system (Computerized Medical Systems, St Louis, MO) to desired dimensions, material types and densities. The organ contours were also obtained for dose calculation and analysis. The phase-space data obtained from a BEAM simulation were used as a source input with variable source positions and beam incident angles. To simulate the dose distribution of a finite size beamlet used by the inverse planning process, particles were transported to the MLC plane and only those within the beamlet area ($= 1 \text{ cm} \times 1 \text{ cm}$ projected at 100 cm SSD) were allowed to go through. This ignored the bremsstrahlung photon leakage and electron scattering by the leaf ends in the optimization process (the effect was corrected in the final dose calculation, as discussed below). After optimization, a leaf sequence was generated using a modified 'step and shoot' algorithm based on our early work (Ma *et al* 1998). The final MERT dose distribution was computed based on an intensity map (a 2D distribution of particle weighting factors) reconstructed from the leaf sequence. The bremsstrahlung leaf leakage effect was included in the intensity map using the leaf sequence and pre-calculated leaf leakage data for 1.5 cm thick tungsten leaves. MCDOSE produced data files that contained geometry specifications such as the number of voxels in all the three directions and their boundaries as well as the dose values and the associated (1σ) statistical uncertainties in the individual voxels and organs (structures). The EGS4 transport parameters were ECUT = AE = 700 keV, PCUT = AP = 10 keV and ESTEPE = 0.04. The number of particle histories simulated ranged from 2 million to 30 million for a MERT treatment. The 1σ statistical uncertainty in the dose was generally 2% or smaller of the D_{max} value. The CPU time required for a MERT simulation was about 1–3 h on a Pentium III 450 MHz PC with the variance reduction option switched on.

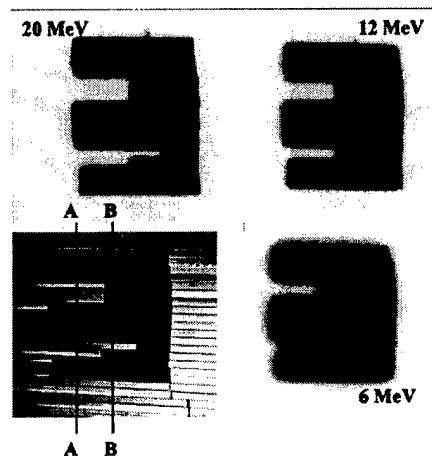


Figure 2. Beam intensity distributions measured by film on the surface of a solid water phantom for 6, 12 and 20 MeV electrons. The MLC leaf positions for the electron fields are also shown (bottom left).

2.4. The optimization process

The treatment planning optimization system used in this work is a home-developed system based on the work by Jiang (1998). First, the planner inputs the patient geometry and defines the treatment setup, such as the beam energy, number and orientations of beams, etc. The target volume and the critical structures are defined by the clinician. A reference monitor unit is assigned to each open rectangular beam and the dose deposition coefficients, which are defined as the dose contribution from a beamlet to a point, are calculated using the MCDOSE code.

Second, using the calculated dose deposition coefficients as input, the optimal intensity profile for each beam is achieved using a gradient method to minimize the objective function. For the target area, a quadratic form of objective function is specified. In addition, two target dose-uniformity constraints are used to ensure a uniform target dose distribution and to distinguish the clinical importance of cold and hot spots. For the critical structures, maximum-dose constraint and several levels of dose-volume constraints are assigned to each structure. For each objective function and constraint, an importance weight relative to the target objective function is assigned. All the constraints are mathematically transformed to the penalty functions of quadratic forms. The augmented objective function, which should be minimized, is a combination of the original objective functions and all penalty functions. The results of the optimization process are the intensity profiles for the individual fields (different incident energies and gantry angles). The same optimizer has been used for photon beam optimization with the Monte Carlo method and a finite-size pencil beam algorithm (Jiang 1998, Jiang *et al* 1999, Pawlicki *et al* 1999).

3. Results and discussion

3.1. Characteristics of electron beams collimated by an electron MLC

Figure 2 shows the electron fields collimated by the prototype electron MLC for 6, 12 and 20 MeV electron beams on a Varian Clinac 2100C machine. For convenience, a photo showing

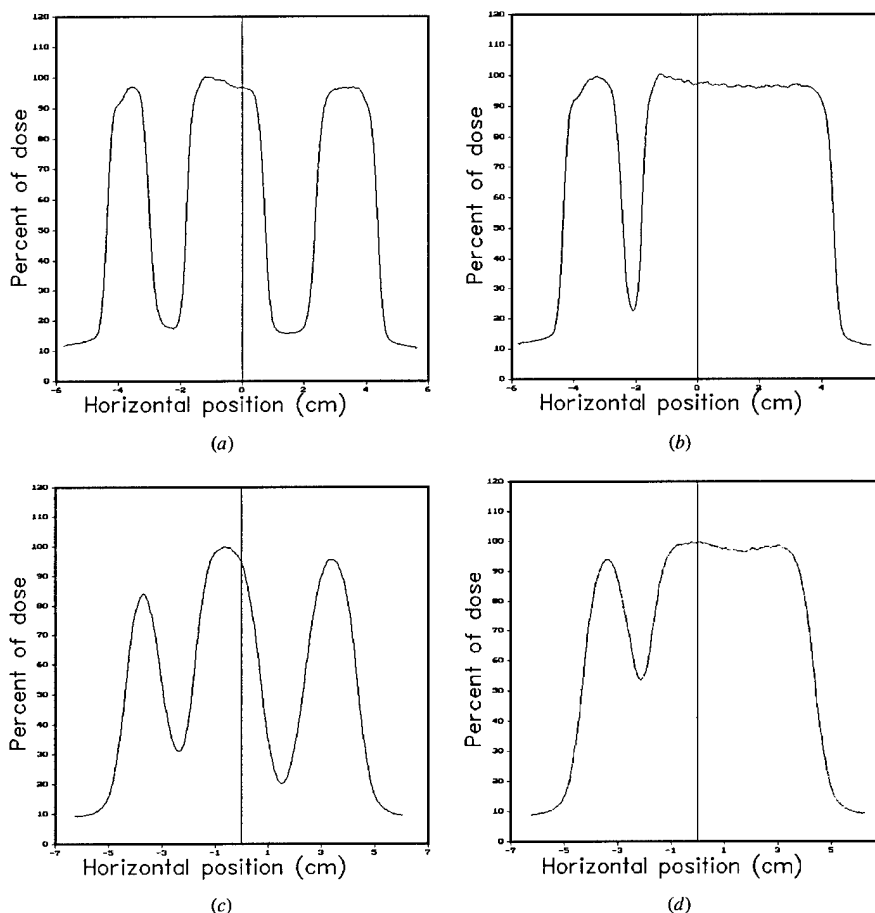


Figure 3. Beam profiles measured by film on the surface of a solid water phantom for the 6 MeV and 20 MeV electron fields shown in figure 2: (a) 20 MeV along A-A; (b) 20 MeV along B-B; (c) 6 MeV along A-A; (d) 6 MeV along B-B.

the MLC leaf positions for the field shape is also included in figure 2. Figure 2 shows the film measurement at the surface of a solid water phantom (97 cm SSD) for 6, 12 and 20 MeV electron beams. Figure 3 shows the measured profiles on the phantom surface along A-A and B-B for the 6 MeV and 20 MeV electron fields shown in figure 2. Figure 4 shows the beam profiles at 2 cm depth in the solid water phantom. It can be seen that for a 20 MeV electron beam, 0.5 cm leaf shapes are still distinguishable on the surface but become very blurred at 2 cm depth. For a 6 MeV electron beam, however, the effect of electron scattering becomes so severe that a leaf width smaller than 1.0 cm will not result in any improvement in the spatial resolution. However, a small leaf width may have the advantage of defining the field more precisely in the direction perpendicular to the leaves.

Based on these experimental results, we further performed Monte Carlo simulations of electron fields collimated by 1 cm wide leaves to study the effect of material type and

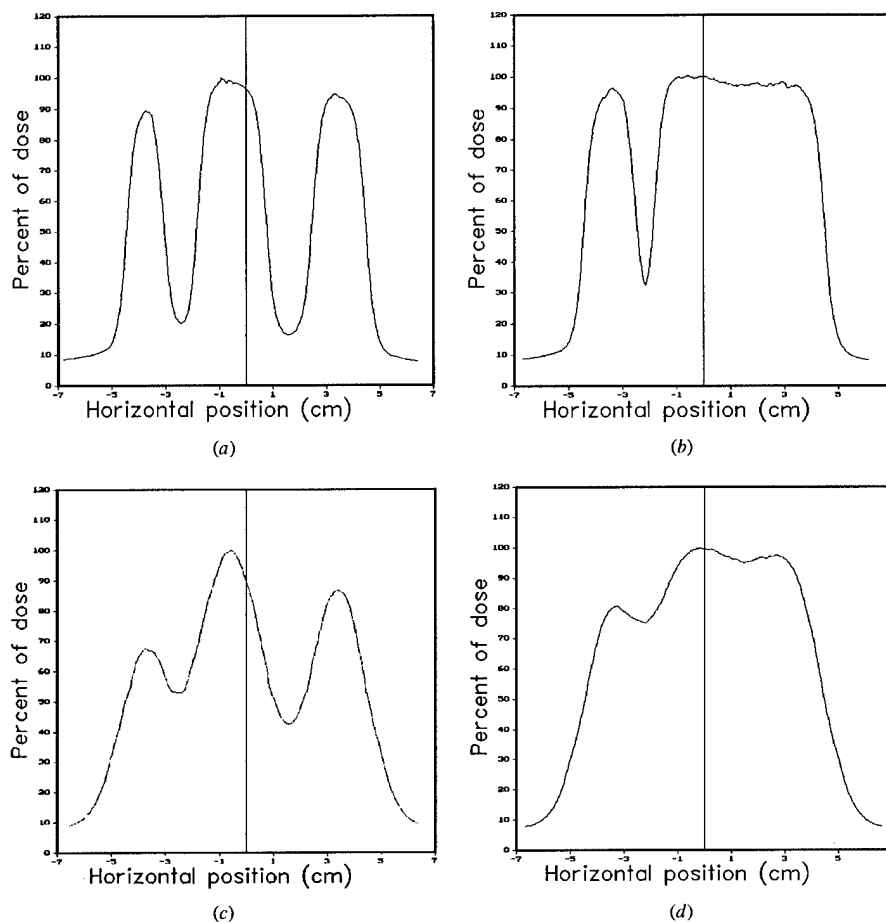


Figure 4. Beam profiles measured at 2 cm depth in a solid water phantom for the 6 MeV and 20 MeV electron fields shown in figure 2: (a) 20 MeV along A-A; (b) 20 MeV along B-B; (c) 6 MeV along A-A; and (d) 6 MeV along B-B.

leaf thickness. Although the beam penumbral widths did not change significantly for leaf thicknesses smaller than 2 cm, the beam intensity outside the field was affected by the leaf thickness and the atomic number of the leaf material. As shown in figure 5 for a 20 MeV electron beam, 1.5 cm thick zinc reduced the electron fluence outside the field to about 5% of the central axis value (figure 5(a)). These electrons were mainly generated by the bremsstrahlung photons in the MLC leaves. This was confirmed by the photon fluence as shown in figure 5(b), where 1.5 cm zinc MLC leaves resulted in about 60% higher photon fluence outside the field compared with the central axis photon fluence. Some electrons were also scattered off the leaf ends and by air. For 1.5 cm copper, 1.5 cm lead and 2 cm steel, the electron fluence was about 2.5% of the central axis value. The electron fluence was reduced to about 1.5% if the leaves were made of 1.5 cm tungsten. This was reflected by the 30% smaller photon fluence under the tungsten MLC leaves compared with the central axis photon fluence. Clearly, tungsten was superior to

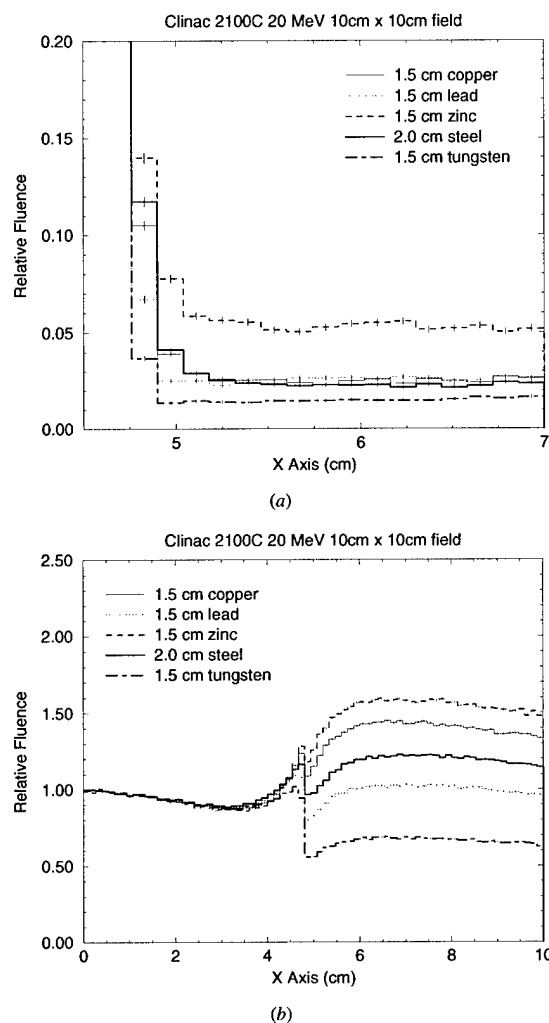


Figure 5. Monte Carlo simulated electron (a) and photon (b) planar fluence in the penumbral region and outside the treatment field for a Varian Clinac 2100C 20 MeV electron beam collimated by an electron MLC of different leaf materials and thicknesses. The air gap between the electron MLC and the scoring plane is 7 cm.

other materials in terms of leaf leakage. If we increased the tungsten leaf thickness to 2 cm the electron fluence would be reduced to less than 1% of the central axis value and the photon leakage would be reduced to about 50% of the central axis value (not shown).

To study the overall effect of the leaf leakage, leaf scattering, air scattering and the extended source in an electron beam, we compared the dose distributions for single fields and multiple abutting fields collimated by an electron MLC with 1.5 cm thick tungsten leaves. Figure 6 shows the Monte Carlo calculated dose distributions for a single 4 cm \times 4 cm electron field and a multiple abutting field of the same size formed by four 1 cm \times 4 cm electron fields. For

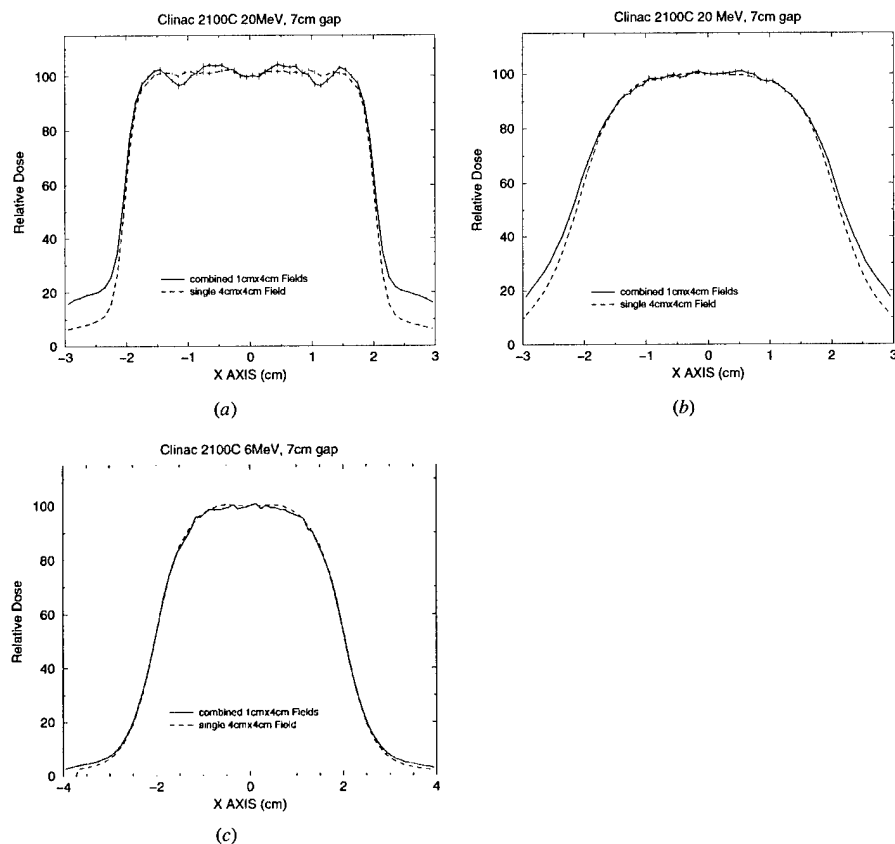


Figure 6. Monte Carlo calculated dose distributions in a water phantom for Varian Clinac 6 and 20 MeV electron beams collimated by an electron MLC of 1.5 cm thick tungsten leaves for a single 4 cm \times 4 cm electron field and a 4 cm \times 4 cm field formed by four 1 cm \times 4 cm electron fields: (a) dose at surface for a 20 MeV beam; (b) dose at 3 cm depth for a 20 MeV beam; (c) dose at surface for a 6 MeV beam.

a 20 MeV electron beam, the dose at the phantom surface for the abutting field shows about 4% fluctuation compared with a single electron field (figure 6(a)). This is potentially due to the effect of leaf shape and extended source. The dose outside the field for the abutting field is about three times higher than that for the single field, which is mainly caused by the leaf leakage due to the longer beam-on time to deliver the four 1 cm \times 4 cm fields and electron scattering off the leaf ends. The dose at 3 cm depth shows little difference between the abutting field and the single field except for the dose near the field edges and outside the field (figure 6(b)). For a 6 MeV electron beam, the dose at the phantom surface for the abutting field is almost the same as that for the single field (figure 6(c)). The dose outside the field for the abutting field is only slightly higher than that for the single field. The effect of leaf leakage is very small for a 6 MeV beam and the dose immediately outside the field is thought to be mainly due to the effect of electron scattering in the air. It seems that field abutting with 1 cm beamlets collimated by an electron MLC can provide adequate beam characteristics for MERT for the beam energies

investigated. However, the dose outside the field needs to be minimized through beam energy and leaf sequence optimization.

3.2. Comparisons of a photon MLC and an electron MLC

There have been studies on electron beam collimation using a photon MLC (Karlsson *et al* 1999). One of the advantages of using a photon MLC is the possibility of combining both photon and electron beams in the same plan. An essential requirement for matching a photon beam and an electron beam at different depths is that both beams share the same source position. Karlsson *et al* (1999) proposed several modifications to the design of a Varian Clinac 2300CD accelerator, one of which was to replace the intervening air with helium. This could significantly reduce the effect of electron scattering in the air on the beam penumbra. However, filling the accelerator head with helium requires major modifications to the existing accelerator design. In this work, we have investigated an alternative solution—a thin leaf MLC at the electron cutout level to reduce the air scattering effect. As can be seen in figure 7, the unfocused MLC leaf ends could scatter the electrons very significantly to degrade the beam characteristics near the field edges. The Varian MLC has rounded leaf ends, which are expected to have similar dosimetric characteristics as the unfocused MLC studied here. Focused leaf ends could greatly improve the beam edges and provided even slightly better dose profiles inside the field for a 20 MeV electron beam compared with an electron MLC (figures 7(a)–(c)), primarily due to the reduction of electron scattering in the accelerator head (helium versus air). The dose outside the field was slightly lower for the electron MLC than for the photon MLC. For a 6 MeV beam, an electron MLC gave slightly better surface dose profiles both inside and outside the field than the focused and unfocused photon MLC. However, the dose profiles became practically similar at the depth of the maximum dose and greater depths (not shown). Note that in these comparisons, we have placed the phantom surface at 20 cm below the photon MLC and 7 cm below the electron MLC to minimize the effect of electron scattering in the air or helium between the MLC and the phantom. It is evident that an electron MLC will have similar dosimetric characteristics as a photon MLC with focused leaf ends but without the need to replace the air in the accelerator head with helium.

3.3. Comparison of beamlet distributions

The accuracy of the beamlet distribution calculation may play an important role in the treatment planning optimization process. Ma *et al* (1999) reported significant differences in the final dose distributions of the optimized treatment plans computed by a commercial inverse treatment planning system with a finite-size pencil beam and the Monte Carlo method. Pawlicki *et al* (1999) demonstrated that inaccurate beamlet distributions may result in under-dosing in the target and over-dosing in the adjacent critical structures, and using the Monte Carlo calculated beamlets could potentially reduce the uncertainty in the photon IMRT dose distributions. This was demonstrated again by Jeraj and Keall (1999) using a Monte Carlo dose calculation based inverse planning algorithm.

It has been shown that the electron beam dose distributions calculated by the pencil beam algorithm as implemented in some commercial treatment planning systems could be fairly uncertain in the regions near material interfaces and inhomogeneities (Cygler *et al* 1987, Shortt *et al* 1986, Mackie *et al* 1994, Ma *et al* 1999). We have computed the beamlet dose distributions using the 3D pencil beam as implemented in the FOCUS treatment planning system (Computerized Medical Systems, St Louis, MO) and compared them with the Monte Carlo calculated beamlets. Figure 8 shows the dose distributions calculated using the Monte

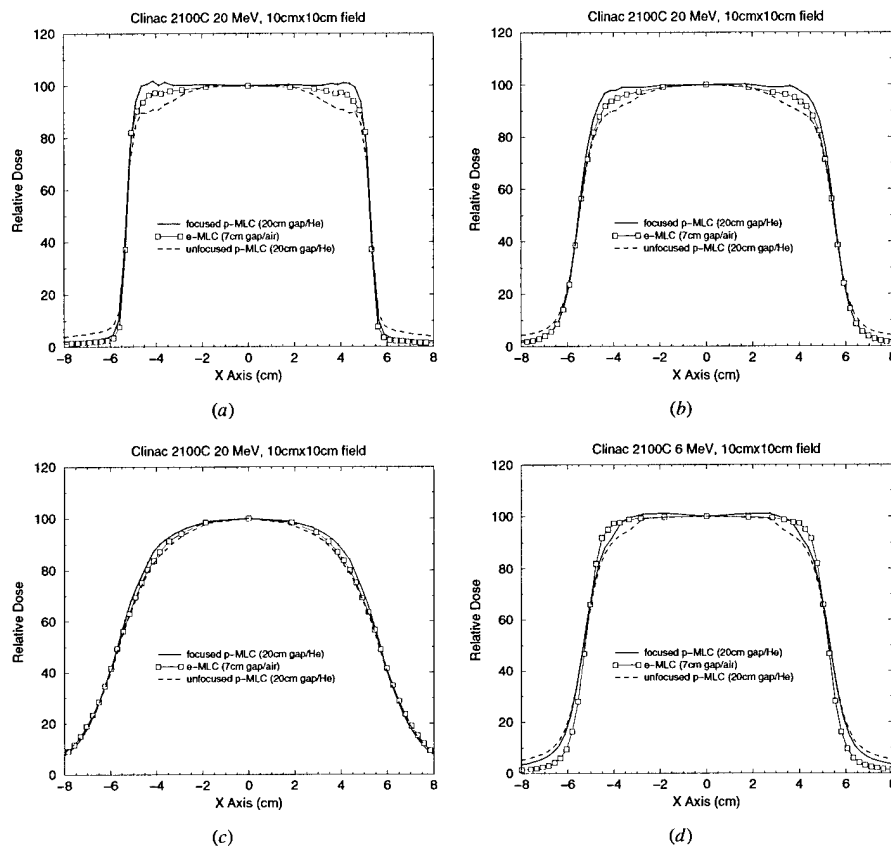


Figure 7. Monte Carlo calculated dose distributions in a water phantom for a 10 cm \times 10 cm field collimated by an electron MLC with 1.5 cm thick tungsten leaves and a photon MLC with 7.5 cm thick leaves on a Varian Clinac 2100C accelerator: (a) surface dose for a 20 MeV beam; (b) dose at 3 cm depth for a 20 MeV beam; (c) dose at 6 cm depth for a 20 MeV beam; (d) surface dose for a 6 MeV beam. The electron MLC has straight leaf ends. The photon MLC has either straight or double-focused leaves.

Carlo method (a, c, e) and the FOCUS 3D pencil beam algorithm (b, d, f) for a 1 cm \times 1 cm 12 MeV beamlet incident on a patient phantom built from CT data. For beamlets with normal incidence (figures 8(a) and (b)), the difference in the dose distributions in the heart was evident: the Monte Carlo calculated isodose lines varied with the heart contour while the pencil beam isodose lines remained symmetrical despite the change in material densities. Figures 8(c) and (d) show the beamlet distributions with a 10 cm air gap. The difference is clearly seen near the surface. The beamlet distributions again differed significantly in the lung for oblique incidence (figures 8(e) and (f)). The axis of the beamlet was intentionally placed to go through soft tissues and bones. The pencil beam isodose lines seemed to stretch according to the beam axis pathlength and showed no signs of electron build-down near the low-density material. These results provided enough evidence to show that to ensure the accuracy of the optimized dose distributions for MERT we should use the Monte Carlo method to compute the electron beamlets for the inverse planning process.

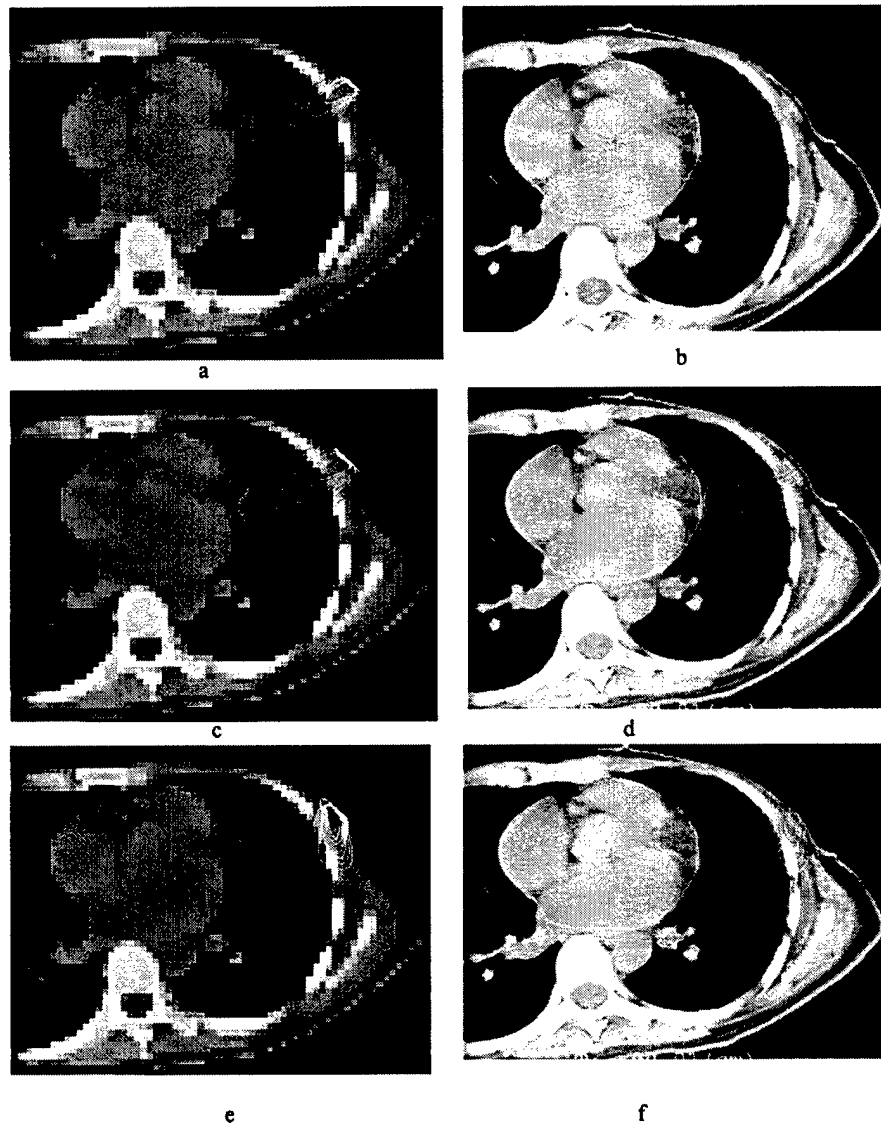


Figure 8. Dose distributions calculated using the Monte Carlo method (*a, c, e*) and the FOCUS 3D pencil beam algorithm (*b, d, f*) for a $1\text{ cm} \times 1\text{ cm}$ 12 MeV beamlet with normal incidence (*a* and *b*), normal incidence plus 10 cm air gap (*c* and *d*), and oblique incidence (*e* and *f*). The beamlet size is defined at 100 cm SSD. The isodose lines shown are 10, 20, 30, 40, 50, 60, 70, 80 and 90% of the maximum dose respectively.

3.4. MERT versus photons: a hypothetical treatment plan

Modulated electron radiotherapy is a general purpose technique that should be advantageous in many clinical situations. An exhaustive investigation of the specific advantages of MERT

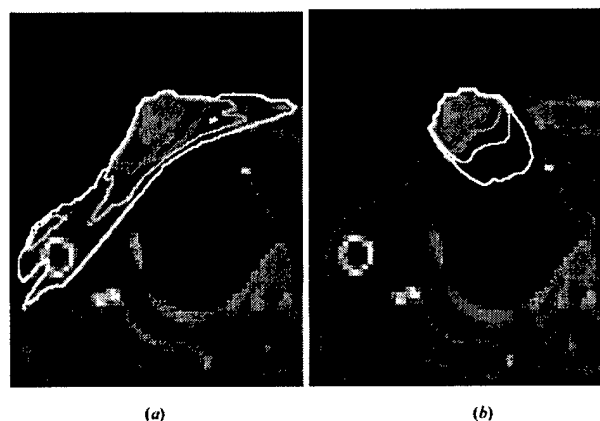


Figure 9. Treatment plans for a hypothetical breast case using tangential 6 MV photon beams (a) and MERT with 6, 12 and 20 MeV electron beams (b). Both plans were calculated using the Monte Carlo method. The isodose lines (90, 70, 50 and 30%) represented 50, 38.9, 25 and 16.7 Gy.

over traditional treatment modalities on a site by site basis is outside the scope of this work. However, to demonstrate the possibility of improving the dose homogeneity in the target and the reduction of the dose in surrounding normal tissues, we compare the dose distributions to treat a hypothetical target using tangential photon beams and MERT. The purpose of the comparison was to illustrate the concept of MERT but not to draw specific conclusions on the use of either technique. Previous investigators have used artificial phantoms and hypothetical targets to mimic different treatment sites (e.g. Hyödynmaa *et al* 1996, Åsell *et al* 1997, Ebert and Hoban 1997). We considered it to be clinically relevant to use a more realistic patient geometry (built from CT data) in our comparison, although the target definition and beam setup are somewhat arbitrary. Figure 9 shows the hypothetical treatment plan using tangential 6 MV photon beams and MERT with normally incident 6, 12 and 20 MeV electron beams. The intensity maps for each electron beam energy are shown in figure 10. The beamlet size was 1 cm \times 1 cm at 100 cm at isocentre. It is worth noting here, that as a matter of practicality, it is impossible to create the intensity maps shown in figure 10 using the conventional electron cutout approach but the electron MLC is a viable alternative. The dose distributions for both plans were calculated using the Monte Carlo method. The isodose lines (90, 70, 50 and 30%) were normalized in such a way that the 90% isodose surface would receive the prescribed target dose of 50 Gy. For the photon plan, the 90% dose line also included a margin in the lung to account for the effect of patient breathing. This was not needed for the electron plan as the electron beams were incident *en face* and the electron beamlet dose distributions do not vary significantly with breathing. Figure 11 shows the dose volume histograms (DVH) for the hypothetical treatment plans shown in figure 9. The target DVH together with the right lung DVH are shown in figure 11(a) (as percentage volume) and the right lung DVH and the 'total body' (including everything inside the external contour) DVH are shown in figure 11(b) (as absolute volume).

It is clear that MERT provided better dose homogeneity in the target region than tangential photon beams. Tangential photon beams produced hot spots in the target and cold spots near the skin (figure 11(a)). MERT significantly reduced the dose to the lung relative to tangential photon beams; the maximum dose to the lung was reduced from 50 Gy for a tangential treatment to 35 Gy for MERT (figure 11(a)). However, MERT increased the volume of the lung that

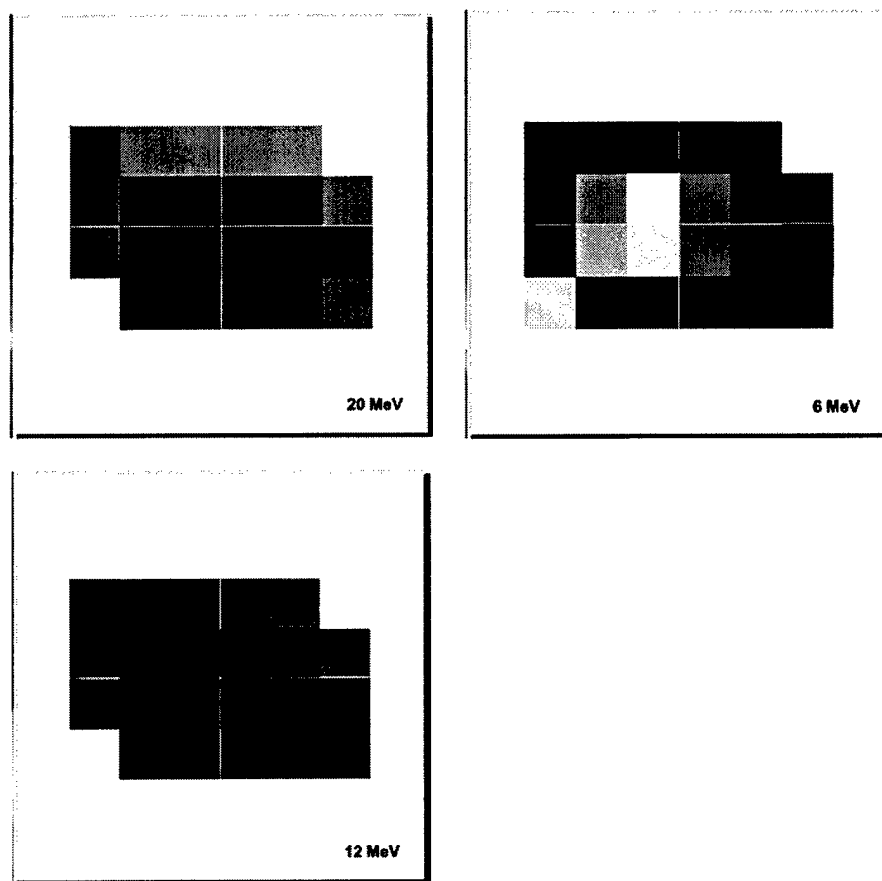
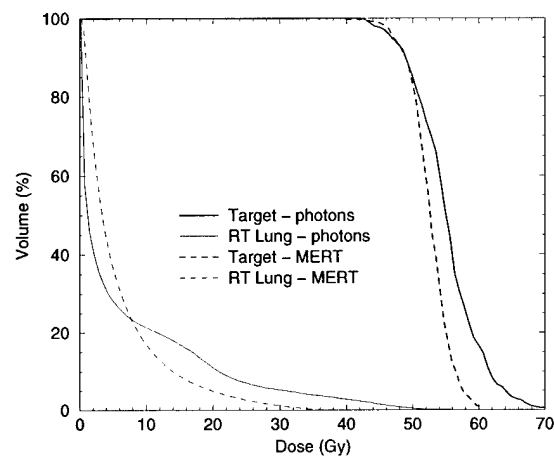


Figure 10. Intensity maps for the three electron beam energies. The beamlet size for each port was $1 \times 1 \text{ cm}^2$. Darker beamlets indicate a higher weight than the lighter beamlets and the grey scale for all three maps is in absolute terms.

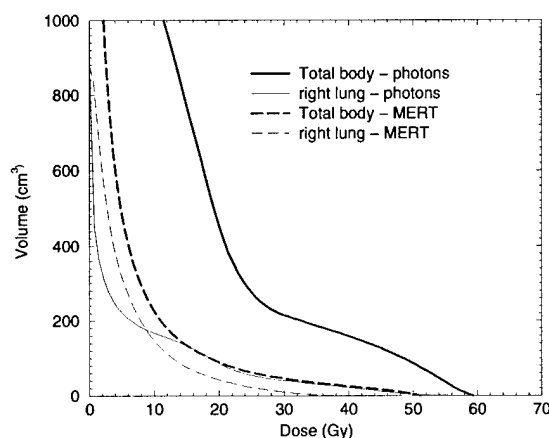
received a lower dose (10% more volume received 5 Gy and 20% more volume received 2 Gy) compared with tangential photon beams. The clinical significance of the increased lung volume receiving such a low dose needs to be investigated. On the other hand, over 150 cm^3 of lung received much less dose with MERT compared with tangential photon beams, which could result in reduced lung complications (figure 11(b)). Another clear benefit with MERT is the exclusion of the surrounding normal tissue from the high dose volume (figure 11(b)). Over 1000 cm^3 of normal tissue received 10–30 Gy less dose in a MERT plan compared with this tangential photon beam plan.

4. Conclusions

In this work, we have investigated the feasibility of modulating both energy and intensity of electron beams for radiotherapy. This was achieved by combining electron beams of different



(a)



(b)

Figure 11. Dose volume histograms (DVH) for the breast treatment plans shown in figure 9: (a) DVH shown as percentage volume for the target (PTV) and the right lung and (b) DVH shown as absolute volume for the right lung and the 'total body' which includes everything inside the external contour.

nominal energies and variable intensity distributions. A prototype electron MLC was built to study the characteristics of MLC-collimated electron beams and the Monte Carlo simulations were used to investigate the effect of MLC leaf material, thickness, shape and location. The beamlet distributions calculated using a 3D electron pencil beam algorithm as implemented in a commercial treatment planning system and the Monte Carlo method were compared for electron beams of different energies, extended air gaps, oblique incidence and heterogeneous geometries. A hypothetical breast case was used to compare the dose distributions using tangential photons and MERT for target coverage (dose homogeneity) and normal tissue sparing (dose reduction in the lung and other surrounding normal tissues).

Our results showed that an electron MLC at the electron cutout location can provide adequate beam collimation for MERT without the need to replace the air in the accelerator head and between the MLC and the phantom with helium. The beam characteristics collimated by an electron MLC are comparable to those collimated by a focused photon MLC. However, the latter requires the accelerator head and between the MLC and the phantom to be filled with helium, which may be impractical for some accelerators because of the major modifications needed to the structure design. An electron MLC can also be used in place of a cutout. The Monte Carlo method can accurately simulate particle transport in cases involving extended air gaps, oblique incidence and heterogeneous anatomy, and is therefore suitable for the beamlet calculation for MERT treatment optimization. Our preliminary results based on a hypothetical breast case demonstrated the potential of MERT for uniform target coverage and normal tissue sparing. To fully explore the potential of MERT, further studies need to be carried out for realistic clinical cases and for other treatment sites such as the head and neck.

Ac no ledgments

We would like to acknowledge Varian Oncology Systems, Palo Alto, CA, for providing detailed information on the Varian Clinac linear accelerators. We would like to thank our colleagues Fred van den Haak, for making the prototype electron MLC, and Sam Brain, Todd Koumrian, Behrooz Tofighrad and Michael Luxton for help with the computers and software support. This investigation was supported in part by grants CA78331 from the NIH, BC971292, BC990018 and BC990213 from the DOD, Seed Cycle 1 from the RSNA Research and Education Fund, and a consortium agreement with the NumeriX, LLC.

References

- AAPM 1983 AAPM TG-21, a protocol for the determination of absorbed dose from high-energy photons and electrons *Med. Phys.* **10** 741
- 1991 AAPM TG-25, Clinical electron beam dosimetry: report of AAPM Radiation Therapy Committee Task Group No. 25 *Med. Phys.* **18** 73–109
- Åsell M, Hyödynmaa S, Gustafsson A and Brahme A 1997 Optimization of 3D conformal electron beam therapy in inhomogeneous media by concomitant fluence and energy modulation *Phys. Med. Biol.* **42** 2083–100
- Bielajew A and Rogers D W O 1987 PRESTA—the parameter reduced electron step algorithm for electron Monte Carlo transport *Nucl. Instrum. Methods B* **18** 165–81
- Bielajew A F, Rogers D W O, Cygler J and Battista J J 1987 A comparison of electron pencil beam and Monte Carlo calculational methods *The Use of Computers in Radiation Therapy* ed I A D Bruinvis (Amsterdam: Elsevier) pp 65–8
- Boesecke R, Doll J, Bauer B, Schlegel W, Pastyr O and Lorenz M 1988 Treatment planning for conformation therapy using a multileaf collimator *Strahlenther. Onkol.* **164** 151–4
- Brewster L, Mohan R, Mageras G, Burman C, Leibel S and Fuks Z 1995 Three dimensional conformal treatment planning with multileaf collimators *Int. J. Radiat. Oncol. Biol. Phys.* **33** 1081–9
- Boyer A L, Geis P B, Grant W, Kendall R and Carol M 1997 Modulated-beam conformal therapy for head and neck tumors *Int. J. Radiat. Oncol. Biol. Phys.* **3** 227–36
- Brahme A 1988 Optimal setting of multileaf collimators in stationary beam radiation therapy *Strahlenther. Onkol.* **164** 343–50
- Chui C S, LoSasso T and Spirou S 1994 Dose calculations for photon beams with intensity modulation generated by dynamic jaw or multileaf collimators *Med. Phys.* **21** 1237–43
- Convery D J and Rosenbloom M E 1992 The generation of intensity-modulated fields for conformal radiotherapy by dynamic collimation *Phys. Med. Biol.* **37** 1359–74
- Cygler J, Battista J J, Scrimger J W, Mah E and Antolak J 1987 Electron dose distributions in experimental phantoms: a comparison with 2D pencil beam calculations *Phys. Med. Biol.* **32** 1073–83
- DeMarco J J, Solberg T D and Smathers J B 1998 A CT-based Monte Carlo simulation tool for dosimetry planning and analysis *Med. Phys.* **25** 1–11

- Ebert M A and Hoban P W 1997 Possibilities for tailing dose distributions through the manipulation of electron beam characteristics *Phys. Med. Biol.* **42** 2065–81
- Faddegon B A, Balogh J, Mackenzie R and Scora D 1998 Clinical considerations of Monte Carlo for electron radiotherapy treatment planning *Radiat. Phys. Chem.* **53** 217–28
- Fraass B A, McShan D L, Kessler M L, Matrone G M, Lewis J D and Weaver T A 1995 A computer-controlled conformal radiotherapy system I: overview *Int. J. Radiat. Oncol. Biol. Phys.* **33** 1139–57
- Hogstrom K R, Mills M D and Almond P R 1981 Electron beam dose calculations *Phys. Med. Biol.* **26** 445–59
- Hyödynmaa S, Gastafsson A and Brahme A 1996 Optimization of conformal electron beam therapy using energy- and fluence-modulated beams *Med. Phys.* **23** 659–66
- ICRU 1984 Radiation dosimetry: Stopping powers for electrons and positrons *ICRU Report 37* (Bethesda, MD: ICRU)
- Jeraj R and Keall P 1999 Monte Carlo-based inverse treatment planning *Phys. Med. Biol.* **44** 1885–96
- Jiang S B 1998 Development of a compensator based intensity modulated radiation therapy system *PhD Thesis* Medical College of Ohio, Toledo, OH
- Jiang S B, Boyer A L and Ma C-M 1999 A hybrid system for IMRT inverse planning and dose verification *Int. J. Radiat. Oncol. Biol. Phys.* **41** 123
- Kapur A 1999 Monte Carlo dose calculations for clinical electron and intensity modulated photon beams in radiotherapy *PhD Thesis* Stanford University, Stanford, CA, USA
- Kapur A, Ma C-M, Mok E and Findley D 1997 Characterization of small field electron beams for radiotherapy using Monte Carlo simulations *Proc. 12th Int. Conf. on the Use of Computers in Radiation Therapy (Salt Lake City, Utah)* (Madison, WI: Medical Physics Publishing) pp 157–8
- Kapur A, Ma C-M, Mok E, Findley D and Boyer A L 1998 Monte Carlo calculations of clinical electron beam output factors *Phys. Med. Biol.* **43** 3479–94
- Karlsson M G, Karlsson M K and Ma C-M 1999 Treatment head design for multileaf collimated high-energy electrons *Med. Phys.* **26** 2125–32
- Karlsson M K, Karlsson M G and Zackrisson B 1998 Intensity modulation with electrons: calculations, measurements and clinical applications *Phys. Med. Biol.* **43** 1159–69
- Kawrakow I, Fippel M and Friedrich K 1996 3D electron dose calculation using a voxel based Monte Carlo algorithm *Med. Phys.* **23** 445–57
- Keall P J and Hoban P 1996 Superposition dose calculation incorporating Monte Carlo generated electron track kernels *Med. Phys.* **23** 479–85
- Kutcher G J, Mageras G S and Leibel S A 1995 Control, correction and modeling of setup errors and organ motion *Semin. Radiat. Oncol.* **5** 134–45
- Leibel S A et al 1992 Three-dimensional conformal radiation therapy at the Memorial Sloan-Kettering Cancer Center *Semin. Radiat. Oncol.* **2** 274–89
- Lief E P, Larsson A and Humm J L 1996 Electron dose profile shaping by modulation of a scanning elementary beam *Med. Phys.* **23** 33–44
- Ling C C et al 1996 Conformal radiation treatment of prostate cancer using inversely-planned intensity-modulated photon beams produced with dynamic multileaf collimation *Int. J. Radiat. Oncol. Biol. Phys.* **35** 731–40
- LoSasso T, Chui C S, Kutcher G J, Leibel S A, Fuks Z and Ling C C 1993 The use of multileaf collimators for conformal radiotherapy of carcinomas of the prostate and nasopharynx *Int. J. Radiat. Oncol. Biol. Phys.* **25** 161–70
- Ma C-M, Mok E, Kapur A and Findley D 1997 Improvement of small-field electron beam dosimetry by Monte Carlo simulations *Proc. 12th Int. Conf. on the Use of Computers in Radiation Therapy (Salt Lake City, Utah)* (Madison, WI: Medical Physics Publishing) pp 159–62
- Ma C-M, Mok E, Kapur A, Pawlicki T A, Findley D, Brain S, Forster K and Boyer A L 1999 Clinical implementation of a Monte Carlo treatment planning system for radiotherapy *Med. Phys.* **26** 2133–43
- Ma C-M and Nahum A E 1993 Calculation of absorbed dose ratios using correlated Monte Carlo sampling *Med. Phys.* **20** 1189–99
- Ma C-M, Reckwerdt P, Holmes M, Rogers D W O and Geiser B 1995 DOSXYZ Users Manual *National Research Council Report PIRS-0509(B)* (Ottawa: NRC)
- Ma L, Boyer A L, Xing L and Ma C-M 1998 An optimized leaf setting algorithm for beam intensity modulation using dynamic multileaf collimators *Phys. Med. Biol.* **43** 1629–43
- Mackie T R, Holmes T W, Reckwerdt P J and Yang J 1995 Tomotherapy: optimized planning and delivery of radiation therapy *Int. J. Imaging Syst. Technol.* **6** 43–55
- Mackie T R et al 1994 The OMEGA project: comparison among EGS4 electron beam simulations, 3D Fermi-Eyges calculations, and dose measurements *Proc. 11th Int. Conf. on the Use of Computers in Radiation Therapy (Manchester, UK)* pp 152–3

- Mageras G S *et al* 1994 Initial clinical experience with computer-controlled conformal radiotherapy using the MM50 microtron *Int. J. Radiat. Oncol. Biol. Phys.* **30** 971–8
- Mah E, Antolak J, Scrimger J W and Pattista J J 1989 Experimental evaluation of a 2D and 3D pencil beam algorithm *Phys. Med. Biol.* **34** 1179–94
- McShan D L, Fraass B A, Kessler M L, Matrone G M, Lewis J D and Weaver T A 1995 A computer-controlled conformal radiotherapy system. II: sequence processor *Int. J. Radiat. Oncol. Biol. Phys.* **33** 1159–72
- Mohan R 1997 Why Monte Carlo? *Proc. 12th Int. Conf. on the Use of Computers in Radiation Therapy* (Salt Lake City, UT) (Madison, WI: Medical Physics Publishing) pp 16–18
- Nelson R, Hirayama H and Rogers D W O 1985 The EGS4 code system *Stanford Linear Accelerator Center Report SLAC-265* (Stanford, CA: SLAC)
- Pawlicki T A, Jiang S B, Deng J, Li J S and Ma C-M 1999 Monte Carlo calculated beamlets for photon beam inverse planning *Med. Phys.* **26** 1064–5
- Powlis W D *et al* 1993 Initiation of multileaf collimator conformal radiation therapy *Int. J. Radiat. Oncol. Biol. Phys.* **25** 171–9
- Rogers D W O and Bielajew A F 1990 Monte Carlo techniques of electrons and photons for radiation dosimetry *Dosimetry of Ionizing Radiation* vol III, ed K Kase, B E Bjarngard and F H Attix (New York: Academic) pp 427–539
- Rogers D W O, Faddegon B A, Ding G X, Ma C-M, Wei J S and Mackie T R 1995 BEAM: a Monte Carlo code to simulate radiotherapy treatment units *Med. Phys.* **22** 503–25
- Shortt K R, Ross C K, Bielajew A F and Rogers D W O 1986 Electron beam dose distributions near standard inhomogeneities *Phys. Med. Biol.* **31** 235–49
- Takahashi S 1965 Conformation radiotherapy-rotation techniques as applied to radiography and radiotherapy of cancer *Acta Radiol. Suppl.* **242** 1–142
- Wang L, Chui C and Lovelock M 1998 A patient-specific Monte Carlo dose-calculation method for photon beams *Med. Phys.* **25** 867–78
- Webb S 1992 Optimization by simulated annealing of three-dimensional conformal treatment planning for radiation fields defined by multi-leaf collimator: II. Inclusion of two-dimensional modulation of x-ray intensity *Phys. Med. Biol.* **37** 1689–704
- 1997 *The Physics of Conformal Radiotherapy: Advances in Technology* (Bristol: Institute of Physics Publishing)
- Yu C X, Symons J M, Du M N, Martinez A A and Wong J W 1995 A method for implementing dynamic photon beam intensity modulation using independent jaws and multileaf collimators *Phys. Med. Biol.* **40** 769–87
- Zackrisson B and Karlsson M 1996 Matching of electron beams for conformal therapy of target volumes at moderate depths *Radiother. Oncol.* **3** 261–70
- Zhang G G, Rogers D W O, Cygler J E and Mackie T R 1999 Monte Carlo investigation of electron beam output factors versus size of square cutout *Med. Phys.* **26** 743–50

Validation of a Monte Carlo dose calculation tool for radiotherapy treatment planning

J S Li, T Pawlicki, J Deng, S B Jiang, E Mok and C-M Ma

Department of Radiation Oncology, Stanford University School of Medicine, Stanford, CA 94305, USA

E-mail: jsli@reyes.stanford.edu

Received 2 March 2000, in final form 26 June 2000

Abstract. A new EGS4/PRESTA Monte Carlo user code, MCDOSE, has been developed as a routine dose calculation tool for radiotherapy treatment planning. It is suitable for both conventional and intensity modulated radiation therapy. Two important features of MCDOSE are the inclusion of beam modifiers in the patient simulation and the implementation of several variance reduction techniques. Before this tool can be used reliably for clinical dose calculation, it must be properly validated. The validation for beam modifiers has been performed by comparing the dose distributions calculated by MCDOSE and the well-benchmarked EGS4 user codes BEAM and DOSXYZ. Various beam modifiers were simulated. Good agreement in the dose distributions was observed. The differences in electron cutout factors between the results of MCDOSE and measurements were within 2%. The accuracy of MCDOSE with various variance reduction techniques was tested by comparing the dose distributions in different inhomogeneous phantoms with those calculated by DOSXYZ without variance reduction. The agreement was within 1.0%. Our results demonstrate that MCDOSE is accurate and efficient for routine dose calculation in radiotherapy treatment planning, with or without beam modifiers.

(Some figures in this article are in colour only in the electronic version; see www.iop.org)

1. Introduction

With the rapid development of computer technology, the Monte Carlo technique, currently the most accurate method for dose calculation (Shortt *et al* 1986, Mackie 1990, Rogers and Bielajew 1990, Andreo 1991, Mackie *et al* 1994, DeMarco *et al* 1998, Ma *et al* 1999a), is becoming more practical for use in radiation therapy treatment planning systems. It has been argued that the outcome of radiation therapy treatment may be improved by using Monte Carlo dose calculation (Mohan 1997, Nahum 1997), especially for intensity modulated radiotherapy (IMRT) treatment planning (Jeraj and Keall 1999, Ma *et al* 1999a, 2000a, b). The Monte Carlo method is being developed for treatment planning dose calculations by several groups (Mackie 1990, Hartmann-Siantar *et al* 1997, Ma *et al* 1997, 1999a, DeMarco *et al* 1998, Wang *et al* 1998, Mubata *et al* 1998, Libby *et al* 1998, Faddegon *et al* 1998).

At present, there are several general-purpose Monte Carlo codes in widespread use for radiation transport simulation, e.g. Electron Gamma Shower version 4 (EGS4) (Nelson *et al* 1985), ETRAN/ITS (Berger and Seltzer 1987) and Monte Carlo *N*-particle (MCNP) (Hendricks 1994) and PENELOPE (Salvat *et al* 1996). It is well known that the EGS4 code system is very well documented and it has been thoroughly benchmarked in the energy region of dosimetric interest (Rogers 1984a, b, Rogers and Bielajew 1984, 1986, 1990). DOSXYZ is

an EGS4 based Monte Carlo simulation code for calculation dose distribution in a rectilinear voxel phantom (Rogers *et al* 1995, Ma *et al* 1995). It is also well benchmarked. Comparisons of the DOSXYZ results with measurements have been reported previously (Rogers *et al* 1995, Kapur *et al* 1998, Ma 1998, Zhang *et al* 1999, Ma *et al* 1999a, 2000a). Unfortunately, these codes are too slow to be acceptable for routine dose calculation in treatment planning systems with existing hardware. Some codes based on the Monte Carlo method have been developed to speed up the dose calculation, such as Macro Monte Carlo (MMC) (Neuenschwander and Born 1992, Neuenschwander *et al* 1995), Voxel Monte Carlo (VMC and XVMC) (Kawrakow *et al* 1996, Fippel 1999) and Super Monte Carlo (SMC) (Keall and Hoban 1996a). Further verification and improvements are needed for routine treatment planning dose calculations.

A new EGS4/PRESTA (Bielajew and Rogers 1987) user code, MCDOSE, has been developed for routine clinical dose calculation (Ma *et al* 1999b, 2000c). MCDOSE was designed as a dose calculation module for easy implementation in a radiotherapy treatment planning system. We have implemented it in an existing commercial RTP system for conventional photon/electron beams (Ma *et al* 1999a) and intensity modulated radiotherapy (IMRT) dose verification (Ma *et al* 2000a). MCDOSE shares similar structure and geometry definition with other EGS4 user codes, such as DOSXYZ. MCDOSE and DOSXYZ have some common features. They can both simulate the transport of photons and electrons (and positrons) in a 3D rectilinear phantom geometry. The volume elements (voxels) in the phantom can have uniform or variable dimensions and the material in the voxel can be specified by the user or determined from the electron density data derived from the patient CT data. Source models are supported in both codes. But there are other features in MCDOSE, which are absent in DOSXYZ:

- (a) Advanced multiple-source models (Ma *et al* 1997, Ma 1998, Deng *et al* 2000, Jiang *et al* 2000a, b) are used as source input for both photon and electron beams in MCDOSE. The multiple-source models implemented in MCDOSE are more accurate and flexible, and easy for commissioning.
- (b) Beam modifiers such as jaws, wedges, blocks, compensators, electron cutouts and bolus are included by MCDOSE in the patient simulation. Both static and dynamic MLC fields can be simulated for conventional and intensity modulated radiotherapy.
- (c) Several variance-reduction techniques have been implemented in MCDOSE. Both codes have range rejection. However, it was implemented in different ways and in different simulation procedures.
- (d) There is an option for selecting the geometry coordinates from two definitions in MCDOSE. One (x, y, z) is the same as that in DOSXYZ for phantom study. The other (x', y', z') is for convenient patient dose calculation corresponding to the treatment system. The relationship between the two coordinates is $x = x'$, $y = -z'$ and $z = y'$.
- (e) Beamlets dose calculation for Monte Carlo inverse planning can be performed by MCDOSE for both photon and electron beams.
- (f) MCDOSE can produce dose volume histograms (DVH) using the patient contour information.

The inclusion of beam modifiers and the implementation of variance reduction techniques makes MCDOSE more practical for routine dose calculation. Beam modifiers play an important role in radiotherapy treatment. They modify the beam shape and/or intensity distribution and therefore change the dose distribution in the patient. They need to be considered for treatment planning dose calculations. It is not sufficient to treat jaws and blocks as apertures and to change the profile using the wedge or compensator factors conventionally. The effect of beam modifiers has been studied by Schach von Wittenau *et al* (2000). It was found

that the scattered electrons generated in jaws could increase the surface dose by several per cent depending on the beam energy and field size. The photon transmission and bremsstrahlung generated in the modifiers need to be considered. To ensure simulation accuracy, these beam modifiers should be simulated with accurate geometry when the Monte Carlo method is used for routine dose calculation. Some codes, like BEAM and PEREGRINE (Walling *et al* 1998), can be used to simulate beam modifiers. But BEAM can only simulate them separately from patient dose calculation. One has to simulate particle transport in the beam modifiers using BEAM first. After scoring the phase space below the modifiers, dose calculation in the patient phantom can then be performed (Ma *et al* 1999a). This two-step method works well but is inconvenient and can be time-consuming. It is not suitable for routine dose calculations. The inclusion of beam modifiers into the patient dose calculation simplifies the simulation procedure in terms of simulation steps and intermediate data storage. Although Monte Carlo is an accurate method, the CPU time needed to perform statistically meaningful dose calculation is always a problem that prevents it from being applied in routine dose calculations. The variance reduction techniques implemented in MCDOSE generally speed up the dose calculation by a factor of 10–30 (Ma *et al* 2000c). This makes the code more practicable for routine application. The dose calculation using MCDOSE for a nine-field IMRT plan (including pre- and post-optimization dose calculation) can be finished in 1 to 4 h on a 450 MHz Pentium III personal computer (Pawlicki *et al* 1999, Ma *et al* 2000b).

Before MCDOSE can be used reliably for clinical dose calculation, it must be extensively validated. The accuracy of the dose calculation depends on the input beam data and the implementation of the user code. Source modelling and beam commissioning have been investigated by Ma *et al* (1997), Ma (1998), Deng *et al* (2000) and Jiang *et al* (2000a, b). Excellent agreement in dose distributions in both homogeneous and heterogeneous phantoms has been achieved between source model, phase space data and measurements. In this work, we focus on the validation of the user code for beam modifiers and variance reduction techniques. The geometry description for beam modifiers and the implementation of variance reduction techniques may affect the simulation accuracy of the code.

The validation of beam modifiers was performed by comparing the simulation results of MCDOSE with those of BEAM/DOSXYZ. The dose distributions in specifically designed homogeneous and inhomogeneous phantoms with different source inputs calculated using MCDOSE and DOSXYZ are presented. Machine data for two Varian accelerators, Clinac 2100C and 2300C/D, were measured as required by the commissioning procedure.

2. Materials and methods

2.1. Simulation of beam modifiers in MCDOSE

In this work, we have implemented beam modifier simulation in MCDOSE. The combination of the modifiers, the geometry parameters and materials can be input by the user. Several different modifiers can be used together. Each of them occupies a slab. For photon beams our multiple-source model covers all the fixed components above the jaws in the accelerator head (Deng *et al* 2000). What we need to consider for routine dose calculations are the jaws, wedges, blocks, compensators, MLC and bolus. For electron beams our multiple-source model covers all the components down to the lowest scraper of the applicator (Jiang *et al* 2000a). Only the electron cutout and bolus need to be considered in MCDOSE.

The x and y jaws are modelled as two pairs. The inner surface of each jaw focuses to the target. The input parameters are x_1 , x_2 , y_1 , y_2 and the material for the jaws. Here x_1 , x_2 , y_1 , y_2 specify the locations of the inner edges of the jaw bars. They correspond to the field size at 100 cm SSD. A schematic diagram for the jaws is shown in figure 1(a).

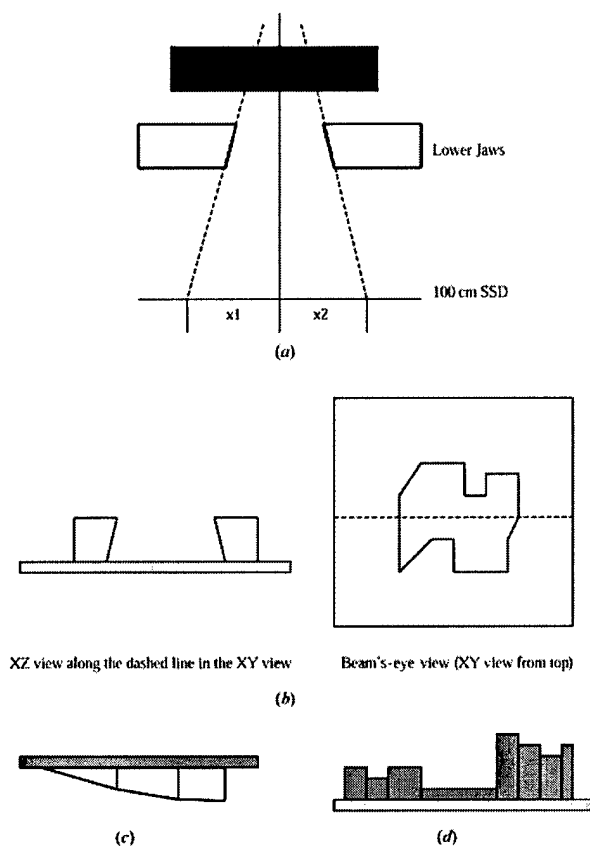


Figure 1. Schematic diagram of the beam modifiers simulated in MCDOSE. (a) X and Y jaws. (b) Photon beam block with tray. (c) Wedge and tray. (d) Compensator and tray.

To simulate the treatment block and the tray, the location, thickness and material of the block and the tray are required. The location is defined as the distance to the isocentre from the bottom surface of the block tray. The user also needs to specify the opening by the coordinates of the vertices that are projected at 100 cm SSD. The planes defining the inner surfaces of the opening are all angled with respect to the Z-axis towards the target as a single focus point. The block opening can be of any shape. The user needs to input the points continuously around the perimeter of the opening. The beam's eye view and X-Z view of the block and tray are shown in figure 1(b).

Wedges can be simulated by MCDOSE using the geometry information about the orientation, location, material and the two-dimensional point coordinates to specify its shape (see figure 1(c)). Full simulation of the particle transport is performed. This approach is similar to the wedge definition for conventional dose calculation algorithms, except for one important point. For the Monte Carlo approach, the user enters the exact wedge specifications without any modifications or adjustments in the parameters so that the final dose calculation matches the measured dose profiles of the wedge under consideration. Thus, in our Monte Carlo approach, the physical transport of particles in the beam modifiers and the

reproduction of the phase space must be accurate to obtain good agreement with measured results.

The compensator including the tray can be simulated by MCDOSE. The location, material and the tray thickness are required. The compensator is divided into different bins in two directions. The coordinates and thickness for each bin (a pixel) are required. An X-Z view of the compensator and tray is shown in figure 1(d). This module can also be used as an MLC after setting the tray material to air.

An electron cutout is simulated in a way similar to a photon block except that it does not have a tray. The option to have a diverging or straight and parallel inner planes to define the opening is considered for different clinical applications. The location, material and coordinates of each vertex to specify the opening are required.

The bolus is simulated by adding an extra layer of material to the patient's geometry (outside the patient external contour) according to its material and thickness.

2.2. Simulation of beam modifiers by EGS4/BEAM

In order to validate the code for beam modifier simulation in MCDOSE, EGS4/BEAM was used to simulate block, wedge, compensator and electron cutout. The simulations started with the phase space above the jaws. No variance reduction techniques were used in these simulations. The cut-off energy of electron and photon were set to be 700 keV and 10 keV (total energy). After the phase space data were obtained below the modifiers, DOSXYZ was used to carry out the dose calculation. Comparison between them can prove that our implementation for the simulation of beam modifier is right.

Two component modules, BLOCK and SLABS, were used to simulate the photon blocks and the trays. To simulate the wedge, the left bars of two or more pairs of JAWS were piled up to match the shape. The component modules MLC and SLABS were used to simulate the compensators and trays. The component BLOCK was used to simulate an electron cutout with the phase space above the last scraper as source input. Five subregions were used to specify a butterfly shape for the opening that was simulated for an electron cutout in this paper. The phase space data were scored below the modifiers. Then dose calculations were performed using DOSXYZ in a water phantom.

2.3. Variance reduction techniques and dose calculation details

The goal of MCDOSE is to perform quick and accurate dose calculation for radiation therapy treatment planning. Several variance reduction techniques have been implemented in MCDOSE to speed up the calculation without losing accuracy. These techniques include electron range and region rejection, photon interaction forcing, particle splitting, Russian roulette (Bielajew and Rogers 1988) and electron track repeating (Kawrakow *et al* 1996, Keall and Hoban 1996b). To speed up the simulation in beam modifiers, the electron region rejection technique was applied to the electrons that make little contribution to the dose. For example, when we transport particles in jaws and blocks, we have an option to transport electrons only in a margin around the opening. Variable global cut-off energy (ECUT) has been applied to different regions. The techniques of photon interaction forcing, splitting and Russian roulette are well known and are implemented in some codes, such as BEAM/EGS4 system. They were well described by Bielajew and Rogers (1988) and Rogers *et al* (1995). Electron track repeating is similar to a technique called correlated sampling (Ma and Nahum 1993), in which particle tracks were repeated in different locations or geometries to improve computation efficiency. It was described in great detail by Kawrakow *et al* (1996) and Keall and Hoban (1996b). The main

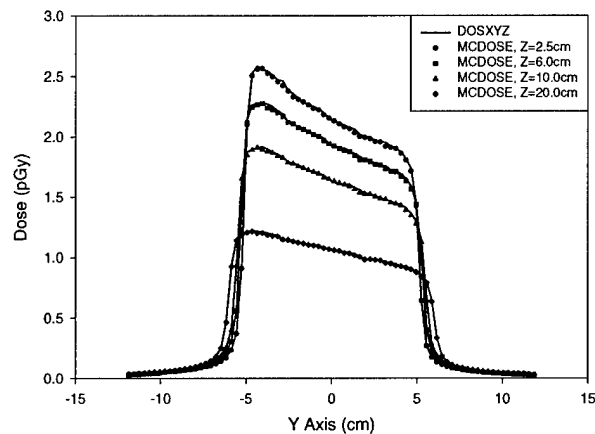


Figure 2. Comparisons of the lateral dose profiles at different depths in a water phantom between MCDOSE and BEAM/DOSXYZ. A 45° wedge were simulated for a 15 MV photon beam, the field size was 10 cm × 10 cm defined at 100 cm SSD.

idea is to simulate an electron in a standard phantom such as in water or tissue, recording all the information of the electron transport tracks including the step length, direction, energy deposition, type of collision and generated particles for each step, then repeat the tracks for other electrons with the same energy starting from a different location in the patient. The initial direction for each electron may be different. The length of every step in the electron track is inversely proportional to the material density at that location. Stopping power ratio and scattering power ratio for different materials need to be considered to scale the path lengths and multiple scattering angles. This technique saves the sampling time for multiple scattering and collision for all the repeated electrons but not for the initial one. How many times to repeat the tracks depends on the problem. The number may affect the final efficiency. Our goal was to integrate this technique efficiently with other techniques mentioned above to produce a fast Monte Carlo code. For example, when photons go into the phantom, they are split and forced to have same interactions at different locations. Many electrons are generated and their tracks are repeated at these locations. So time is saved because we do not perform initial simulation for all the electrons. Russian roulette is applied to reduce the number of scattering photons.

To ensure the accuracy of the dose calculation with MCDOSE, specially designed inhomogeneous phantoms, such as layered-lung or layered-bone phantoms, are used. The dose distributions (depth dose curves and lateral dose profiles) calculated by MCDOSE and DOSXYZ for different photon beams and electron beams are compared. DOSXYZ was selected for comparison with MCDOSE because it has already been tested thoroughly and it is also an EGS4 user code. Agreement between MCDOSE and DOSXYZ means that the beam modifier implementation in MCDOSE is correct and the application of variance reduction techniques does not affect the accuracy. Since DOSXYZ has been well benchmarked by other investigators and our previous work (Rogers *et al* 1995, Kapur *et al* 1998, Ma 1998, Zhang *et al* 1999, Ma *et al* 1999a, 2000a), it is not necessary to compare all the MCDOSE results with measurements. In this work, both monoenergetic photon beams and realistic clinical beams of Varian 2300C/D are studied. The goal for use of monoenergetic photon beams is to make sure that the code works well for monoenergetic beams (therefore it should also work

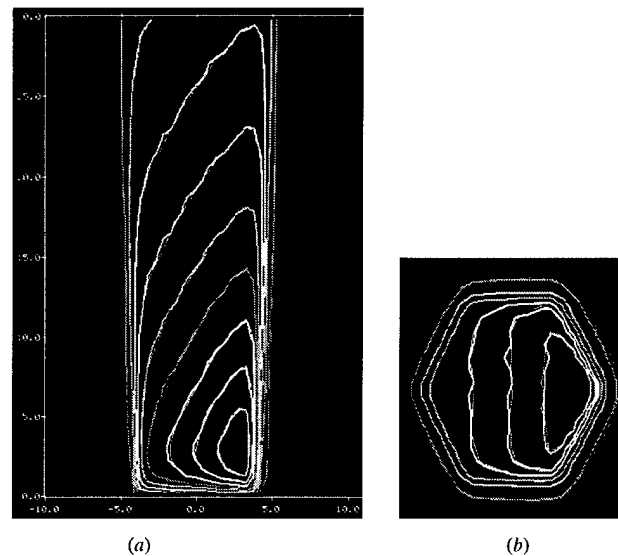


Figure 3. Dose distributions in a water phantom calculated by MCDOSE (thin curve) and BEAM/DOSXYZ (thick curve) for a $10\text{ cm} \times 10\text{ cm}$ field of a 15 MV photon beam. The beam was modified by a hexagonal block and a 60° wedge. (a) The isodose distribution in the X-Z plane through the central axis (beams come from the bottom). (b) The isodose distribution in the X-Y plane at a depth of 3.5 cm.

for polyenergetic beams). This test was done thoroughly in the energy range of interest for dosimetry with an interval of 1 MeV.

3. Results

3.1. Validation of beam modifiers

3.1.1. A 45° wedge. Figure 2 shows the lateral dose profiles at different depths in a water phantom calculated using MCDOSE and BEAM/DOSXYZ for a 45° wedge. Lead was used as the wedge material. The field size was set to $10\text{ cm} \times 10\text{ cm}$ at 100 cm SSD. The voxel size in the water phantom was $1.0\text{ cm} \times 0.3\text{ cm} \times 0.5\text{ cm}$. A 15 MV photon beam from a Varian Clinac 2300C/D machine was used as source input with phase space scored above the jaws. The comparison calculations were performed under the same conditions. The agreement between the results of MCDOSE and BEAM/DOSXYZ is within 1% of the maximum dose. The CPU time comparison between MCDOSE and BEAM/DOSXYZ is shown in table 1. MCDOSE is about 16 times faster than BEAM/DOSXYZ for this simulation.

3.1.2. A hexagonal block and a 60° wedge. Figure 3 shows the dose distributions calculated by MCDOSE and BEAM/DOSXYZ in a water phantom with a hexagonal block and a 60° wedge for a $10\text{ cm} \times 10\text{ cm}$ field of a 15 MV photon beam. The block was made of Cerrobend and its thickness was 7.7 cm. The block tray was made of PMMA and its thickness was 0.7 cm. The wedge was made of lead. The voxel size in the water phantom was $0.5\text{ cm} \times 0.5\text{ cm} \times 0.5\text{ cm}$. Figure 3(a) shows the isodose distribution in the X-Z plane through the central axis and figure 3(b) shows the isodose distribution in the X-Y plane at a depth of 3.5 cm. The difference between the results of MCDOSE and BEAM/DOSXYZ is within 1% of the maximum dose.

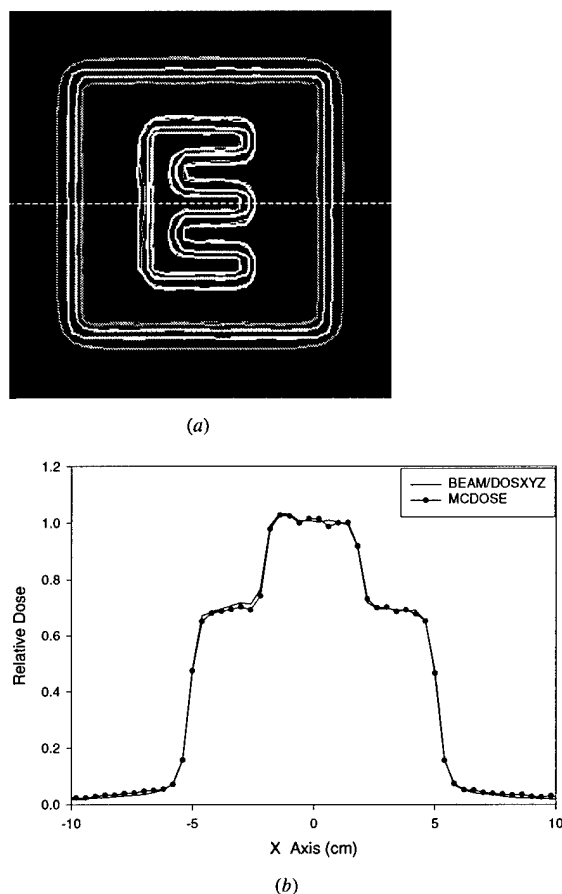


Figure 4. (a) The isodose distributions in *XY* view at a depth of 2.5 cm in a water phantom for a modified 10 cm \times 10 cm 15 MV photon beam using a specially designed compensator. The thick curve is the simulation result of BEAM/DOSXYZ. The thin curve is the result of MCDOSE. (b) The lateral dose profile along the dashed line in (a). The curve with symbols in (b) is the result of MCDOSE.

Table 1. The CPU time (hours) required by MCDOSE and BEAM/DOSXYZ for the beam modifier simulation investigated in this work on a Pentium III 450 MHz personal computer. The statistical uncertainties of the maximum doses are 1%.

	Modifier			
	45° wedge	60° wedge/block	E-shaped compensator	Butterfly-shaped electron cutout
BEAM + DOSXYZ	31.5 \pm 6.1	247.5 \pm 7.9	10.3 \pm 10.9	37.9 \pm 1.4
MCDOSE	2.3	13.0	5.3	2.5
Ratio	16.3	19.4	4.0	15.7

The CPU time needed by MCDOSE and BEAM/DOSXYZ is given in table 1. MCDOSE is about 19 times faster than BEAM/DOSXYZ for this simulation.

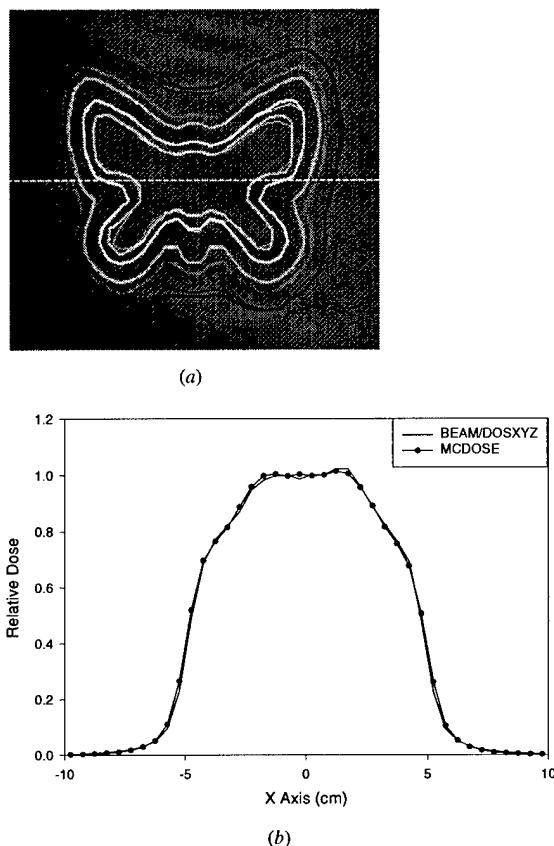


Figure 5. (a) is the isodose distributions in *XY* view at a depth of 2.25 cm in a water phantom for a modified 10 cm \times 10 cm 12 MeV electron beam using an electron cutout with a butterfly-shaped opening. The thick curve is the simulation result of BEAM/DOSXYZ. The thin curve is the result of MCDOSE. (b) The lateral dose profile along the dashed line in (a). The curve with symbols in (b) is the result of MCDOSE.

3.1.3. Compensator. Figure 4 shows the E-shaped compensator isodose distributions (a) and lateral dose profiles (b) at a depth of 2.5 cm in the water phantom. They were calculated using MCDOSE and BEAM/DOSXYZ respectively. The compensator was made of copper. The thickness in the area of the compensator forming the 'E' shape was 0.5 cm and the thickness in the remaining area was 2 cm. The voxel size in the water phantom was 0.4 cm \times 0.4 cm \times 1.0 cm. Agreement (within 1%) can be observed from the comparison. In the penumbra regions, the separation between the results of MCDOSE and BEAM/DOSXYZ is within 1 mm. The CPU time needed by MCDOSE and BEAM/DOSXYZ is also shown in table 1. MCDOSE is about four times faster than BEAM/DOSXYZ for this simulation.

3.1.4. Electron cutout. Figure 5 shows the isodose distributions (a) and lateral dose profiles (b) in a water phantom calculated using BEAM/DOSXYZ and MCDOSE, for a 12 MeV realistic electron beam from a Varian 2100C machine with a butterfly-shaped cutout. The cutout was made of Cerrobend and its thickness was 1.4 cm. The voxel size in the water phantom

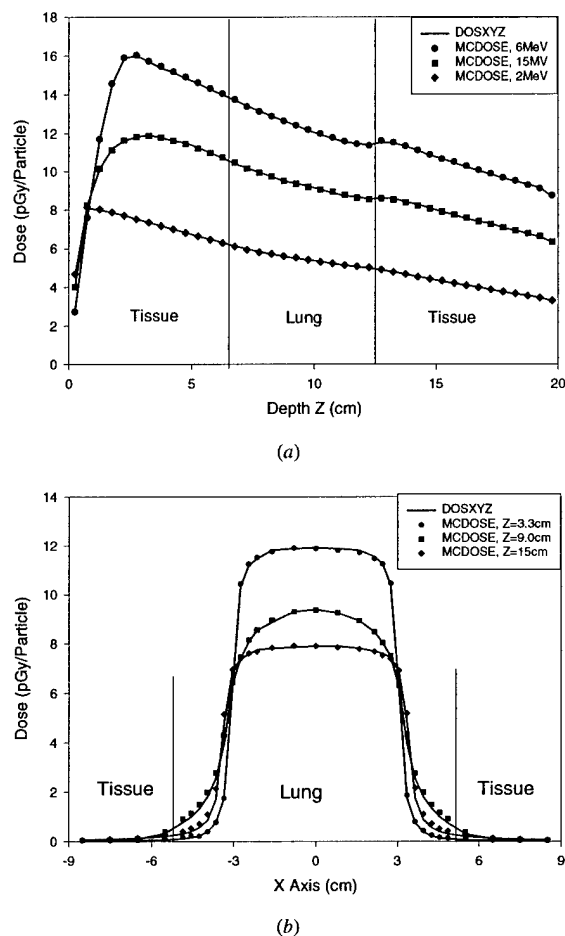
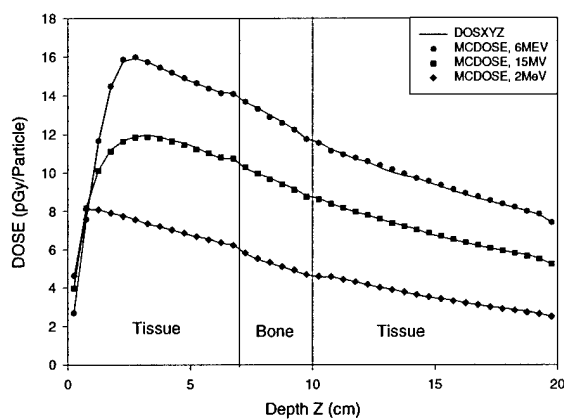


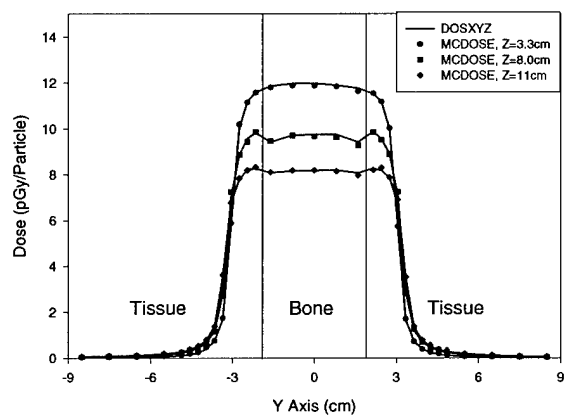
Figure 6. Dose distribution in a tissue–lung–tissue phantom calculated by DOSXYZ and MCDOSE for 6 MeV, 15 MV and 2 MeV photon beams with field size of 6 cm × 6 cm defined at 100 cm SSD. The material in the volume of –5.0 cm to 5.0 cm along the *X* direction, –2.0 cm to 2.0 cm along the *Y* direction and 7.0 cm to 12.5 cm along the *Z* direction is lung. (a) The depth dose curves along the central axis for the beams. (b) The lateral dose profiles along the *X*-axis at depths of 3.3 cm, 9.0 cm and 15.0 cm for the 15 MV photon beam.

was 0.5 cm × 0.5 cm × 0.3 cm. The phase space of an electron beam above the last scraper of a 10 cm × 10 cm applicator was used as the source input. Good agreement (within 1%) has been achieved between the results of MCDOSE and BEAM/DOSXYZ. In the penumbra regions, the separation between MCDOSE and BEAM/DOSXYZ is within 1 mm. The CPU time needed by MCDOSE and BEAM/DOSXYZ is shown in table 1. MCDOSE is about 16 times faster than BEAM/DOSXYZ for this simulation.

The electron beam cutout factors calculated using MCDOSE are compared with the published data in table 2. The published data were calculated using BEAM/DOSXYZ with full phase space input and measured by Kapur *et al* (1998). The difference between the MCDOSE data and those calculated with full phase space by DOSXYZ is within 1.0%. The differences



(a)



(b)

Figure 7. Dose distributions in a tissue-bone-tissue phantom calculated by DOSXYZ and MCDOSE for 6 MeV, 15 MV and 2 MeV photon beams with field size of $6\text{ cm} \times 6\text{ cm}$ defined at 100 cm SSD. The material in the volume of -5.0 cm to 5.0 cm along the X direction, -2.0 cm to 2.0 cm along the Y direction and 7.0 cm to 10.0 cm along the Z direction is bone. (a) The depth dose curve along the central axis for the beams. (b) The lateral dose profiles along the Y axis at depths of 3.3 cm, 8.0 cm and 11.0 cm for the 15 MV photon beam.

in the cutout factors between MCDOSE data and measurement is less than 2% except for the cases of 20 MeV electron beams with $3\text{ cm} \times 3\text{ cm}$ and $4\text{ cm} \times 4\text{ cm}$ inserts.

3.2. Validation of dose distribution in heterogeneous phantoms

To test the accuracy of the dose distribution calculated using MCDOSE with the variance reduction techniques, comparisons are made with the results of DOSXYZ. Each example has been calculated with a source-surface distance of 100 cm and field size of $6\text{ cm} \times 6\text{ cm}$. The global electron cut-off energy (ECUT) was set to 700 keV and photon cut-off energy (PCUT) was set to 10 keV in MCDOSE and DOSXYZ. The maximum fractional energy loss per electron step (ESTEPE) was limited to 4% for both codes. The material compositions and

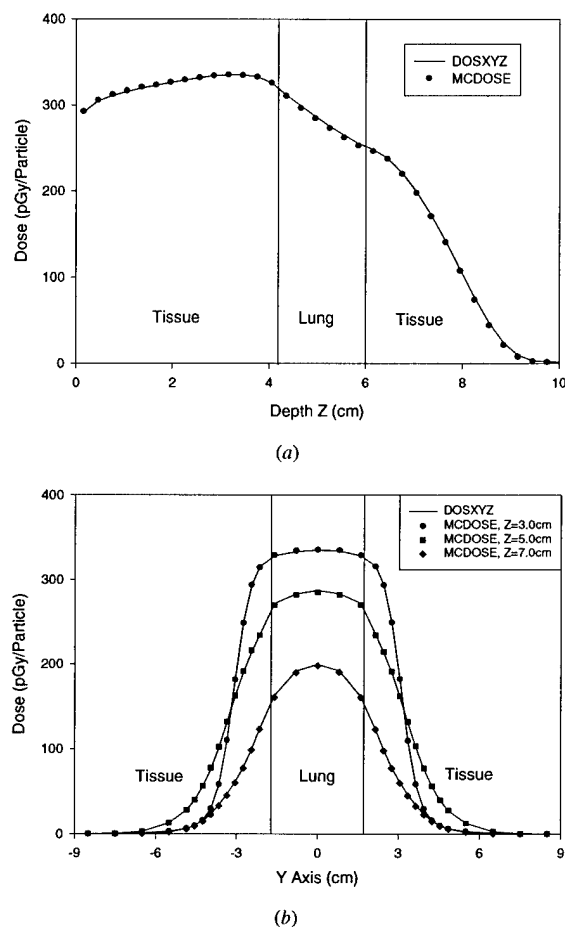


Figure 8. Dose distributions in a tissue-lung-tissue phantom calculated by DOSXYZ and MCDOSE for a 15 MeV electron beam with field size 6 cm \times 6 cm. The material in the volume of -5.0 cm to 5.0 cm along the *X* direction, -2.0 cm to 2.0 cm along *Y* direction and 4.2 cm to 6.0 cm along the *Z* direction is lung. (a) The depth dose curve along the central axis. (b) The lateral dose profiles along the *Y*-axis at depths of 3.0 cm, 5.0 cm and 7.0 cm.

densities are taken from ICRU (1992). Monoenergetic point sources and phase space files for a 15 MV photon beam of a Varian Clinac 2300C/D linear accelerator were used. Since dose per incident fluence is calculated, absolute dose comparisons are made between MCDOSE and DOSXYZ.

3.2.1. Photon beams. Figure 6(a) shows the depth dose curves along the central axis for 6 MeV and 2 MeV monoenergetic photon beams calculated by DOSXYZ and MCDOSE in a tissue phantom with 3D lung inhomogeneity. At depths from 7 cm to 12.5 cm, the phantom contains a 10 cm \times 4 cm slab of lung in the centre. The depth dose curves for a realistic 15 MV photon beam from a Varian Clinac 2300C/D accelerator calculated by DOSXYZ and MCDOSE in the same phantom are also shown in figure 6(a) and the lateral dose profiles at

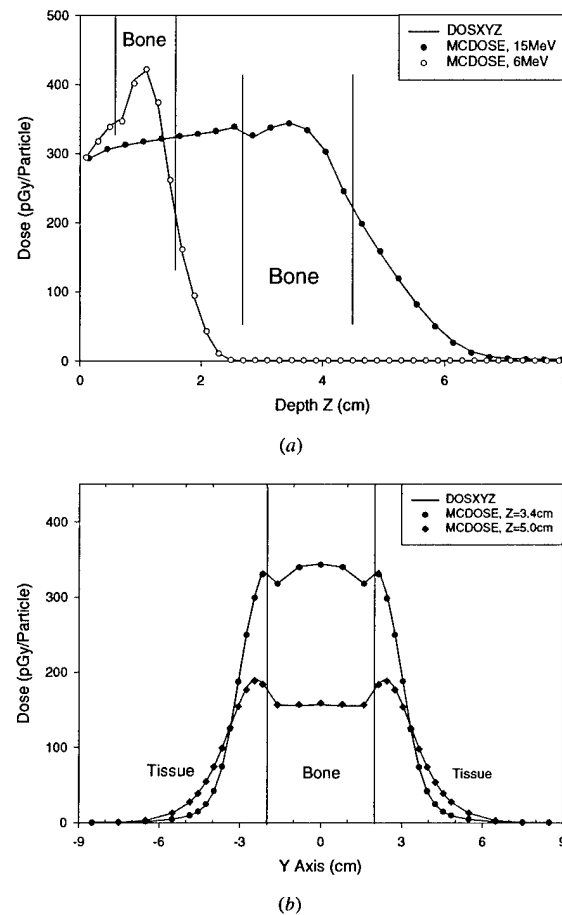


Figure 9. Dose distribution in tissue-bone-tissue phantoms calculated by DOSXYZ and MCDOSE for 15 MeV and 6 MeV electron beams with field size 6 cm \times 6 cm. For the 15 MeV electron beam, the material in the volume of -5.0 cm to 5.0 cm along the X direction, -2.0 cm to 2.0 cm along the Y direction and 2.7 cm to 4.5 cm along the Z direction is bone. For the 6 MeV electron beam, the material in the volume of -5.0 cm to 5.0 cm along the X direction, -2.0 cm to 2.0 cm along the Y direction and 0.6 cm to 1.6 cm along the Z direction is bone. (a) The depth dose curves along the central axis for two beams. (b) The lateral dose profiles along the Y axis at depths of 3.4 cm and 5.0 cm for the 15 MeV electron beam.

different depths are shown in figure 6(b). The phase space for a 15 MV photon beam was generated by BEAM and contains over 5 million particles. The 1σ statistical uncertainty on the dose values for these curves is less than 0.5%.

Dose calculations were also performed for photon beams in an inhomogeneous phantom containing tissue and bone. A 10 cm \times 4 cm slab of bone was placed between 7 cm and 10 cm depth in the centre of the tissue phantom. Figure 7(a) shows the depth dose curves along the central axis for different photon beams. Figure 7(b) shows the lateral dose profiles at different depths for a 15 MV photon beam.

Figures 6 and 7 show good agreement in dose distributions between MCDOSE and DOSXYZ for different photon beams. The absolute doses calculated by these two codes

Table 2. The electron cutout factors for various square inserts in $10 \times 10 \text{ cm}^2$ applicator for 6, 12 and 20 MeV beams calculated by MCDOSE and compared with the full phase space calculation by DOSXYZ and measurement of Kapur *et al* (1998). The values in the parentheses indicate the per cent difference between the MCDOSE calculated data and those measured or calculated with full phase space by DOSXYZ.

Energy (MeV)	Insert (cm \times cm)	MCDOSE	Full phase space	Measurement
6	3 \times 3	0.922	0.923 (−0.1%)	0.927 (−0.5%)
	4 \times 4	0.983	0.982 (0.1%)	0.988 (−0.5%)
	8 \times 8	1.009	1.005 (0.4%)	1.003 (0.6%)
12	3 \times 3	0.930	0.930 (0.0%)	0.928 (0.2%)
	4 \times 4	0.965	0.956 (0.9%)	0.963 (0.2%)
	8 \times 8	0.999	1.002 (−0.3%)	0.991 (0.8%)
20	3 \times 3	0.964	0.968 (−0.4%)	0.993 (−2.9%)
	4 \times 4	0.989	0.993 (−0.4%)	1.011 (−2.2%)
	8 \times 8	0.999	0.993 (0.6%)	1.004 (−0.5%)

in tissue, lung, bone, even at the interface between tissue and bone and tissue and lung agree to within 1% of the maximum dose. Further comparisons of dose calculations for monoenergetic photon beams from 1 MeV to 20 MeV, and also for 6 MV and 10 MV photon beams were performed. Similar agreement between MCDOSE and DOSXYZ was achieved. In most cases, the differences were within the 1σ statistical uncertainty of 1%.

3.2.2. Electron beams. We also performed dose calculations for monoenergetic point source electron beams with field size 6 cm \times 6 cm. The depth dose curves of a 15 MeV electron beam calculated by MCDOSE and DOSXYZ in a tissue–lung–tissue phantom are shown in figure 8(a). The lung material was at a depth from 4 to 6 cm. Figure 8(b) shows the lateral dose profiles at different depths in the phantom. At a depth from 4.2 to 6.0 cm, the lung material was from −5 cm to 5 cm in the *X* direction and from −2 cm to 2 cm in the *Y* direction. The remaining volume was tissue. The difference between the simulation results of MCDOSE and DOSXYZ is within 1% of the maximum dose.

The depth dose curves and lateral dose profiles at different depths for a 15 MeV electron point source beam in a tissue–bone–tissue phantom are shown in figures 9(a) and (b). At a depth from 2.7 to 4.5 cm, there was a 10 cm \times 4 cm slab of bone in the centre surrounded by tissue. The depth dose curve for a 6 MeV electron beam in a tissue–bone–tissue phantom is also shown in figure 9(a). The bone material was at a depth from 0.6 to 1.6 cm. The difference between the simulation results of MCDOSE and DOSXYZ is within 1% of the maximum dose.

3.2.3. CPU time comparison. The CPU times required by MCDOSE and DOSXYZ for dose calculations shown in figures 6 and 9 are listed in table 3 for different photon and electron beams. The calculations were performed on a Pentium III 450 MHz PC. The statistical uncertainty of the maximum dose is 1%. The ratios in the table are the speed-up factors of MCDOSE compared with DOSXYZ for each beam. In general MCDOSE is 20–50 times faster than DOSXYZ for photon beams and 5–10 times faster than DOSXYZ for electron beams.

4. Summary

A new Monte Carlo dose calculation tool has been developed and validated for clinical dose calculation. The main features of MCDOSE include electron and photon beam reconstruction

Table 3. The CPU time (hours) required by MCDOSE and DOSXYZ for the dose calculations shown in figures 6 and 9 on a Pentium III 450 MHz personal computer. The statistical uncertainties of the maximum doses are 1%.

	Beam				
	2 MeV photon	6 MeV photon	15 MV photon	6 MeV electron	15 MeV electron
DOSXYZ	9.44	2.95	4.86	0.78	0.94
MCDOSE	0.25	0.074	0.098	0.08	0.17
Ratio	37.7	39.8	49.6	9.8	5.6

by source models, simulation of beam modifiers together with the patient geometry for dose calculation and application of variance reduction techniques.

Comparisons of dose distribution with wedges, blocks, compensator and electron cutout between MCDOSE and BEAM/DOSXYZ demonstrated that dose calculation with modifiers in MCDOSE is accurate, convenient and efficient. To compare MCDOSE and DOSXYZ dose distributions, 3D heterogeneous phantoms containing lung and bone were used. Excellent agreement between the MCDOSE and DOSXYZ results has been obtained for both photon and electron beams of different energies. Comparing with DOSXYZ, the MCDOSE code runs generally 20–50 times faster for the photon beams and 5–10 times faster for electron beams investigated in this work without beam modifiers.

Acknowledgments

This work is partially supported by an NCI grant no CA 78331, a DOD grant no BC971292 and a consortium agreement with the NumeriX, LLC. We would like to thank Dr Arthur Boyer, Dr Gary Luxton and Dr Sam Brain for valuable discussions and comments on our work. We would also like to thank Todd Koumrian and Michael Luxton for computer hardware and software support.

References

- Andreo P 1991 Monte Carlo technique in medical physics *Phys. Med. Biol.* **36** 861–920
- Berger M J and Seltzer S M 1973 ETRAN, Monte Carlo code system for electron and photon transport through extended media *Documentation for RSIC Computer Package CCC-107* (Oak Ridge, TN: Oak Ridge National Laboratory)
- Bielajew A F and Rogers D W O 1987 PRESTA: the parameter reduced electron-step transport algorithm for electron Monte Carlo transport *Nucl. Instrum. Methods Phys. Res. B* **18** 165–81
- 1988 Variance-reduction techniques *Proc. Int. School of Radiation Damage and Protection Eighth Course: Monte Carlo Transport of Electrons and Photons below 50 MeV* ed T M Jenkins, W R Nelson and A Rindi (New York: Plenum) pp 407–19
- DeMarco J J, Solberg T D and Smathers J B 1998 A CT-based Monte Carlo simulation tool for dosimetry planning and analysis *Med. Phys.* **25** 1–11
- Deng J, Jiang S B, Kapur A, Li J S, Pawlicki T and Ma C-M 2000 Photon beam characterization and modelling for Monte Carlo treatment planning *Phys. Med. Biol.* **45** 411–27
- Faddegon B A, Balogh J, Mackenzie R and Scora D 1998 Clinical considerations of Monte Carlo for electron radiotherapy treatment planning *Radiat. Phys. Chem.* **53** 217–28
- Fippel M 1999 Fast Monte Carlo dose calculation for photon beams based on the VMC electron algorithm *Med. Phys.* **26** 1466–75
- Hartmann-Siantar C L *et al* 1997 Lawrence Livermore National Laboratory's PEREGRINE Project *Proc. 12th Int. Conf. on the Use of Computers in Radiation Therapy (Salt Lake City, UT)* (Madison, WI: Medical Physics Publishing) pp 19–22

- Hendricks J S 1994 A Monte Carlo code for particle transport *Los Alamos Scientific Laboratory Report* **22** 30–43
- ICRU 1992 Photon, electron, proton and neutron interaction data for body tissues *ICRU Report* **46** (Bethesda, MD: ICRU)
- Jeraj R and Keall P 1999 Monte Carlo-based inverse treatment planning *Phys. Med. Biol.* **44** 1885–96
- Jiang S B, Boyer A L and Ma C-M 2000b Modeling the extrafocal radiation and monitor chamber backscatter for photon beam dose calculation *Med. Phys.* accepted
- Jiang S B, Kapur A and Ma C-M 2000a Electron beam modelling and commissioning for Monte Carlo treatment planning *Med. Phys.* **27** 180–91
- Kapur A, Ma C-M, Mok E C, Findley D O and Boyer A L 1998 Monte Carlo calculation of electron beam output factors for a medical linear accelerator *Phys. Med. Biol.* **43** 3479–94
- Kawrakow I, Fippel M and Friedrich K 1996 3D electron dose calculation using a voxel based Monte Carlo algorithm (VMC) *Med. Phys.* **23** 445–57
- Keall P J and Hoban P W 1996a Super-Monte Carlo: a 3D electron beam dose calculation algorithm *Med. Phys.* **23** 2023–34
- 1996b Superposition dose calculation incorporating Monte Carlo generated electron track kernels *Med. Phys.* **23** 479–85
- Libby B, Siebers J and Mohan R 1998 Systematic analysis of Monte Carlo generating beam weights *Med. Phys.* **23** 965–71
- Ma C-M 1998 Characterization of computer simulated radiotherapy beams for Monte Carlo treatment planning *Radiat. Phys. Chem.* **53** 329–44
- Ma C-M, Faddegon B A, Rogers D W O and Mackie T R 1997 Accurate characterization of Monte Carlo calculated electron beams for radio-therapy *Med. Phys.* **24** 401–16
- Ma C-M, Li J S, Pawlicki T, Jiang S B and Deng J 2000c MCDOSE: a Monte Carlo dose calculation tool for radiation therapy treatment planning *Proc. 13th Int. Conf. on the Use of Computers in Radiation Therapy (Heidelberg, Germany)* (Berlin: Springer) pp 123–5
- Ma C-M, Mok E, Kapur A and Findley D 1997 Improvement of small-field electron beam dosimetry by Monte Carlo simulations *Proc. 12th Int. Conf. on the Use of Computers in Radiation Therapy (Salt Lake City, UT)* (Madison, WI: Medical Physics Publishing) pp 159–62
- Ma C-M, Mok E, Kapur A, Pawlicki T, Findley D, Brain S, Forster K and Boyer A L 1999a Clinical implementation of a Monte Carlo treatment planning system *Med. Phys.* **26** 2133–43
- Ma C-M and Nahum A E 1993 Calculation of absorbed dose ratios using correlated Monte Carlo sampling *Med. Phys.* **20** 1189–99
- Ma C-M, Pawlicki T, Jiang S B, Li J S, Deng J, Mok E, Kapur A, Xing L, Ma L and Boyer A L 2000a Monte Carlo verification of IMRT dose distributions from a commercial treatment planning optimization system *Phys. Med. Biol.* **45** 2483–95
- Ma C-M, Pawlicki T, Lee M C, Jiang S B, Li J S, Deng J, Yi B, Mok E and Boyer A L 2000b Energy- and intensity-modulated electron beams for radiotherapy *Phys. Med. Biol.* **45** 2293–311
- Ma C-M, Pawlicki T, Li J S, Jiang S B, Deng J, Kapur A, Mok E, Luxton G and Boyer A L 1999b MCDOSE—A dose calculation tool for radiotherapy treatment planning (abstract) *Med. Phys.* **26** 1148
- Ma C-M, Reckwerdt P, Holmes M, Rogers D W O, Geiser B and Walters B 1995 DOSXYZ users manual *NRCC Report PIRS-0509B*
- Mackie T R 1990 *Dosimetry of Ionizing Radiation* vol 3, ed K Kase, B Bjarnagard and F H Attix (New York: Academic) pp 541–620
- Mackie T R et al 1994 The OMEGA project: comparison among EGS4 electron beam simulations, 3D Fermi-Eyges calculations, and dose measurements *Proc. 11th Int. Conf. on the Use of Computers in Radiation Therapy (Manchester, UK)* pp 152–3
- Mohan R 1997 Why Monte Carlo? *Proc. 12th Int. Conf. on the Use of Computers in Radiation Therapy (Salt Lake City, UT)* (Madison, WI: Medical Physics Publishing) pp 16–18
- Mubata C D, Nahum A E, Rosenberg I and Bielajew A F 1998 Optimization of Monte Carlo simulation in external-beam treatment planning *Med. Phys.* **25** A185
- Nahum A E 1997 Conformal therapy needs Monte Carlo dose computation *Proc. Challenges in Conformal Radiotherapy* (Nice: European Society for Therapeutic Radiology and Oncology) pp 1–11
- Nelson W R, Hirayama H and Rogers D W O 1985 The EGS4 code system *Stanford Linear Accelerator Center Report SLAC-265* (Stanford, CA: SLAC)
- Neuenschwander H and Born E 1992 A macro Monte Carlo method for electron beam dose calculation *Phys. Med. Biol.* **37** 107–25
- Neuenschwander H, Mackie T R and Reckwerdt P J 1995 MMC: a high performance Monte Carlo code for electron beam treatment planning *Phys. Med. Biol.* **40** 543

- Pawlicki T, Jiang S B, Deng J, Li J S and Ma C-M 1999 Monte Carlo calculated beamlets for photon beam inverse planning (abstract) *Med. Phys.* **26** 1064-5
- Rogers D W O 1984a Fluence to dose equivalent conversion factors calculated with EGS3 for electrons from 100 keV to 20 GeV and photons from 11 keV to 20 GeV *Health Phys.* **46** 891
- 1984b Low energy electron transport with EGS *Nucl. Instrum. Methods A* **227** 535
- Rogers D W O and Bielajew A F 1984 The use of EGS for Monte Carlo calculations in medical physics *NRCC Report PXR-2692* (Ottawa: NRCC)
- 1986 Difference in electron depth-dose curve calculated with EGS and ETRAN and improved energy-range relationships *Med. Phys.* **13** 687-94
- 1990 *Dosimetry of Ionizing Radiation* vol 3, ed K Kase, B Bjarnagard and F H Attix (New York: Academic) pp 427-539
- Rogers D W O, Bielajew A F, Mackie T R and Kubsad S S 1990 The OMEGA project: treatment planning for electron-beam radiotherapy using Monte Carlo techniques *Phys. Med. Biol.* **35** 285
- Rogers D W O, Faddegon B A, Ding G X, Ma C-M, We J and Mackie T R 1995 BEAM—a Monte Carlo code to simulate radiotherapy treatment units *Med. Phys.* **22** 503-24
- Salvat F, Fernandez-Vera J M, Baro J and Sempau J 1996 *PENELOPE, An Algorithm and Computer Code for Monte Carlo Simulation of Electron-Photon Showers* (Barcelona: Informes Tècnics Ciemat)
- Schach von Wittenau A E, Bergstrom P M and Cox L J 2000 Patient-dependent beam modifier physics in Monte Carlo photon dose calculations *Med. Phys.* **27** 935-47
- Shortt K R, Ross C K, Bielajew A F and Rogers D W O 1986 Electron beam dose distributions near standard inhomogeneities *Phys. Med. Biol.* **31** 235-49
- Siebers J, Libby B and Mohan R 1998 Trust, but verify: comparison of MCNP and BEAM Monte Carlo codes for generation of phase space distributions for a Varian 2100C *Med. Phys.* **25** A143
- Walling R, Hartmann Siantar C, Albright N, Wiczorek D, Knapp D, Verhey L, May S and Moses E 1998 Clinical validation of the PEREGRINE Monte Carlo dose calculation system for photon beam teletherapy *Med. Phys.* **25** A128
- Wang L, Chui C and Lovelock M A 1998 A patient-specific Monte Carlo dose-calculation method for photon beams *Med. Phys.* **25** 867-78
- Zhang G G, Rogers D W O, Cygler J E and Mackie T R 1999 Monte Carlo investigation of electron beam output factors versus size of square cutout *Med. Phys.* **26** 743-50

Electron beam modeling and commissioning for Monte Carlo treatment planning

Steve B. Jiang,^{a)} Ajay Kapur, and C.-M. Ma

Department of Radiation Oncology, Stanford University School of Medicine, 300 Pasteur Drive, Stanford, California 94305-5304

(Received 19 April 1999; accepted for publication 22 October 1999)

A hybrid approach for commissioning electron beam Monte Carlo treatment planning systems has been studied. The approach is based on the assumption that accelerators of the same type have very similar electron beam characteristics and the major difference comes from the on-site tuning of the electron incident energy at the exit window. For one type of accelerator, a reference machine can be selected and simulated with the Monte Carlo method. A multiple source model can be built on the full Monte Carlo simulation of the reference beam. When commissioning electron beams from other accelerators of the same type, the energy spectra in the source model are tuned to match the measured dose distributions. A Varian Clinac 2100C accelerator was chosen as the reference machine and a four-source beam model was established based on the Monte Carlo simulations. This simplified beam model can be used to generate Monte Carlo dose distributions accurately (within 2%/2 mm compared to those calculated with full phase space data) for electron beams from the reference machine with various nominal energies, applicator sizes, and SSDs. Three electron beams were commissioned by adjusting the energy spectra in the source model. The dose distributions calculated with the adjusted source model were compared with the dose distributions calculated using the phase space data for these beams. The agreement is within 1% in most of cases and 2% in all situations. This preliminary study has shown the capability of the commissioning approach for handling large variation in the electron incident energy. The possibility of making the approach more versatile is also discussed. © 2000 American Association of Physicists in Medicine.[S0094-2405(00)03401-5]

Key words: electron beam, treatment planning, Monte Carlo simulation, beam commissioning, source modeling

I. INTRODUCTION

Electron beam radiation therapy is used extensively to treat head and neck cancers to avoid the irradiation of the spinal cord, and to treat chest walls to limit the irradiated volume of lung. The currently available commercial systems for electron treatment planning mostly utilize the Hogstrom algorithm as the dose calculation engine,¹ which is based on Fermi-Eyges theory.^{2,3} Due to the inappropriate treatment of electron transport in inhomogeneous phantoms, large discrepancies (10% or more) in the dose distributions have been observed between the current analytical algorithms and measurements or Monte Carlo simulations in some clinical situations where the treatment volumes encompass air cavities and bone.⁴⁻⁷ Accurate dose calculation is an important factor for the widespread clinical use of electron therapy and the development of new electron therapy techniques, such as electron beam or mixed electron/photon beam intensity modulated therapy, which are expected to improve the conformality of the delivered dose distribution to the target volume for some disease sites.⁸⁻¹⁰

The Monte Carlo method is generally considered to be the most accurate approach for electron dose calculation under all circumstances.¹¹⁻¹⁶ In particular, Monte Carlo simulation can handle electron multiple scattering in the presence of inhomogeneities (such as bone and air cavity) much more

accurately than any existing analytical dose models. The necessity of accurate electron dose calculation has motivated many efforts to develop Monte Carlo electron beam treatment planning systems.^{6,7,17-22} Due to the rapid development of computer technology and the employment of innovative variance reduction techniques, it is expected that treatment planning systems utilizing a Monte Carlo dose engine will begin to serve in routine clinical practice in the next few years.^{6,7,20-29}

The commissioning procedure for a Monte Carlo treatment planning system can be different from that for a conventional planning system, since it requires more detailed and accurate clinical beam data.²² For example, the phase space information (position, direction and energy) is needed to represent particles coming out of the accelerator treatment head. This information is extremely difficult, if not impossible, to acquire experimentally, mainly due to the very high intensity of the therapeutic electron beam.³⁰ Some researchers tried to extract the phase space information from the limited set of measured dose data (such as depth dose curves and dose profiles) by using a simple beam model.³¹ Although the approach may have great potential, at least currently it uses many approximations and the accuracy of the reconstructed phase space cannot be guaranteed. The only method to obtain the accurate electron beam phase space

information is to simulate the accelerator treatment head using the Monte Carlo method.³²⁻³⁴ An EGS4 Monte Carlo user code, OMEGA BEAM, was developed specifically for this purpose.³⁴ Using the BEAM code, the accelerator treatment head and electron applicator can be simulated to yield a data file containing the phase space information for tens of millions of particles exiting the treatment head. The phase space data can then be used as input to calculate dose distributions in a patient's CT phantom.³⁴

However, direct simulation of the accelerator treatment head using the Monte Carlo method is not a viable commissioning approach for Monte Carlo treatment planning. The beam characteristics are usually different due to variation in accelerator designs and on-site beam tuning. The simulated electron beam phase space for one accelerator may not be used directly for another. It is necessary to simulate each accelerator individually to obtain the phase space information. This fact presents three problems for the clinical acceptance of Monte Carlo treatment planning systems. First, the simulation of the accelerator treatment head for every energy/applicator combination takes much more time than the commissioning of a conventional electron planning system. As estimated by Faddegon *et al.*,²² even for users with Monte Carlo simulation experience, it takes about two months of CPU time to generate a complete set of beam data for a single accelerator. Second, the storage of the phase space information requires a lot of computer disk space. For each energy/applicator combination, a phase space file is usually pre-calculated and stored in the treatment planning computer. For accurate treatment planning, a phase space file occupies hundreds of megabytes of disk space. This is certainly a substantial burden for the computer resources at most clinical centers. Third, the generation and quality assurance of the phase space data files by simulating the treatment head requires Monte Carlo simulation experience. Therefore, it is a prohibitive task for general users to perform Monte Carlo simulations for their own accelerators.

In this paper, a hybrid approach for commissioning electron beam Monte Carlo treatment planning systems is proposed. This method combines the advantages of the full Monte Carlo simulation and the method of Janssen *et al.*³¹ It is based on the assumption that accelerators of the same type have very similar electron beam characteristics and the major difference is the electron incident energy at the exit window due to beam tuning during linac acceptance. By simulating a reference accelerator for a particular type of accelerator using the Monte Carlo BEAM code,³⁴ a beam model is constructed using the resultant phase space information. The beam model is a simplified implementation of a previously developed multiple source model which can compress the Monte Carlo phase space data by a factor of 1000 or more.³⁵⁻³⁷ When commissioning another accelerator of the same type, the energy spectra in the beam model are tuned to match standard measured data such as depth doses and dose profiles. Using this approach, we do not have to simulate every accelerator individually. Only one reference accelerator needs to be simulated for a type of accelerator, and this can be done carefully by someone with Monte Carlo exper-

tise. In this paper, a Varian Clinac 2100C accelerator is chosen as the reference machine. The machine is simulated using the BEAM code³⁴ and a four-source beam model is established based on the simulated beam phase space information. The accuracy of the Monte Carlo dose distributions calculated with the model is verified. Then, the model based on the reference beam is used to commission three other electron beams. Two beams are also from the reference machine but with incident energies significantly different from that of the reference beam. The third beam is from another Clinac 2100C machine at a different institution.³⁸ The validity of the proposed commissioning approach is demonstrated by commissioning these three beams.

II. METHODS AND MATERIAL

A. Beam modeling

1. General considerations

Beam modeling is the first step in our hybrid commissioning procedure for a Monte Carlo treatment planning system. A beam model for a type of accelerator is established using the Monte Carlo simulated phase space information for the reference beam. The beam data are modeled using the multiple source model developed by Ma *et al.*,³⁵⁻³⁷ which is modified in the current work for use in the commissioning procedure. The major modifications of the model are discussed here.

The multiple source model is based on the observation that particles from different components of an accelerator have significantly different energy, angular, and spatial distributions, while the particles from the same component have very similar characteristics.³⁵⁻³⁷ Therefore, the particles from different components of an accelerator can be treated as they are from different sub-sources. Each sub-source represents a critical component in the treatment head and its geometrical dimensions are determined by the component dimensions. Each sub-source has its own energy spectrum and planar fluence distribution derived from the simulated phase space data. When the model is used for dose calculation, the incident energy and position of a particle are sampled from the corresponding stored energy spectrum and planar fluence distribution. The incident direction of the particle is reconstructed by sampling the position of the particle on the sub-source and on the phantom surface. The correlation between the particle position and incident angle is naturally retained.

A primary reason to develop the multiple source model was to find a concise way to replace the huge phase space data files generated from Monte Carlo simulations.^{35,36} The emphasis of the current work is to develop a clinically practical commissioning procedure for Monte Carlo treatment planning. The multiple source model is simplified to make the commissioning procedure as simple as possible while trying to maintaining dose calculation accuracy under all circumstances of clinical relevance. The number of sub-sources in the model is minimized and only those sub-sources of dosimetric significance are retained. The dependence of the model on the detailed information of accelerators is reduced. Sub-sources are represented by dimensionless geometric ob-

jects, such as points and lines, instead of the actual geometrical shapes and sizes of the treatment head components as used previously.^{35,36}

Ma *et al.* established their multiple source model from the Monte Carlo simulated phase space data on the patient surface (at 100 cm SSD) and the last scraper of the electron applicator was included in the model as a sub-source.^{35,36} In this work, the treatment head is simulated using the BEAM code down to just above the last scraper of the electron applicator,³⁴ where the patient specific cutout is inserted. The last scraper, as well as the field-defining cutout, are simulated together with the patient CT phantom when performing Monte Carlo treatment planning dose calculations. The advantage of this method is that the beam model is patient independent. However, this approach, compared to that of Ma *et al.*,^{35,36} requires more careful beam modeling since an air gap between the last scraper and patient surface is not included in the original BEAM simulation.

In the present paper, the beam modeling approach is applied to a Varian Clinac 2100C machine at Stanford Medical Center, which is chosen as the reference machine to build beam models. At first, a very detailed model for each beam is used as the starting point. All the critical components of the treatment head are modeled as sub-sources. With this model, the phase space information of the electron beam can be precisely reconstructed and the dose distribution in a water phantom can be accurately calculated. Then, the number of sub-sources is gradually reduced while maintaining the accuracy in dose distribution calculation. We find that a point electron source with the energy spectrum obtained from the Monte Carlo simulation is able to give a reasonably accurate depth-dose curve, which is consistent with the previous observation.³⁶ By adding another point photon source, the bremsstrahlung tail in the depth dose distribution can be reproduced accurately. However, it is found that the penumbra at the phantom surface generated with this two point source model is sharper compared to that generated with the full phase space data. In order to get the dose profiles correct, we find that, in addition to the two point sources, two square ring electron sources (which emit electrons isotropically) are needed to represent electrons scattered from the applicator scrapers. (The term *square ring* is used here to represent the edge of a square.) Therefore, the beam model should include four sub-sources: a point electron source for direct electrons (which do not interact with the beam defining system) and electrons scattered from the primary collimator, movable jaws and shieldings, a point photon source for all contaminant photons, and two square ring electron sources for electrons scattered from the first two scrapers of the electron applicator (the third also last scraper is not included in the model).

As described previously, beam modeling consists of two steps, namely, beam representation and beam reconstruction.^{35,36} In beam representation, parameters in the model are extracted from the simulated phase space file. In the current simplified model, these parameters include the positions and relative intensities of the sub-sources, the energy spectra for particles inside and outside the field for each

sub-source, and the planar fluence distributions on the scoring plane (directly above the last scraper) for each sub-source. Beam reconstruction is performed when using the model for dose calculations. The phase space information for each particle, including the energy, position and direction, is reconstructed from the scored source parameters.

2. Beam representation

The positions of the virtual electron and photon point sources can be determined using a method described in Ref. 36, which is analogous to the pinhole method.³⁹ A thin annular aperture is selected on the scoring plane and phase space particles are allowed to pass through the aperture and form an image at a distance below the scoring plane. Ray lines drawn through the center of the aperture and the peak of the aperture image form a virtual focal spot, which is adopted as the position of the point source. This pinhole method is very effective for the photon point source. However, we find that for electrons, this method is only applicable to high energy beams. For lower energy beams, e.g., 6 MeV, the virtual SSD determined with this method is greatly overestimated and dependent on the radius of the thin annular aperture on the scoring plane. This is due to the fact that the in-air multiple scattering of low energy electrons is significant. To overcome this problem we performed another Monte Carlo simulation of the accelerator treatment head by replacing the intervening air with vacuum. Then, based on the new phase space data, this pinhole method can be used to generate the correct position for the virtual electron point source, which is independent of the sampling radius. The effect of in-air multiple scattering is taken into account during beam reconstruction by adding a perturbation to the electron incident direction, as discussed later.

Two square ring sources of electrons are located at the corresponding positions of the two applicator scrapers. The sides of the square rings correspond to the actual openings of the scrapers.

The energy spectrum for each sub-source is derived from the simulated phase space data. It was found that the mean energy of the electrons is relatively uniform inside the field as well as outside the field. The change of mean energy with the distance from the central axis is more like a step function.³⁶ Therefore, in the current model, each sub-source has two different energy spectra, one for electrons inside and the other for electrons outside the treatment field. Parameters stored in the model are the minimum and maximum energies, number of energy bins as well as the relative fluence for each energy bin. The minimum and maximum energies correspond to the cutoff energies (ECUT or PCUT) and the incident energy used in the accelerator simulation. The number of bins is determined by the desired resolution. For example, if we want the uncertainty in the calculated depth of 50% dose, R_{50} , to be less than 1%, the uncertainty in the peak position of the energy spectrum should be within 1% and therefore the bin width should be smaller than 1% of the peak energy. For the 12 MeV beam, we used 128 bins and then the bin width is less than 0.1 MeV. This bin width is

also found to be small enough to represent the peak width of the energy spectrum, which has a significant effect on the slope of the depth dose fall-off.

The planar fluence distribution for each sub-source is also derived from the simulated phase space data and recorded on the scoring plane using a grid scheme. Within each pixel of the grid, the planar fluence is assumed to be uniform. The dimension of a pixel is dependent on field size, usually from 1 to 3 mm. Parameters used to represent the planar fluence distribution include the treatment field dimension, the number of pixels and the relative intensity of each pixel, for each sub-source. It has been found that in general, the mean energy varied from position to position in the treatment field by less than 10% for a given sub-source.³⁶ Thus, it is reasonable to store and then sample the particle energy and position independently.

The angular distributions are not scored explicitly. They are reconstructed during the dose calculation, as described in the next section.

Finally, the simulated phase space information is represented with a set of parameters for each sub-source. The resultant source parameter file is much smaller (about 100 kilobytes) than the original phase space file (>100 megabytes).

3. Beam reconstruction

When performing dose calculation in a patient's CT phantom, the source parameter file is used to reconstruct the phase space information (energy, position and direction) of every incident particle. The beam reconstruction process consists of the following steps:

- (1) Determine from which particular sub-source a particle originates by sampling from the relative source intensity of each sub-source.
- (2) Determine the position on the sub-source (excluding point sources) where the particle is emitted.
- (3) Sample the particle position on the scoring plane from the fluence pattern for the sub-source.
- (4) Sample the particle energy from the energy spectrum for the given sub-source based on the particle position (inside or outside the treatment field).
- (5) Determine the particle incident angle by connecting the position on the sub-source from where the particle is emitted and the position of the particle on the scoring plane.
- (6) Add in-air perturbation on the particle direction if it is an electron.

The sampling from the relative source intensity distribution is done by a table-look-up method.³⁵ All the sub-sources are in turn numbered from 1 to N (here $N=4$ for accelerators with designs similar to the Varian Clinac 2100C machine) and the relative intensity of the i th sub-source is p_i ($i=1, \dots, N$). The accumulative source intensity for the i th sub-source, $P_i (= \sum_{j=1}^i p_j)$, is multiplied by a large integer M . The value of M is determined according to the desired sampling precision of the relative source intensity. For ex-

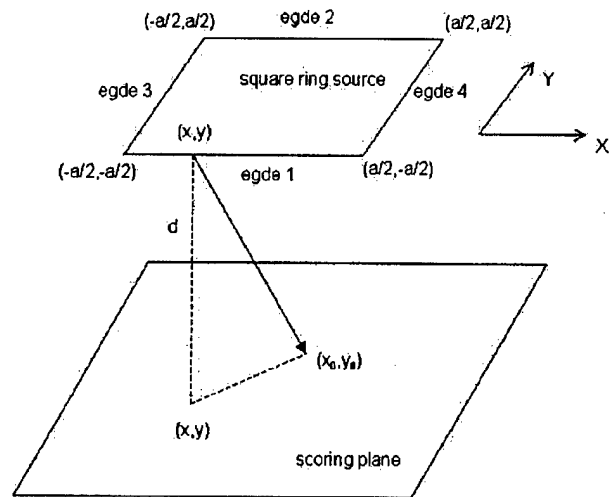


FIG. 1. A diagram for illustrating the sampling algorithm from a square ring source. The origin of the coordinate system is at the center of the square ring.

ample, $M=1000$ corresponds to the precision of 0.1% in sampling from the relative source intensity distribution. Then, a one dimensional array of M elements is prepared by assigning value i to array elements from $INT(MP_{i-1})$ to $INT(MP_i)$, where the operator INT returns the integer part of a real number. During the beam reconstruction, a random integer number K between 1 and M is generated and the value of the K th array element is the sub-source number where the particle is emitted. Such a table-look-up method is of very high sampling speed and efficiency. Its speed is also independent of the number of sub-sources. The sampling precision is usually adequate as long as an large enough array is used.

According to the energy spectra on the scoring plane, the bin number in which the particle energy falls is also sampled using the table-look-up method. An additional uniform sampling is done within the given energy bin to make the particle energy continuous.

The same table-look-up method is also used to sample the pixel number corresponding to a particle position on the scoring plane. Another sampling is performed uniformly to determine the particle's coordinates within the chosen pixel.

For the point sources, the incident angle of the particle is determined by constructing a ray line from the point source to the position of the particle on the scoring plane. For the square ring electron sources, we need to determine where the electron comes from on the ring. This is done in two steps. First, we determine from which edge of the square ring the electron is emitted. Second, we determine from where on the chosen edge the electron comes.

As illustrated in Fig. 1, a square ring of size $a \times a$ is located above the scoring plane at a distance d . We assume that the square ring edge emits electrons uniformly and isotropically. Under this approximation, the probability for an electron on the scoring plane to come from a point on the ring is proportional to the inverse square of the distance be-

tween the points on the ring and plane. This approximation greatly simplifies the sampling process. It is found that the angular distribution of the scattered electrons reconstructed based on the fluence distribution on the scoring plane and the emitting position on the square ring source is reasonably accurate, although electrons scattered from the applicator scraper mainly correspond to electrons incident on the vertical face of the scraper and are dominantly forward directed.⁴⁰ Furthermore, the dose profile at the patient surface is greatly influenced by electrons scattered from the last scraper or cut-outs, which are not included in the source model but will be accurately simulated with the patient CT phantom.

For an electron at position (x_0, y_0) on the scoring plane (see Fig. 1), the probability for it to have come from the i th edge is given as

$$p'_i(x_0, y_0) \sim \frac{1}{C_i} \left[\arctan\left(\frac{x_0 + a/2}{C_i}\right) - \arctan\left(\frac{x_0 - a/2}{C_i}\right) \right] \text{ for } i=1,2, \quad (1)$$

$$p'_i(x_0, y_0) \sim \frac{1}{C_i} \left[\arctan\left(\frac{y_0 + a/2}{C_i}\right) - \arctan\left(\frac{y_0 - a/2}{C_i}\right) \right] \text{ for } i=3,4, \quad (2)$$

where

$$C_1 = \sqrt{(y_0 + a/2)^2 + d^2}, \quad (3)$$

$$C_2 = \sqrt{(y_0 - a/2)^2 + d^2}, \quad (4)$$

$$C_3 = \sqrt{(x_0 + a/2)^2 + d^2}, \quad (5)$$

$$C_4 = \sqrt{(x_0 - a/2)^2 + d^2}. \quad (6)$$

Using the probabilities given above, the edge from which the electron has come can be sampled. Then, the position (x, y) on the chosen edge is further sampled. For edges 1 and 2,

$$x = x_0 - C_i \cdot \tan \left[(1 - \xi) \cdot \arctan\left(\frac{x_0 + a/2}{C_i}\right) + \xi \cdot \arctan\left(\frac{x_0 - a/2}{C_i}\right) \right] \quad i=1,2, \quad (7)$$

$$y = \begin{cases} -a/2 & \text{for } i=1 \\ a/2 & \text{for } i=2 \end{cases}, \quad (8)$$

and for edges 3 and 4,

$$x = \begin{cases} -a/2 & \text{for } i=3 \\ a/2 & \text{for } i=4 \end{cases} \quad (9)$$

$$y = y_0 - C_i \cdot \tan \left[(1 - \xi) \cdot \arctan\left(\frac{y_0 + a/2}{C_i}\right) + \xi \cdot \arctan\left(\frac{y_0 - a/2}{C_i}\right) \right] \quad i=3,4, \quad (10)$$

where ξ is a random number uniformly distributed from 0 to 1.

After the electron position on the square ring is determined, the connection of this position to the position on the scoring plane gives the electron's incident direction, which needs to be additionally perturbed to address the in-air multiple scattering.

In a previous implementation of this model, the effect of electron multiple scattering in air as well as other materials on its path to the scoring plane was taken into account by sampling the electron perturbation angle from a Monte Carlo simulated angular distribution.³⁶ This angular distribution was stored while performing the Monte Carlo simulation for the accelerator and only included electrons falling into a small region (e.g., of 1 cm radius) around beam central axis. In the current work, the effect of in-air multiple scattering is considered more accurately using the Fermi-Eyges theory.^{2,3} The effect of other materials is considered by adding a parameter to the standard deviation of the angular distribution. The Fermi-Eyges theory is a well-known small-angle theory and can predict the multiple scattering effect of megavoltage electrons in air or other heavier materials as long as the electron effective pathlengths are small.^{41,42}

Assume that an electron initially travels along the z axis. According to the Fermi-Eyges theory, the distributions for the projections of the polar angle, θ , on the $x-z$ plane, θ_x , and on the $y-z$ plane, θ_y , are both Gaussian after electrons travel a distance, and are given as^{3,42}

$$f(\theta_x) = \frac{1}{\sqrt{2\pi}\sigma_{\theta_x}} \exp\left(-\frac{\theta_x^2}{2\sigma_{\theta_x}^2}\right), \quad (11)$$

$$f(\theta_y) = \frac{1}{\sqrt{2\pi}\sigma_{\theta_y}} \exp\left(-\frac{\theta_y^2}{2\sigma_{\theta_y}^2}\right), \quad (12)$$

where σ_{θ_x} and σ_{θ_y} are the standard deviations for each Gaussian distribution, respectively. In a homogeneous material, and without the presence of an electromagnetic field, both standard deviations should be the same, so we let $\sigma = \sigma_{\theta_x} = \sigma_{\theta_y}$. Under the small-angle approximation

$$\theta^2 = \theta_x^2 + \theta_y^2, \quad (13)$$

therefore the polar angle θ obeys a radial Gaussian distribution while the azimuthal angle ϕ is uniformly distributed in $[0, 2\pi]$. Hence the sampling method for these two angles is given as follows:

$$\theta = \sigma \sqrt{-2 \ln \xi_1}, \quad (14)$$

$$\phi = 2\pi \xi_2, \quad (15)$$

where ξ_1 and ξ_2 are random numbers uniformly distributed in $[0, 1]$.

According to the Fermi-Eyges theory, σ can be calculated as^{3,42}

$$\sigma^2 = A_0 - A_1^2/A_2, \quad (16)$$

where

$$A_i = \frac{1}{2} \int_0^l K(l-t)^i dt, \quad i=0,1,2. \quad (17)$$

Here, K is the electron linear scattering power and l is the distance at which electrons travel. The electron linear scattering power can be fitted well using a simple formula proposed by Werner *et al.*:⁴³

$$K(E) = \alpha E^{-\beta}. \quad (18)$$

Using this formula we fitted the linear scattering power data in air supplied by ICRU Report 35⁴⁴ and found that $\alpha = 3.329 \times 10^{-3} \text{ rad}^2/\text{cm}$ and $\beta = 1.638$. E is the electron energy in MeV and sampled from the energy spectrum at the scoring plane. The energy loss of electrons in air is usually very small and can be ignored when they travel from the virtual source to the scoring plane. The mean energy loss of 6 MeV electrons after traveling 100 cm in air is about 4% of its initial energy (estimated using the stopping power) and it is about 2% for 20 MeV electrons. Therefore σ can be given as

$$\sigma^2 = \frac{1}{8} K(E)l, \quad (19)$$

which is a function of electron energy and the distance between the virtual source and the position on scoring plane. During beam reconstruction, according to the sampled electron energy, positions on the scoring plane and on the virtual source, σ can be calculated. Then using Eqs. (14) and (15) θ and ϕ are sampled and a perturbation is added to the electron's incident direction.

The perturbation caused by in-air multiple scattering can be directly calculated using Eq. (19) for electrons from the squaring ring sources. For direct electrons, there are other accelerator components in their paths from the virtual point source to the scoring plane in addition to the intervening air, such as the exit window, scattering foil, monitor chamber, mirror and protection window. The effect of these materials on electron angular distribution has been mainly included in the determination of the virtual electron point source position. We also need to take into account the angular perturbation caused by these materials. If we know precisely the material and thickness of these parts, we can calculate their effect on σ , as done by Keall and Hoban.⁴¹ However, it is usually difficult for users to know this information about their accelerator when commissioning a Monte Carlo treatment planning system. Therefore, we introduce a factor k to account for the effect of these materials. For direct electrons, σ is then given as

$$\sigma^2 = \frac{1}{8} K(E)lk. \quad (20)$$

The factor k is determined by fitting the angular distribution calculated using Fermi-Eyes theory to that simulated with the Monte Carlo method for direct electrons. The introduction of k factor provides a potentially tunable parameter in the source model.

4. Model verification

The four-source model is verified dosimetrically by comparing the dose distributions in a water phantom calculated

using the model with those calculated using the full phase space data. Dose distributions are calculated for various combinations of three electron energies (6, 12, and 20 MeV), three applicator sizes (6×6 , 10×10 , and $20 \times 20 \text{ cm}^2$), and two SSDs (100 cm and 120 cm).

The measurement of electron beam applicator factors (defined as the ratio of the open field dose in water at d_{\max} for a given applicator to that of the reference applicator, typically the 10×10 or $15 \times 15 \text{ cm}^2$, for the same beam energy) is done during accelerator commissioning for all energy/cone combinations. Therefore, the applicator factors will be supplied by the user when performing the model commissioning. Cutout factors (defined as the ratio of the dose in water at d_{\max} for a blocked field to that of the open field for the same applicator and beam energy) are patient specific and not always easy to measure accurately for all clinical situations. Therefore, the model should be able to calculate cutout factors. To demonstrate this, we compare the model calculated cutout factors with those measured and calculated by Kapur *et al.* using a full Monte Carlo simulation.⁴⁵

B. Beam commissioning

The four-source model which is built using a Varian Clinac 2100C accelerator as the reference machine can be used to reconstruct electron beams from other Clinac 2100C accelerators by tuning the energy spectra in the model.

For accelerators with exactly the same design, the major different is the electron incident energy due to the on-site tuning to suit the user. This energy approximately corresponds to the maximum energy of all the stored energy spectra in the source model. It is found that the energy spectra for all sub-sources are very similar for different accelerators of the same type. When the incident energy is changed, the energy spectra can be approximated as stretched or compressed along the energy axis accordingly. The depth dose curve is very sensitive to the electron incident energy and therefore used to adjust the maximum energy, E_{\max} , in the model. The relationship between the incident energy, E_{in} , and R_{50} has been studied by simulating the reference accelerator using a $10 \times 10 \text{ cm}^2$ cone and 100 cm SSD with various incident energies. Then, the variation of E_{in} as a function of the variation of R_{50} is established for this type of accelerator. This relationship is used as a guide to tune the maximum energy in the model to commission a clinical beam.

The proposed commissioning approach can be summarized as follows:

- (1) Chose an accelerator as the reference machine for all other accelerators of the same design, and carefully perform full Monte Carlo simulations for the electron beams of various nominal energies from the reference machine with $10 \times 10 \text{ cm}^2$ applicator.
- (2) Build the source models for the simulated beams based on the Monte Carlo phase space data, perform Monte Carlo dose calculation in water for 100 cm SSD, and record the maximum energy, $E_{\max}^{(\text{ref})}$, in the model and the $R_{50}^{(\text{ref})}$ value for each beam.

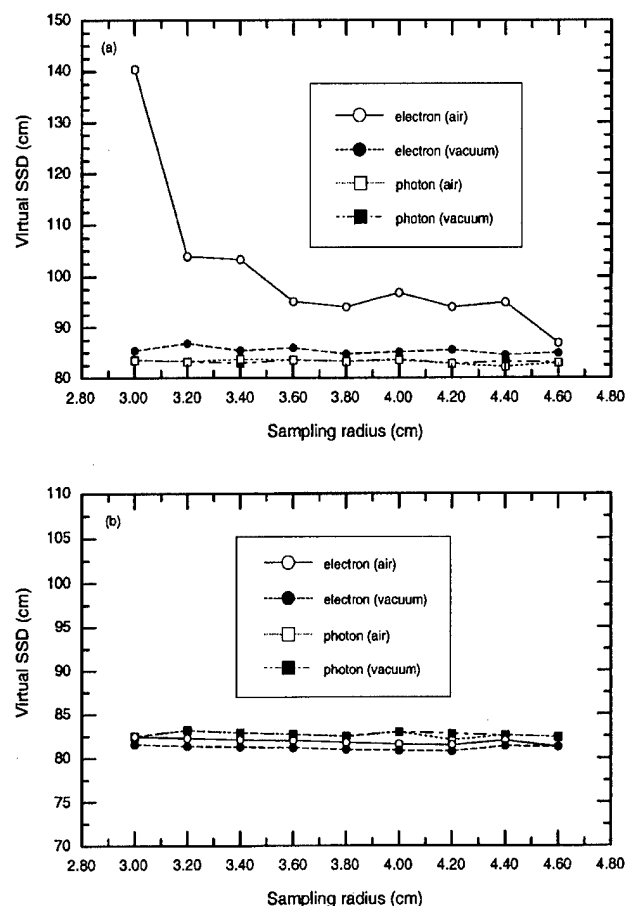


FIG. 2. Effects of intervening air and sampling radius on virtual SSD (defined here as the distance from the point source to the scoring plane) for the electron point source determined with the pinhole method. (a) 6 MeV; (b) 20 MeV.

- (3) For the beam to be commissioned, find the $R_{50}^{(mca)}$ value of the measured depth-dose curve in water for $10 \times 10 \text{ cm}^2$ applicator and 100 cm SSD.
- (4) Select the reference beam which has the same or closest nominal energy as the commissioning beam. Let $i=0$, $E_{\max}^{(i)} = E_{\max}^{(\text{ref})}$, and $R_{50}^{(i)} = R_{50}^{(\text{ref})}$.
- (5) Calculate $\Delta R_{50}^{(i)} = R_{50}^{(i)} - R_{50}^{(mca)}$. If $\Delta R_{50}^{(i)} \leq \epsilon$, where ϵ is the pre-set convergence tolerance, stop iteration and use $E_{\max}^{(i)}$ as the maximum energy in the source model for the commissioning beam; otherwise, go to the next step.
- (6) According to the relationship between ΔE_{in} and ΔR_{50} , calculate $\Delta E^{(i)}$ using $\Delta R_{50}^{(i)}$ and then calculate $E_{\max}^{(i+1)} = E_{\max}^{(i)} - \Delta E^{(i)}$.
- (7) Calculate the dose distribution using the source model with $E_{\max}^{(i+1)}$ and find the corresponding $R_{50}^{(i+1)}$.
- (8) Let $i \leftarrow i+1$; go back to step 5.

The first two steps only need to be done once for all accelerators of the same design. The convergence tolerance, ϵ , is set by the user, usually according to the estimated measurement error in R_{50} . For example, $\epsilon=1 \text{ mm}$ is good enough in most

clinical situations. The iteration process converges very fast; usually only two or three iterations are needed even for ϵ much smaller than 1 mm.

The commissioning approach has been applied to three electron beams, A, B, and C. The reference beam is the same for all three beams, which is from the reference Clinac 2100C accelerator with $E_{\text{in}}=12.0 \text{ MeV}$. Beam A and beam B are also from the reference machine but with E_{in} as 9.0 MeV and 15.0 MeV, respectively. These two beams are used to mimic two clinical beams of the same nominal energy as the reference beam but with significantly different incident energies. Of course, in reality, the electron incident energy will not be tuned so much ($\pm 3 \text{ MeV}$). These two beams are used as extreme cases to test the commissioning approach. Beam C is a 9 MeV electron beam from another Clinac 2100C accelerator. The dose distributions for beam C are taken from the published data.³⁸

III. RESULTS AND DISCUSSION

Figure 2 shows the effects of intervening air and sampling radius on the electron and photon virtual SSD determined with the pinhole method for 6 MeV and 20 MeV beams. It can be seen that for photons and high energy electrons (20 MeV) effects of intervening air and sampling radius on the positions of virtual point sources are negligible. However, for low energy electrons (6 MeV), these effects are significant. Therefore, to obtain the accurate virtual electron point source position for low energy beams, the phase space simulated without intervening air should be used.

Figure 3 shows the comparison between the angular distributions for direct electrons in 6, 12 and 20 MeV beams calculated with the Fermi-Eyges theory and the Monte Carlo method. We can see that, in general, the fitted angular distributions based on the Fermi-Eyges theory match well with those calculated with the Monte Carlo simulation. We also notice that at large angles the Fermi-Eyges theory slightly

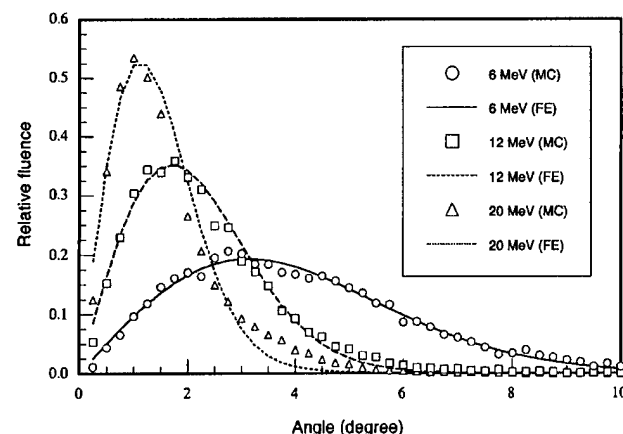


FIG. 3. Angular distributions for direct electrons calculated using the Fermi-Eyges theory and the Monte Carlo method. Beam energies are 6 MeV, 12 MeV and 20 MeV. The fitted k factor is 1.540 for 6 MeV, 1.501 for 12 MeV and 1.571 for 20 MeV. Each distribution is normalized to have unit area under the curve.

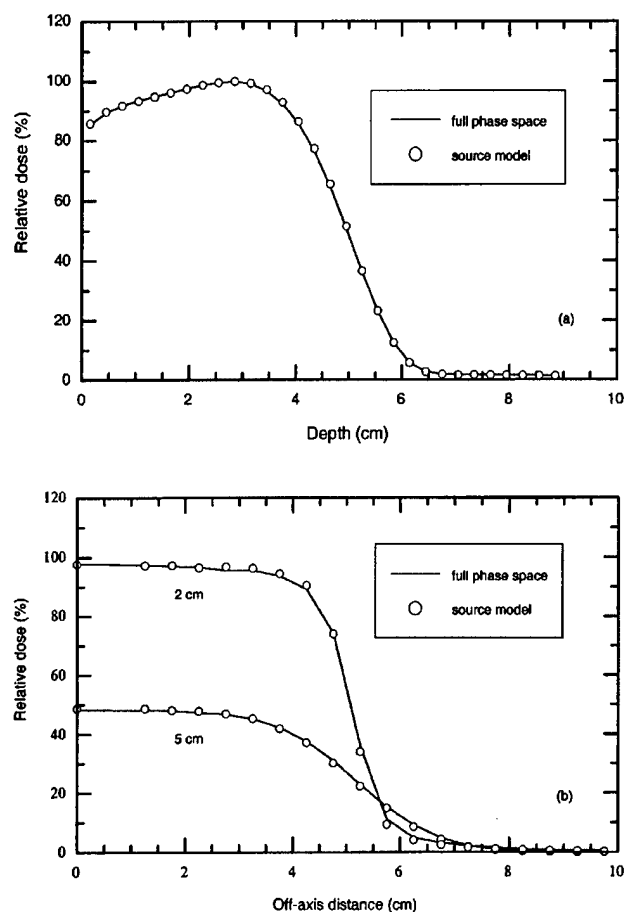


FIG. 4. Dose distributions in water for 12 MeV electron beam with $10 \times 10 \text{ cm}^2$ applicator at 100 cm SSD, calculated with full phase space data and source model: (a) Depth-dose distributions; (b) dose profiles at depths of 2 cm and 5 cm. Curves are normalized to the dose at d_{max} .

underestimates electron fluence due to the fact that it is a small-angle theory. We found that the small discrepancy does not have any significant effect on the final dose distributions. Therefore, the Fermi-Eyges theory with the fitted k factor can be used to account for the angular perturbations of electrons on their way from the source to the scoring plane.

The four-source model was tested by comparing the dose distributions calculated by the model with those calculated by full phase space data for various combinations of three electron energies (6, 12, and 20 MeV), three applicator sizes (6×6 , 10×10 , and $20 \times 20 \text{ cm}^2$), and two SSDs (100 cm and 120 cm). For all the cases tested, the agreement of 1%–2%/1–2 mm has been achieved. Figure 4 shows the comparison for a 12 MeV beam with a $10 \times 10 \text{ cm}^2$ cone at 100 cm SSD. Figure 5 gives the depth-dose curves and dose profiles for 20 MeV beam with $6 \times 6 \text{ cm}^2$ cone at 120 cm SSD, calculated with both the source model and full phase space data. All the curves in Figs. 4 and 5 are normalized to the doses at d_{max} . The Monte Carlo uncertainty is always less than 0.5% and therefore not shown on the curves. In both figures the agreement between the full Monte Carlo simulations and the source model calculations is better than 1%/1 mm. Keep in

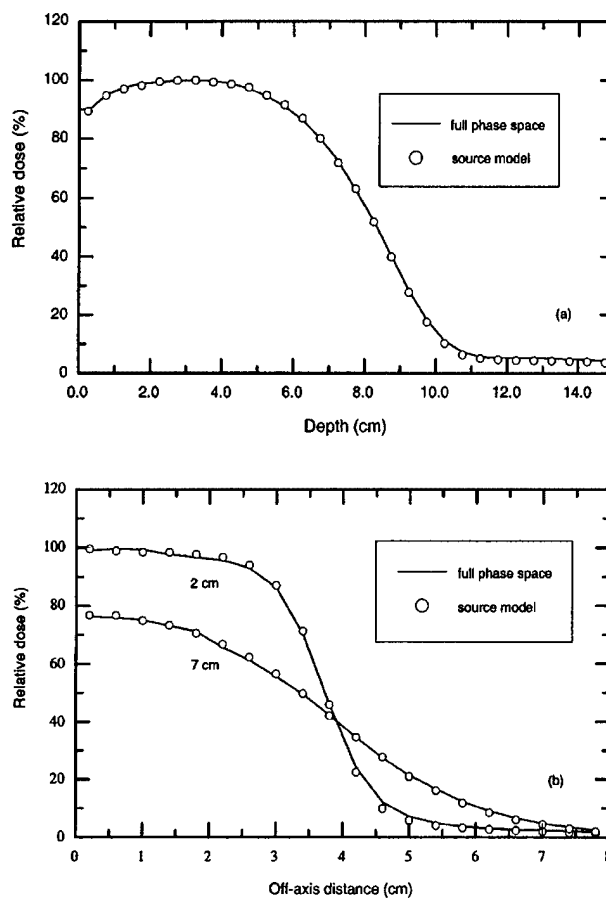


FIG. 5. Dose distributions in water for 20 MeV electron beam with $6 \times 6 \text{ cm}^2$ applicator at 120 cm SSD, calculated with full phase space data and source model: (a) Depth-dose distributions; (b) dose profiles at depths of 2 cm and 7 cm. Curves are normalized to the dose at d_{max} .

mind that 20 cm air gap is rarely used in actual clinical situations. Therefore, we have demonstrated that the simplified four-source model can be used for accurate dose calculations even for extreme cases (such as very large extended SSDs).

The capability of the model for calculating the relative beam output was also tested. Table I shows cutout factors for various square inserts in a $10 \times 10 \text{ cm}^2$ applicator for 6, 12 and 20 MeV electron beams. It is found that the cutout factors calculated with the four-source model are within about $\pm 2\%$ compared to the measured values except for one case where we see 2.5% difference. This is at about the same accuracy level as the full Monte Carlo simulation and considered to be acceptable for clinical use.

The relationship between E_{in} and R_{50} for the reference accelerator with a $10 \times 10 \text{ cm}^2$ cone and 100 cm SSD is shown in Fig. 6. A linear relationship was found and fitted as

$$E_{\text{in}} = 2.597R_{50} + 0.633. \quad (21)$$

It gives the relationship between the variation in the incident energy and the variation in R_{50} as

$$\Delta E_{\text{in}} = 2.597\Delta R_{50}. \quad (22)$$

TABLE I. The electron cutout factors for various square inserts in $10 \times 10 \text{ cm}^2$ applicator for 6, 12, and 20 MeV beams calculated with the source model and the full phase space data and compared with the measurement of Kapur *et al.* (Ref. 45). The values in parenthesis indicate the difference of the data calculated with the source model or the full phase space from the measured data.

Energy (MeV)	Insert (cm^2)	Cutout factor		
		Source model	Full phase space	Measurement
6	2×2	0.803 (2.5%)	0.765 (−1.3%)	0.778
	3×3	0.930 (0.3%)	0.923 (−0.4%)	0.927
	4×4	0.970 (−1.8%)	0.982 (−0.6%)	0.988
	8×8	1.002 (−0.1%)	1.005 (−0.2%)	1.003
12	2×2	0.881 (−0.8%)	0.861 (−2.8%)	0.889
	3×3	0.908 (−2.0%)	0.930 (0.2%)	0.928
	4×4	0.942 (−2.1%)	0.956 (−0.7%)	0.963
	8×8	0.999 (0.8%)	1.002 (1.1%)	0.991
20	2×2	0.963 (−1.1%)	0.957 (−1.9%)	0.976
	3×3	0.989 (−0.4%)	0.968 (−2.5%)	0.993
	4×4	0.993 (−1.8%)	0.993 (−1.8%)	1.011
	8×8	0.999 (−0.5%)	0.993 (−1.1%)	1.004

Equation (22) is used for tuning the maximum energy in the source model to match the measured depth dose curves when commissioning a clinical beam.

Figure 7 shows the dose distributions for the reference beam, beam A, and beam B with the applicator size of $10 \times 10 \text{ cm}^2$ and SSD of 100 cm. All the curves are normalized to the dose at d_{max} . The statistical uncertainty (1σ) in all the Monte Carlo dose calculations was kept to be smaller than 0.5%, therefore, the error bars are smaller than the symbol size and not shown on the curves. The maximum energy in the source model was adjusted to 8.87 MeV to match the dose distributions of the beam A ($E_{\text{in}}=9.0 \text{ MeV}$) and to 15.17 MeV to match the dose distributions of the beam B ($E_{\text{in}}=15.0 \text{ MeV}$). The difference between the depth-dose curves calculated by the adjusted models and the full Monte Carlo simulation is always less than 0.5% for both beam A and beam B. For dose profiles, the difference is usually less than 1% except that in the shoulder region for beam B the difference is about 2%.

Figure 8 shows the dose distributions for the reference beam and beam C with the applicator size of $10 \times 10 \text{ cm}^2$ and SSD of 100 cm. Again, the curves are normalized to the dose at d_{max} and the Monte Carlo uncertainty is lower than 0.5%. In this case, the maximum energy in the source model was adjusted to 11.25 MeV. The dose distributions calculated by the source model with the adjusted maximum energy agree very well (1%/1 mm) with the published data.³⁸

Table II gives E_{in} and R_{50} for the reference and Monte Carlo simulated beams, and E_{max} and R_{50} for the adjusted source models. For the reference beam, E_{max} was directly obtained from the full Monte Carlo simulation. For beam C, E_{in} is unknown. In this study, we set $\epsilon=0.01 \text{ cm}$. Therefore, the R_{50} 's calculated using the adjusted source model match with the full Monte Carlo simulation to within 0.01 cm. Of course, we will not use such a small ϵ in real clinical applications since it is much smaller than the measurement uncertainty in R_{50} . Here, we just want to demonstrate the capa-

bility of the method to reproduce R_{50} accurately.

We have applied the commissioning approach to electron beams from a Clinac 2300C/D accelerator in our institution. The reference machine is still the same Clinac 2100C accelerator. These two machines are sufficiently similar to each other in treatment head geometry. Their dosimetric characteristics are very close to each other due to the beam tuning during linac acceptance. Therefore, it is not surprising to see that the dose distributions calculated with the adjusted source model agree well (within 1%–2% or 1–2 mm) with the measured data.

These preliminary results have shown that the proposed hybrid commissioning approach can be used for accelerators of the same design to account for the dosimetric variations mainly caused by the on-site tuning of the electron incident energy. The capability of the approach to handle large variation in the electron incident energy has been demonstrated. It is believed that for most clinical accelerators of the same type, their treatment head designs are exactly the same or at least very similar, therefore the dosimetric difference can usually be traced back to the difference in the electron incident energy. Therefore, the current approach should be applicable in most clinical situations. In the future work, the method will be evaluated under more critical conditions, such as small field sizes, extended SSD, and heterogeneous phantoms.

The general idea proposed here should also work for other types of accelerators, although we have selected the Varian Clinac 2100C accelerators in the current study. For each type of accelerator, a reference machine should be carefully simulated using the Monte Carlo method. A source model, which may consist of a different number of sub-sources, can be established based on the simulated data. Then, the maximum energy in the model can be adjusted to commission electron beams from other accelerators of the same type.

In some situations, the proposed commissioning approach may not be directly applicable. For example, the measured

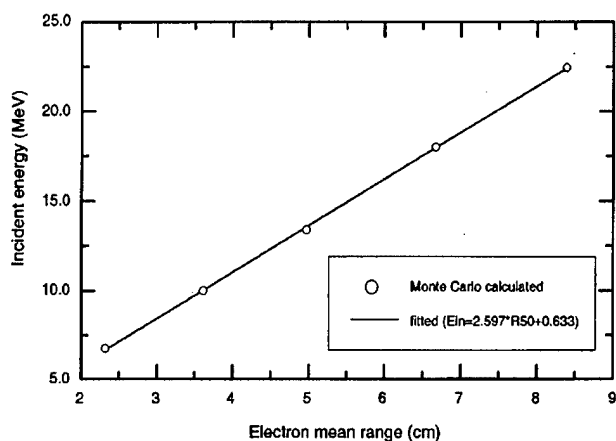


FIG. 6. The relationship between electron incident energy at accelerator exit window (E_{in}) and the depth of 50% dose (R_{50}) for electron beams from the reference accelerator with $10 \times 10 \text{ cm}^2$ applicator and 100 cm SSD. Symbols are calculated with Monte Carlo simulation of the accelerator treatment head. Solid line is the fitted result with formula $E_{in} = 2.597R_{50} + 0.633$.

dose distributions used for commissioning more or less contain measurement errors, depending on the measurement techniques and the experience of the person who performs the measurements. Since only the maximum energy is the adjustable parameter in the current source model, our approach may not be able to exactly match the measured data. Occasionally, an accelerator used in the clinic may differ from its original design in addition to the electron incident energy. Some parts in the accelerator treatment head may be replaced with nonstandard ones. In this case, we can always perform a full Monte Carlo simulation for this unique accelerator and build its own source model. Alternatively, we can make the present approach more versatile to handle those situations. More parameters in the source model other than the maximum energy, such as the relative intensity of each sub-source, the k factor for in-air perturbation for the direct electrons, and the field size, can be adjusted to match the measured dose distributions. For example, the adjustment of the relative intensity of the photon source will ensure a good match to the bremsstrahlung tail in the depth-dose curve. If some of the materials in the paths of direct electrons, such as the scattering foil, monitor chamber or mirror, are different from those used in the reference accelerator, the adjustment of the k factor can yield a better estimation of the electron angular perturbation. The adjustment of the field size in the source model should recover the measurement error in the width of the dose profiles (e.g., errors of the order of about 1 mm are not rare in a clinical situation). In summary, the introduction of more adjustable parameters in the source model will make the current commissioning approach more powerful. This possibility will be investigated in our future study.

IV. CONCLUSIONS

A hybrid commissioning approach based on a multiple source model has been proposed for Monte Carlo treatment planning. It has been demonstrated that a simplified four-

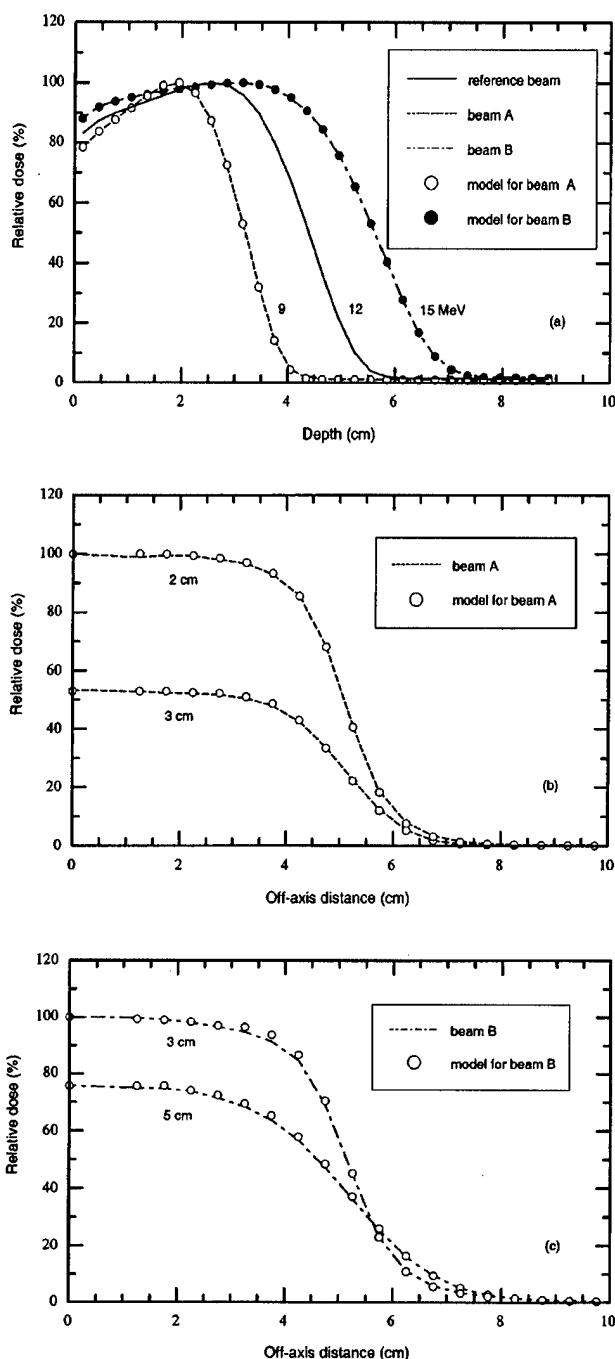


FIG. 7. Dose distributions in water for electron beams from the reference accelerator with $10 \times 10 \text{ cm}^2$ applicator and at 100 cm SSD. The reference beam has the electron incident energy of 12.0 MeV. A source model was built based on the Monte Carlo simulation of the reference beam. The maximum energy of the energy spectra in the model was adjusted to 8.87 MeV to match the beam A (with $E_{in} = 9.0 \text{ MeV}$) and 15.17 MeV to match the beam B (with $E_{in} = 15.0 \text{ MeV}$). Lines are dose distributions from the full Monte Carlo simulations. Symbols are data calculated by the source model with adjusted maximum energies. All data are normalized to the doses at d_{max} . (a) Depth-dose distributions; (b) dose profiles at depths of 2 cm and 3 cm for beam A; (c) dose profiles at depths of 3 cm and 5 cm for beam B.

source model can be used to generate accurate Monte Carlo dose distributions for electron beams from Varian Clinac 2100C accelerators. The model includes a point electron source for direct electrons and electrons scattered from pri-

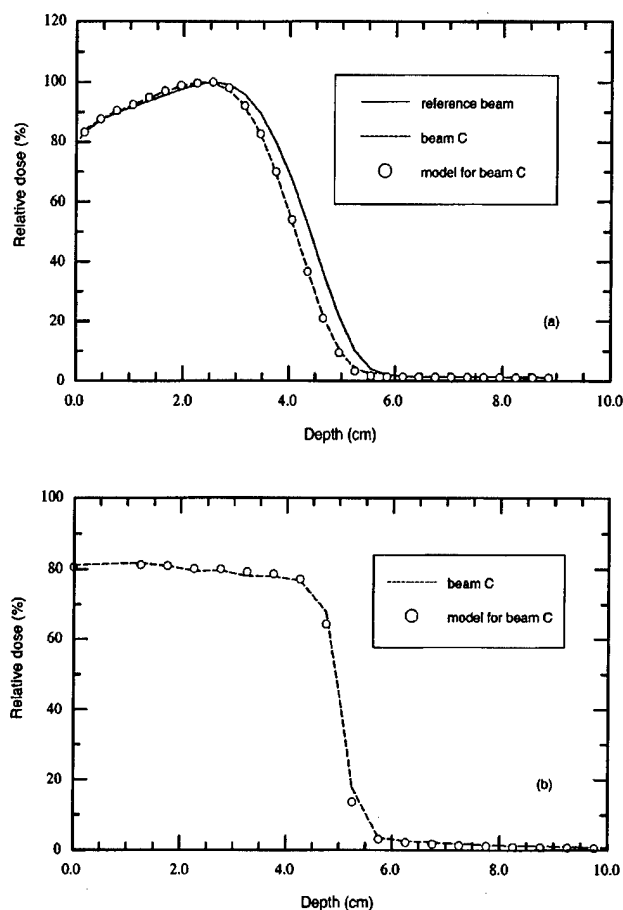


FIG. 8. Dose distributions in water for electron beams with $10 \times 10 \text{ cm}^2$ applicator and at 100 cm SSD. The reference beam (solid line) is from a Clinac 2100C accelerator with $E_{\text{in}} = 12.0 \text{ MeV}$. The dose distributions for beam C (dashed lines) is taken from the published data for a 9 MeV beam from another Clinac 2100C accelerator with type III applicator (Ref. 38). A source model built based on the Monte Carlo simulation of the reference beam is used to match beam C by adjusting the maximum energy to 11.25 MeV (open circles). All data are normalized to the dose at d_{max} . (a) Depth-dose distributions; (b) dose profiles at depth of 0.1 cm.

mary collimator and jaws, a point photon source for all contaminant bremsstrahlung photons, and two square ring electron sources representing electrons scattered from two scrapers (other than the last scraper) of the Varian electron applicator (type III). It was found that the position of the virtual point source can be determined accurately using the pinhole method for photons in all cases and electrons in high energy beams. For low energy beams, we should use the Monte Carlo phase space data which are obtained by simulating the treatment head with the intervening air replaced by vacuum. We also found that the in-air perturbation on the electron incident direction can be properly accounted for using the Fermi-Eyges model. The source model which was built based on the simulated phase space data for the reference accelerator can be used for other accelerators of the same type, by simply adjusting the energy spectra in the model. The capability of this commissioning approach for handling large variation in the electron incident energy has been demonstrated.

TABLE II. Some parameters for the full Monte Carlo simulations and the adjusted source models. E_{in} is the electron incident energy at the exit window in the simulation. E_{max} is the maximum energy in the source model. R_{50} is the depth of 50% dose of the depth dose curve in water for $10 \times 10 \text{ cm}^2$ applicator and 100 cm SSD. A source model was built based on the full Monte Carlo simulation of the reference beam. For beams to be commissioned (A, B, and C), E_{max} in the model was adjusted to match the corresponding R_{50} from the Monte Carlo simulation.

Beam tested	MC simulation		Source model	
	E_{in} (MeV)	R_{50} (cm)	E_{max} (MeV)	R_{50} (cm)
Reference	12.0	4.397	12.00	4.397
Beam A	9.0	3.197	8.87	3.192
Beam B	15.0	5.622	15.17	5.624
Beam C	unknown	4.116	11.25	4.119

ACKNOWLEDGMENTS

The authors are grateful to the referees, Drs. Art Boyer, Alan Nahum, Alex Bielajew, David Findley, Gary Luxton, Ed Mok, Todd Pawlicki, and Frank Verhaegen for useful comments on the manuscript. The authors would also like to thank Dr. Sam Brain, Todd Koumian, and Behrooz Tofighrad for computer support, Dr. Dave Rogers and his OMEGA/BEAM team at the National Research Council of Canada for the Monte Carlo simulation system, and Eva Papiez for supplying some measured data. The work was supported in part by the U.S. Army breast cancer research program (BC971292), NCI Grant No. CA78331 and a consortium agreement with the NumeriX Cooperation.

^aCorresponding author. Tel: (650)498-4074, Fax: (419)498-4015, E-mail: stevej@reyes.stanford.edu

¹K. R. Hogstrom, M. D. Mills, and P. R. Almond, "Electron beam dose calculations," *Phys. Med. Biol.* **26**, 445-459 (1981).

²E. Fermi, in B. Rossi and K. Greisen, "Cosmic-ray theory," *Rev. Mod. Phys.* **13**, 265-268 (1941).

³L. Eyges, "Multiple scattering with energy loss," *Phys. Rev.* **74**, 1534-1535 (1948).

⁴J. Cygler, J. J. Battista, J. W. Scrimger, E. Mah, and J. Antolak, "Electron dose distributions in experimental phantoms: A comparison with 2D pencil beam calculations," *Phys. Med. Biol.* **32**, 1073-1086 (1987).

⁵E. Mah, J. Antolak, J. W. Scrimger, and J. J. Battista, "Experimental evaluation of a 2D and a 3D electron pencil beam algorithm," *Phys. Med. Biol.* **34**, 1179-1194 (1989).

⁶I. Kawrakow, M. Fippel, and K. Friedrich, "3D electron dose calculation using a voxel based Monte Carlo algorithm (VMC)," *Med. Phys.* **23**, 445-457 (1996).

⁷C. M. Ma, E. C. Mok, A. Kapur, T. Pawlicki, D. O. Findley, S. Brain, K. Forster, and A. L. Boyer, "Clinical implementation of a Monte Carlo treatment planning system," *Med. Phys.* **26**, 2133-2143 (1999).

⁸M. A. Ebert and P. W. Hoban, "Possibilities for tailoring dose distributions through the manipulation of electron beam characteristics," *Phys. Med. Biol.* **42**, 2065-2081 (1997).

⁹M. G. Karlsson, M. Karlsson, and B. Zackrisson, "Intensity modulation with electrons: calculations, measurements and clinical applications," *Phys. Med. Biol.* **43**, 1159-1169 (1998).

¹⁰M. Åsell, S. Hyödynmaa, S. Söderström, and A. Brahme, "Optimal electron and combined electron and photon therapy in the phase space of complication-free cure," *Phys. Med. Biol.* **44**, 235-252 (1999).

- ¹¹ A. E. Nahum, "Monte Carlo electron transport simulation II: Application to dose planning," in *The Computation of Dose Distributions in Electron Beam Radiotherapy*, edited by A. E. Nahum (Umeå University, Umeå, Sweden, 1985), pp. 319–340.
- ¹² T. M. Jenkins, W. R. Nelson, A. Rindi, A. E. Nahum, and D. W. O. Rogers, *Monte Carlo Transport of Electrons and Photons* (Plenum, New York, 1988).
- ¹³ T. R. Mackie, "Applications of the Monte Carlo method in radiotherapy," in *Vol. III of Dosimetry of Ionizing Radiation*, edited by K. Kase, B. Bjärgard, and F. H. Attix (Academic, New York, 1990), 541–620.
- ¹⁴ D. W. O. Rogers and A. F. Bielajew, "Monte Carlo techniques of electron and photon transport for radiation dosimetry," in *Vol. III of The Dosimetry of Ionizing Radiation*, edited by K. R. Case, B. E. Bjärgard, and F. H. Attix (Academic, New York, 1990), pp. 427–539.
- ¹⁵ D. W. O. Rogers, "The role of Monte Carlo simulation of electron transport in radiation dosimetry," *Int. J. Appl. Radiat. Isot.* **42**, 965–974 (1991).
- ¹⁶ P. Andreo, "Monte Carlo techniques in medical radiation physics," *Phys. Med. Biol.* **36**, 861–920 (1991).
- ¹⁷ C. Manfredotti, U. Nastasi, R. Ragona, and S. Anglesio, "Comparison of three dimensional Monte Carlo simulation and the pencil beam algorithm for an electron beam from a linear accelerator," *Nucl. Instrum. Methods Phys. Res. A* **255**, 355–359 (1987).
- ¹⁸ C. Manfredotti, U. Nastasi, R. Marchisio, C. Ongaro, G. Gervino, R. Ragona, S. Anglesio, and G. Sannazzari, "Monte Carlo simulation of dose distribution in electron beam radiotherapy treatment planning," *Nucl. Instrum. Methods Phys. Res. A* **291**, 646–654 (1990).
- ¹⁹ A. A. al-Beteri and D. E. Raeside, "Optimal electron-beam treatment planning for retinoblastoma using a new three-dimensional Monte Carlo-based treatment planning system," *Med. Phys.* **19**, 125–135 (1992).
- ²⁰ H. Neuenschwander, T. R. Mackie, and P. J. Reckwerdt, "MMC—A high-performance Monte Carlo code for electron beam treatment planning," *Phys. Med. Biol.* **40**, 543–574 (1995).
- ²¹ P. J. Keall and P. W. Hoban, "Super-Radio Monte Carlo: A 3-D electron beam dose calculation algorithm," *Med. Phys.* **23**, 2023–2034 (1996).
- ²² B. Faddegon, J. Balogh, R. Mackenzie, and D. Scora, "Clinical considerations of Monte Carlo for electron radiotherapy treatment planning," *Radiat. Phys. Chem.* **53**, 217–227 (1998).
- ²³ C. M. Ma and A. E. Nahum, "Calculation of absorbed dose ratios using correlated Monte Carlo sampling," *Med. Phys.* **20**, 1189–1199 (1993).
- ²⁴ M. A. Holmes, T. R. Mackie, W. Sohn, P. J. Reckwerdt, T. J. Kinsella, A. F. Bielajew, and D. W. O. Rogers, "The application of correlated sampling to the computation of electron beam dose distributions in heterogeneous phantoms using the Monte Carlo method," *Phys. Med. Biol.* **38**, 675–688 (1993).
- ²⁵ A. F. Bielajew, "Monte Carlo modeling in external electron-beam radiotherapy—Why leave it to chance?," in *Proceedings of The 11th International Conference on The Use of Computers in Radiation Therapy*, edited by A. R. Hounsell, J. M. Wilkinson, and P. C. Williams (Manchester, UK, 1994), pp. 2–5. North Western Medical Physics Department, Christie Hospital NHS Trust.
- ²⁶ R. Mohan, "Why Monte Carlo?" in *Proceedings of The 12th International Conference on The Use of Computers in Radiation Therapy*, edited by D. D. Leavitt and G. Starkschall, Salt Lake City, Utah (Medical Physics Publishing, Madison, 1997), pp. 16–18.
- ²⁷ C. L. Hartmann-Siantar, P. M. Bergstrom, W. P. Chansler, L. Chase, L. J. Cox, T. P. Daly, D. Garrett, S. M. Hornstein, R. K. House, E. I. Moses, R. W. Patterson, J. A. Rathkopf, and A. S. von Wittenau, "Lawrence Livermore National Laboratory's PEREGRINE project," in *Proceedings of the 12th International Conference on the Use of Computers in Radiation Therapy*, edited by D. D. Leavitt and G. Starkschall, Salt Lake City, Utah (Medical Physics Publishing, Madison, 1997), pp. 19–22.
- ²⁸ J. J. DeMarco, T. D. Solberg, and J. B. Smathers, "A CT-based Monte Carlo simulation tool for dosimetry planning and analysis," *Med. Phys.* **25**, 1–11 (1998).
- ²⁹ L. Wang, C. S. Chui, and M. Lovelock, "A patient-specific Monte Carlo dose-calculation method for photon beams," *Med. Phys.* **25**, 867–878 (1998).
- ³⁰ J. O. Deasy, P. R. Almond, and M. T. McEllistrem, "Measured electron energy and angular distributions from clinical accelerators," *Med. Phys.* **23**, 675–684 (1996).
- ³¹ J. J. Janssen, E. W. Korevaar, L. J. van Battum, P. R. M. Storchi, and H. Huizenga, "Clinical electron beam dose calculations with the Phase Space Evolution model," in *Proceedings of the 12th International Conference on the Use of Computers in Radiation Therapy*, edited by D. D. Leavitt and G. Starkschall, Salt Lake City, Utah (Medical Physics Publishing, Madison, 1997), pp. 195–196.
- ³² M. Udale, "A Monte Carlo investigation of surface doses for broad electron beams," *Phys. Med. Biol.* **33**, 939–954 (1988).
- ³³ M. Udale-Smith, "Monte Carlo calculations of electron beam parameters for three Philips linear accelerators," *Phys. Med. Biol.* **37**, 85–105 (1992).
- ³⁴ D. W. O. Rogers, B. A. Faddegon, G. X. Ding, C. M. Ma, J. We, and T. R. Mackie, "BEAM: A Monte Carlo code to simulate radiotherapy treatment units," *Med. Phys.* **22**, 503–524 (1995).
- ³⁵ C. M. Ma and D. W. O. Rogers, "Beam characterization: a multiple-source model," Technical Report PIRS 509d, National Research Council of Canada, Ottawa, Canada, 1995.
- ³⁶ C. M. Ma, B. A. Faddegon, D. W. O. Rogers, and T. R. Mackie, "Accurate characterization of Monte Carlo calculated electron beams for radiotherapy," *Med. Phys.* **24**, 401–416 (1997).
- ³⁷ C. M. Ma, "Characterization of computer simulated radiotherapy beams for Monte-Carlo treatment planning," *Radiat. Phys. Chem.* **53**, 329–344 (1998).
- ³⁸ G. X. Ding and D. W. O. Rogers, "Energy spectra, angular spread and dose distributions of electron beams from various accelerators used in radiotherapy," Technical Report PIRS 0439, National Research Council of Canada, Ottawa, Canada, 1995.
- ³⁹ AAPM TG-25, "Clinical electron beam dosimetry: Report of AAPM Radiation Therapy Committee Task Group No. 25," *Med. Phys.* **18**, 73–109 (1991).
- ⁴⁰ M. A. Ebert and P. W. Hoban, "A Monte Carlo investigation of electron-beam applicator scatter," *Med. Phys.* **22**, 1431–1435 (1995).
- ⁴¹ P. J. Keall and P. W. Hoban, "Calculating the angular standard deviation of electron beams using Fermi-Eyges theory," *Phys. Med. Biol.* **41**, 1511–1515 (1996).
- ⁴² S. B. Jiang, Z. M. Luo, and K. M. Ayyangar, "Incorporation of the electron energy-loss straggling into the Fermi-Eyges equation," *Radiat. Phys. Chem.* **53**, 477–482 (1998).
- ⁴³ B. L. Werner, F. M. Khan, and F. C. Deibel, "A model for calculating electron beam scattering in treatment planning," *Med. Phys.* **9**, 180–187 (1982).
- ⁴⁴ ICRU 35, "Radiation Dosimetry: Electron Beams with Energies Between 1 and 50 MeV," International Commission on Radiation Units and Measurements, Bethesda, MA, 1984.
- ⁴⁵ A. Kapur, C. M. Ma, E. C. Mok, D. O. Findly, and A. L. Boyer, "Monte Carlo calculations of electron beam output factors for a medical linear accelerator," *Phys. Med. Biol.* **43**, 3479–3494 (1998).

Monte Carlo verification of IMRT dose distributions from a commercial treatment planning optimization system

C-M Ma, T Pawlicki, S B Jiang, J S Li, J Deng, E Mok, A Kapur, L Xing,
L Ma and A L Boyer

Radiation Oncology Department, Stanford University School of Medicine, Stanford, CA 94305,
USA

E-mail: cma@reyes.stanford.edu

Received 25 February 2000, in final form 8 May 2000

Abstract. The purpose of this work was to use Monte Carlo simulations to verify the accuracy of the dose distributions from a commercial treatment planning optimization system (Corvus, Nomos Corp., Sewickley, PA) for intensity-modulated radiotherapy (IMRT). A Monte Carlo treatment planning system has been implemented clinically to improve and verify the accuracy of radiotherapy dose calculations. Further modifications to the system were made to compute the dose in a patient for multiple fixed-gantry IMRT fields. The dose distributions in the experimental phantoms and in the patients were calculated and used to verify the optimized treatment plans generated by the Corvus system. The Monte Carlo calculated IMRT dose distributions agreed with the measurements to within 2% of the maximum dose for all the beam energies and field sizes for both the homogeneous and heterogeneous phantoms. The dose distributions predicted by the Corvus system, which employs a finite-size pencil beam (FSPB) algorithm, agreed with the Monte Carlo simulations and measurements to within 4% in a cylindrical water phantom with various hypothetical target shapes. Discrepancies of more than 5% (relative to the prescribed target dose) in the target region and over 20% in the critical structures were found in some IMRT patient calculations. The FSPB algorithm as implemented in the Corvus system is adequate for homogeneous phantoms (such as prostate) but may result in significant under- or over-estimation of the dose in some cases involving heterogeneities such as the air-tissue, lung-tissue and tissue-bone interfaces.

(Some figures in this article are in colour only in the electronic version; see www.iop.org)

1. Introduction

For the last few years, extensive research has been carried out to develop conformal radiotherapy using computer-controlled linear accelerators equipped with multileaf collimators (MLC) (Boesecke *et al* 1988, Leibel *et al* 1992, LoSasso *et al* 1993, Powlis *et al* 1993, Mageras *et al* 1994, Brewster *et al* 1995, Fraass *et al* 1995, McShan *et al* 1995, Yu *et al* 1995). More recently, intensity modulated radiotherapy (IMRT) has been developed (Brahme 1988, Convery and Rosenbloom 1992, Webb 1992, Boyer *et al* 1997) and implemented (Ling *et al* 1996, Boyer *et al* 1998) that uses computer-controlled modulation of x-ray fields by the MLC. It is anticipated that conformal radiotherapy will provide radiation oncologists with a significantly improved tool to deliver high doses of ionizing radiation to some tumour sites while reducing doses to adjacent normal tissue below levels to which they are unavoidably exposed by currently available techniques. Thus, acute and chronic toxicity associated with treatment of a tumour volume by radiation may be significantly reduced or delayed for certain sites of malignant presentations.

The use of conformal radiotherapy, especially with the IMRT technique, is a major departure from the way radiotherapy is currently delivered. Although the use of MLCs provides the possibility of achieving better dose distributions conformed to tumour targets, it also increases the complexity of treatment. The sequences of leaf movement and their associated effects on the dose delivered to the patient may vary significantly depending on the accelerator and the MLC design. Important factors include the variation of the accelerator head scatter component in the MLC-collimated beam (Convery and Webb 1997), the amount of photon leakage through the leaves (Wang *et al* 1996, Webb 1997, Holmes *et al* 1997), the scatter from the leaf ends, the 'tongue and groove' effect (Chui *et al* 1994, Wang *et al* 1996), the effect of back-scattered photons from the moving jaws and MLC leaves on the monitor chamber signal (Hounsell 1998). Traditionally, patient dose calculations in radiotherapy have been based on correcting measured dose distributions. New dose calculation algorithms have been developed to predict the patient dose from 'first principles' using a model of radiation transport (Mackie *et al* 1995). Comparisons of the traditional photon algorithms and the newer ones have been reviewed by Wong and Purdy (1990), Cunningham and Battista (1995) and Mackie *et al* (1996). Due to the lack of electron transport, the conventional dose calculation algorithms often failed to predict the dose distribution accurately near inhomogeneities (Mackie *et al* 1996, Mohan 1997, DeMarco *et al* 1998, Wang *et al* 1998, Ma *et al* 1999). Furthermore, the inverse-planning algorithms for beam optimization have all used approximations to speed up the dose computation that may introduce significant uncertainty in the calculated dose distributions, especially in the presence of heterogeneities. When simple source models are used in the dose computation, the correlation between the calibrated reference dose and the dose related to a beam segment may be lost. All the above imply a potential problem with the prediction of the dose distributions in a patient for an IMRT treatment.

Oldham and Webb (1997) reported differences in excess of 10% in the absolute dose between the optimization dose calculations and measurements (using film) of fields delivered by a dynamic MLC. The differences were attributed partially to the nonlinearity of dose per monitor unit (MU) for small MU deliveries (the actual dose delivered per MU increased by more than 10% from MU = 20 to MU = 1). Wang *et al* (1996) reported that for the Memorial Hospital's dynamic MLC delivery process, the discrepancies between the calculated dose and the measured dose were in excess of 5% if various effects related to the MLC construction, such as accelerator head scatter, were not properly accounted for. The uncertainty in the doses calculated by a conventional dose calculation algorithm was 5–10% in the presence of heterogeneities (Mohan 1997). Our recent Monte Carlo results were consistent with these findings (Ma *et al* 1999).

The purpose of this work was to verify the accuracy of the IMRT dose distributions from a commercial treatment planning optimization system (Corvus, Nomos Corp., Sewickley, PA) using Monte Carlo simulations. We have used the EGS4/BEAM Monte Carlo code system (Nelson *et al* 1985, Rogers *et al* 1995a, b) to simulate the clinical photon beams from two linear accelerators, Varian Clinac 2100C and 2300C/D (Varian Oncology, Palo Alto, CA). The EGS4/DOSXYZ code (Rogers *et al* 1995a, Ma *et al* 1995) was modified to compute the dose in a patient (a three-dimensional phantom built from the CT data) for multiple fixed-gantry fields. Phantom measurements were performed to commission the Monte Carlo system. The dose distributions in the experimental phantoms and in the patients were calculated and used to verify the optimized treatment plans generated by the Corvus inverse-planning system. In the following sections, we will describe the dose calculations in the inverse-planning system and the Monte Carlo simulations. We will show the dose distributions for homogeneous and heterogeneous phantoms and discuss the effect of material density and atomic number on the final dose calculations.

2. Materials and method

2.1. Treatment planning and dose measurement

The treatment planning optimization system used in this work is the Corvus inverse-planning system. The inverse planning process employs a simulated annealing optimization algorithm (Webb 1992). The dose calculation algorithm used for the inverse planning process is a finite-size pencil beam (FSPB) algorithm, which uses predetermined beamlet dose distributions. The beamlet distributions were derived from measured dose distributions and normalized to produce consistent output factors for various field sizes. The patient inhomogeneity correction is made by 'stretching' the beamlet distribution proportionally based on the equivalent pathlength. Some details of the dose calculations have been described by Holmes *et al* (1998) and Boyer *et al* (1999). The monitor unit calculations for a 'step-and-shoot' leaf sequence algorithm have been discussed by Boyer *et al* (1999). The effect of the leaf leakage is accounted for in Corvus by reducing the original beamlet weight by the same amount as the accumulated leakage for a given leaf sequence. This method works well for those beamlets whose weights are greater than the estimated leakage. If the beamlet weights are smaller than the leakage this method will underestimate the dose as any remaining leakage effect cannot be accounted for and the initial dose calculation does not include any leaf leakage effect (which is unknown before a leaf sequence is generated for the field). The Corvus system has been commissioned for clinical IMRT treatment planning (Xing *et al* 1999) and used for treating head and neck patients with IMRT (Boyer *et al* 1998).

In order to test the Corvus system, inverse plans were computed for various target shapes placed in the centre of a cylindrical water phantom having a diameter of 30 cm. Comparisons of the Corvus dose distributions with measurements have been reported in detail by Boyer *et al* (1999). In this work, we have computed the dose distributions for these plans using Monte Carlo methods (see descriptions below). For completeness, we briefly describe the plans and the measurements below. Inverse plans were computed for different hypothetical targets with different numbers of beams directed toward the axis of the cylinder at the centre of the target and spaced at equal angles. The treatments were delivered using a dynamic multileaf collimator (Varian Oncology Systems, Palo Alto, CA). The leaf sequences computed within the Nomos software were written into files with formats conformed to the requirements of the Varian digital control software. The leaf sequences were delivered using the monitor units calculated by the Corvus system. The absolute dose delivered by the leaf sequences was measured in the 30 cm diameter cylindrical water phantom using a 0.147 cm³ ionization chamber (Wellhöfer Dosimetrie, Schwartenbruck, Germany) following the AAPM TG-21 protocol (AAPM 1983). No corrections were made for the variation in the chamber displacement effect, which depends on the dose gradient at the measurement point and the chamber diameter. This may introduce an up to 2% uncertainty in the measured dose for the 6 mm diameter chamber used (the dose gradient was 5–8% per centimetre at some measurement points). The chamber positioning uncertainty was about 0.1 cm. The overall uncertainty in the measured dose was estimated to be about 3% (1 σ).

2.2. The Monte Carlo simulation

We have used BEAM and DOSXYZ (Rogers *et al* 1995a, b, Ma *et al* 1995) Monte Carlo codes for the accelerator head simulation and dose calculation in the patient respectively. Both codes were EGS4 (Electron Gamma Shower version 4, Nelson *et al* (1985)) user codes, running under the UNIX operating system, developed through the Omega project for Monte Carlo treatment planning dose calculations (Mackie *et al* 1994). Detailed descriptions of the software can be

found from Rogers *et al* (1995a, b). A detailed description of the clinical implementation of the Monte Carlo code system was given in a previous publication (Ma *et al* 1999).

Two types of clinical linear accelerators were simulated for the clinical implementation of Monte Carlo dose verification in this work: Varian Clinac 2100C and 2300C/D (Varian Oncology Systems, Palo Alto, CA). The dimensions and materials for the accelerator components were incorporated according to the manufacturer's specifications. Electron beams emerging from the vacuum exit window were assumed to be monoenergetic and monodirectional with a beam radius of 0.1–0.2 cm. These were found to be reasonable assumptions to achieve an acceptable dose calculation accuracy of about 2% of the dose maximum (D_{\max}) anywhere in the phantom for clinical radiotherapy applications (Kapur *et al* 1998, Ma 1998, Ma *et al* 1999). We obtained accurate phase-space data for photon beams with nominal energies of 4, 6 and 15 MV. The energy cut-offs for electron transport in the accelerator simulation (ECUT and AE) 700 keV (kinetic + rest mass) and for photon transport (PCUT and AP) 10 keV. The maximum fractional energy loss per electron step (ESTEPE) was 0.04. The bremsstrahlung splitting and Russian roulette options were implemented for photon beam simulations (Rogers *et al* 1995b). The ICRU recommended compositions and stopping power values were used for the materials used in the accelerator simulations (ICRU 1984). The phase-space data were scored at a plane immediately above the photon jaws. The number of particles in a photon beam file was about 50 million. Field shaping by photon jaws, blocks and the MLC was further simulated using BEAM and the phase-space data could be stored temporarily or used directly for dose calculations.

The DOSXYZ code was designed for dose calculations in a 3D rectilinear voxel (volume element) geometry (Ma *et al* 1995). Voxel dimensions were completely variable in all three directions. Every voxel could be assigned to a different material. The cross-section data for the materials used were available in a pre-processed PEGS4 cross-section data file. The mass density of the material in a DOSXYZ calculation was varied based on the patient's CT data, although the density effect corrections for the stopping powers of the material remain unchanged (Ma *et al* 1999). The voxel dimensions and materials were defined in a DOSXYZ input file together with the transport parameters such as ECUT, PCUT, ESTEPE and the parameters required by PRESTA (Bielajew and Rogers 1988). The phase-space data obtained from a BEAM simulation was used as a source input with variable source positions and beam incidence angles. Dose contributions from different beam components were selectively calculated based on the particle charge or the LATCH settings specified in the BEAM simulation. DOSXYZ produced a data file that contained geometry specifications such as the number of voxels in all three directions and their boundaries as well as the dose values and the associated (1σ) statistical uncertainties in the individual voxels.

The DOSXYZ code has been modified to read the MLC leaf sequence files for IMRT treatment. For this study, the Varian dynamic MLC leaf sequence files (G-version) generated using a step-and-shoot leaf sequencing algorithm, were used. The monitor units for each leaf sequence were integrated into a two-dimensional map (grids). The dimensions of the map at the isocentre (100 cm from the virtual point source position) are 40 cm in both the x and y directions and the grid sizes were 0.1 cm. The monitor units for the open areas were accumulated for each of the pixels, while for the closed areas a fraction of the monitor units were accumulated based on the measured MLC leakage factor for each beam energy. Thus, the integrated intensity map has included the averaged leaf leakage effect but ignored the influence of the leaf shape (tongue and groove) and the variation of the spatial and spectral distributions due to photon attenuation and scattering in the MLC leaves. This is considered to be a reasonable approach since, unless the effect of organ motion and patient set-up uncertainty has been accounted for properly, the averaged leaf leakage is a more realistic quantity than

the explicit leakage through the leaf and the tongue and groove for estimating the overall dose in a patient during the whole treatment course. The transmission factor for the areas under the photon jaws was assumed to be zero. The dimensions of the photon jaw opening were set according to the actual treatment set-ups. Further modifications were made to simulate several gantry angles in the same run. The leaf sequence files were read sequentially and the gantry angle was changed automatically after the simulation of a photon field was completed.

During the Monte Carlo simulation, the weight of a phase-space particle was altered based on the value of the pixel in the intensity map through which the particle was travelling. To improve the simulation efficiency, two variance reduction techniques were implemented in the DOSXYZ code, particle splitting and Russian roulette (Rogers and Bielajew 1990). The former was applied to the particles with weight greater than unity and the latter was applied to the particles with weight smaller than unity. The splitting and Russian roulette processes were implemented in such a way that the resulting particles would have identical weighting factors. Using uniform weighting factors will generally improve the statistical uncertainty of a simulation.

For patient dose calculations, the simulation phantom was built from the patient's CT data with up to $128 \times 128 \times 128$ voxels (uniform in any dimensions). The side of a voxel varied from 0.2 to 0.4 cm. The EGS4 transport parameters were set to $ECUT = AE = 700$ keV, $PCUT = AP = 10$ keV and $ESTEPE = 0.04$. The number of particle histories simulated ranged from 300 million to 1 billion for up to nine gantry angles for an IMRT treatment. The 1σ statistical uncertainty in the dose was generally 1–2% of the D_{max} value. The CPU time required for an IMRT simulation was 3–15 h on a single Pentium III 450 MHz PC depending on the beam energy and field sizes.

3. Results

3.1. Comparisons in homogeneous water phantoms

Both the inverse-planning system and the Monte Carlo dose calculation system have been commissioned for routine clinical applications (Xing *et al* 1999, Ma 1998, Ma *et al* 1999). Both systems regenerated the PDD curves and the dose profiles at various depths to within 2% of the dose maximum values of the measured beam data for various field sizes and source to surface distances (SSD). The dose distributions given by the Corvus system agreed with measurements to about 3% in a cylindrical water phantom with various hypothetical target shapes (Boyer *et al* 1999). Figure 1 shows the dose distributions in a 30 cm diameter water cylinder irradiated by seven 6 MV intensity-modulated photon beams calculated by Corvus and by the Monte Carlo simulations. The critical structure is in the centre of the water cylinder immediately next to the C-shaped target. A beamlet size of $1 \text{ cm} \times 1 \text{ cm}$ was used in the optimization calculation. The leaf sequencing algorithm used 20 intensity levels. The isodose lines calculated by both systems agreed within about 4% or a shift in isodose lines within about 0.3 cm. These small discrepancies were thought to be partially due to the approximations used by Corvus in accounting for the effect of MLC leaf leakage. Considering that the average leaf leakage is about 1.5% for a 6 MV beam and the total MU required to deliver an IMRT field is about three times more than that required by a conventional field, the estimated accumulated leaf leakage beneath a completely closed leaf pair is about 4.5%. Thus, a few per cent of the observed dose difference may be attributed to the difference in leaf leakage implementation between Corvus and Monte Carlo.

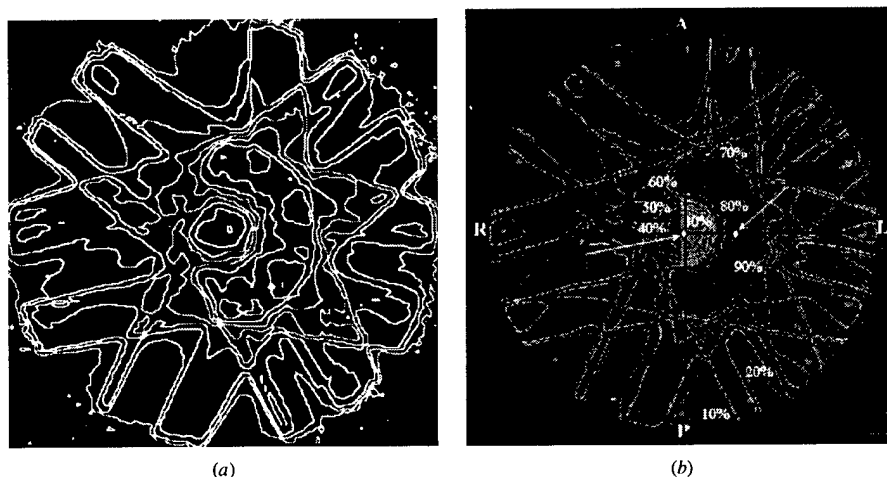


Figure 1. Comparison of 6 MV photon beam (seven co-planar fields at 26, 77, 180, 231, 283 and 334° gantry angles) dose distributions in a water cylinder calculated by Monte Carlo (a) and Corvus (b). The differences between the Corvus calculations and measurements using an ion chamber are shown for certain locations (arrows).

3.2. Comparisons in CT phantoms

In this work, we have compared the dose distributions calculated by Monte Carlo and the Corvus FSPB algorithm for various treatment sites to identify potential treatment situations that may benefit from dose accuracy improvements. In the following examples, we show two typical IMRT treatment plans computed by the Corvus inverse planning system and verified by the Monte Carlo system.

3.2.1. Prostate. To explore the effect of photon and electron transport on IMRT dose calculations, we show in figure 2 an IMRT prostate treatment plan calculated by Monte Carlo simulation and the Corvus system. The plan was generated using the Corvus system for 15 MV photon beams with nine gantry angles (20, 60, 100, 140, 220, 260, 300 and 340°). The beam intensity was modulated using a Varian dynamic MLC with 80 leaves. In both calculations, the isodose lines represent the absolute dose values in the patient. It can be seen that the dose values in the target (the prostate) agreed very well between the Corvus calculations and the Monte Carlo simulations. Similar results were found for six other prostate cases compared (not shown). The difference in the average dose to the target volume was 1.6% between Monte Carlo and Corvus and the maximum dose difference in the target dose was 3.4%. This confirms that both calculation algorithms can predict dose distributions in homogeneous phantoms accurately. The dose values in the nearby critical structures also agreed to 3–7% of the prescribed target dose. For the case shown in figure 2(c), the maximum difference was about 3 Gy in the rectum. However, other cases also showed the maximum differences in the bladder. These differences may be considered to be clinically acceptable.

The dose values in the regions near the bony structures sometimes showed a difference of a few per cent between the Corvus and the Monte Carlo calculations. These discrepancies may be partially explained by the effect of electron backscatter from the bone (high atomic number and high density) to the soft tissue, which was accurately accounted for by the Monte Carlo

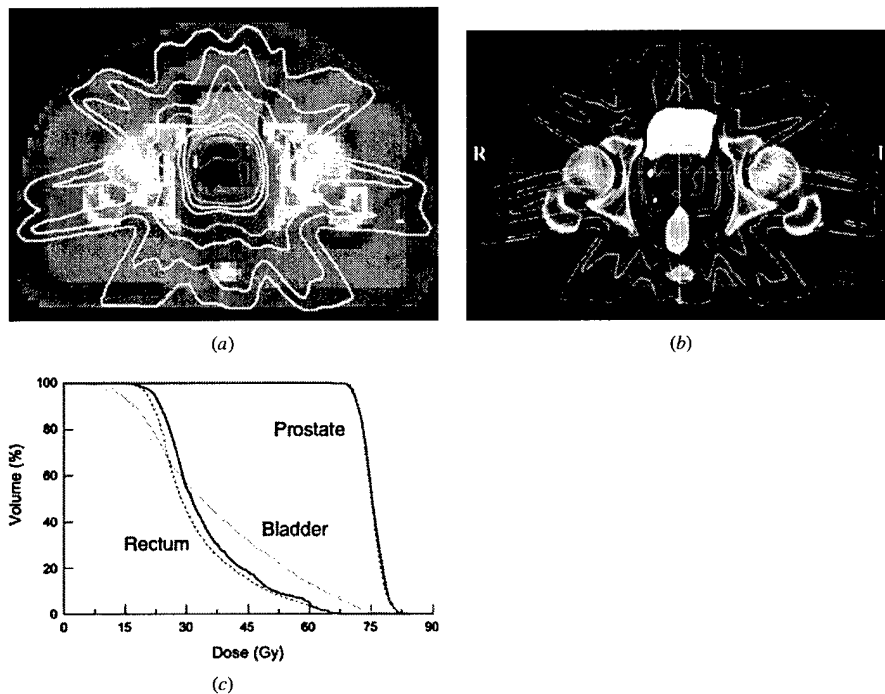


Figure 2. Comparison of 15 MV photon beam (nine co-planar fields) dose distributions for a prostate treatment calculated by Monte Carlo (a) and Corvus (b). The isodose lines are 77.2, 70.0, 56.1, 48.9, 35.0, 27.8, 21.1 and 13.9 Gy respectively in each figure. (c) The dose volume histograms as calculated by Monte Carlo (full curves) and Corvus (broken curves).

simulation but not in a FSPB algorithm. There have been several Monte Carlo studies in the literature showing similar discrepancies between the Monte Carlo algorithm and the correction based calculation algorithms in dose build-up or build-down regions near air cavities, lung and large bony structures (DeMarco *et al* 1998, Mohan 1997, Wang *et al* 1996, Ma *et al* 1999). It should be mentioned that the difference in the dose to the bone was partially due to the fact that the conventional dose calculation algorithms usually used water as the phantom material and the inhomogeneity corrections were computed using varying electron density (based on the CT numbers) while the Monte Carlo algorithm used different materials such as air, tissue, lung and bone with varying mass density calculated from the CT data. If we convert the dose to the bone material to the dose to tissue using the stopping power ratio for bone to tissue (assuming the same electron energy fluence) the dose in the bone regions will be about 3.5% higher for soft bone and about 10% higher for compact bone (ICRU 1984, Siebers *et al* 2000). We will discuss this issue further in section 4. Anyway, the dose in the surrounding tissue regions should not be affected by the conversion, which was mainly caused by the perturbation of the electron fluence by the nearby inhomogeneous anatomy.

3.2.2. Vertebra. Figure 3 shows the dose distributions for the treatment of the vertebra calculated by both Monte Carlo simulation and the Corvus system. The plan was generated using the Corvus system for 15 MV photon beams with nine co-planar gantry angles (20, 55,

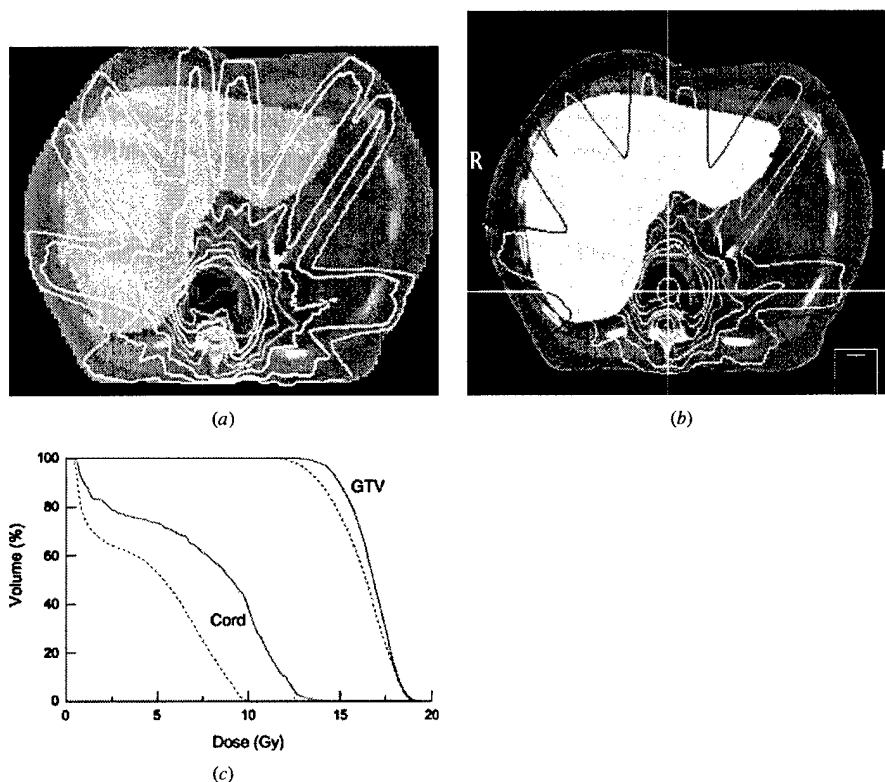


Figure 3. Dose distributions for the treatment of the vertebra calculated by Monte Carlo (a) and by Corvus (b) for 15 MV photons (nine co-planar fields). The isodose lines are 17.6, 15.6, 13.7, 11.7, 9.8, 7.8, 5.9, 3.9 and 2.0 Gy respectively in each figure. (c) The dose volume histograms as calculated by Monte Carlo (full curves) and Corvus (broken curves) for the target and the spinal cord.

90, 140, 180, 220, 260, 300 and 340°). The intensity was modulated using a Varian dynamic MLC with 80 leaves. The prescribed target dose was 18 Gy. The maximum dose in the target showed good agreement between Corvus and Monte Carlo (figure 3(c)). The Monte Carlo dose distribution showed slightly better target coverage than the Corvus dose distribution (a 2 Gy difference in the minimum target dose). Because the cord was sometimes immediately next to the target region the maximum cord dose was expected to be equal to or higher than the minimum target dose. This was confirmed by the Monte Carlo simulations (see figure 3(c)). In the regions near large bony structures (such as the cord) differences of more than 20% of the prescribed target dose could be seen between the Corvus calculation (10 Gy) and the Monte Carlo simulation (14 Gy). The difference in the dose to the cord was thought to be due in part to electron scattering from the surrounding bone, which could not be modelled properly using the FSPB algorithm. Another possible reason might be due to the implementation of the heterogeneity and leaf leakage corrections in the FSPB model. Although the photon beams were optimized to avoid the cord, electrons could reach the cord and the dose to the cord could be enhanced due to the high-density material surrounding it and/or photon leaf leakage that is not included in the dose calculation during the inverse planning process. Further studies are

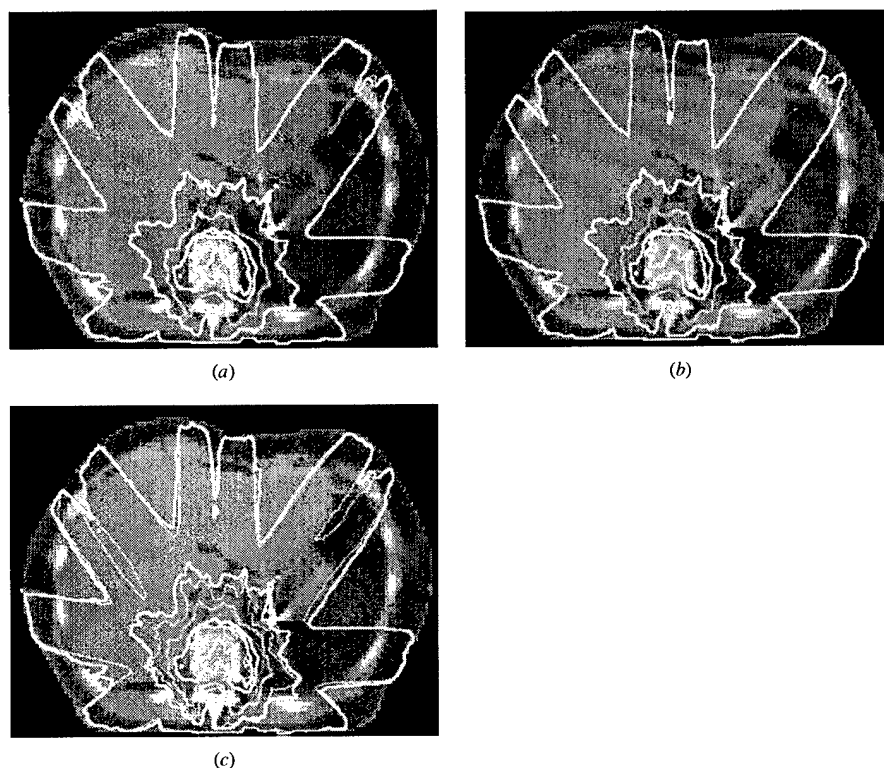


Figure 4. Dose distributions for different tissue types and material densities: (a) tissue and bone with variable density (thick line) and tissue with unity density (thin line); (b) tissue and bone with variable density (thick line) and tissue with variable density (thin line); and (c) tissue and bone with variable density (thick line) and tissue with unity density and bone with 10 g cm^{-3} density (thin line). The phantom geometry and beam arrangements are the same as in figure 3. The isodose lines are given as 10, 30, 50, 70 and 80% of the prescribed target dose.

needed to understand these differences if more access to the FSPB and leaf sequence algorithms in the Corvus system is available.

4. Discussion

Several important factors may affect the Monte Carlo calculated dose distributions and the DVH curves. First, the isodose lines and the DVH curves are affected by the materials used in the patient CT phantom, i.e. whether we plot dose to tissue only or dose to any material (such as air, tissue or bone). It seems reasonable that our previous experience was based on dose to tissue (or dose to water, the difference between the two is within 1%) and therefore the dose values should be expressed as dose to tissue. However, it can also be argued that the real dose to the biological material such as bone should be given whenever possible. Only in this way can the relationship between the 'old' practice and new experience be established.

To understand the effect of the conversion of the dose to different materials, we show in figure 4 the dose distributions calculated using Monte Carlo with different materials and

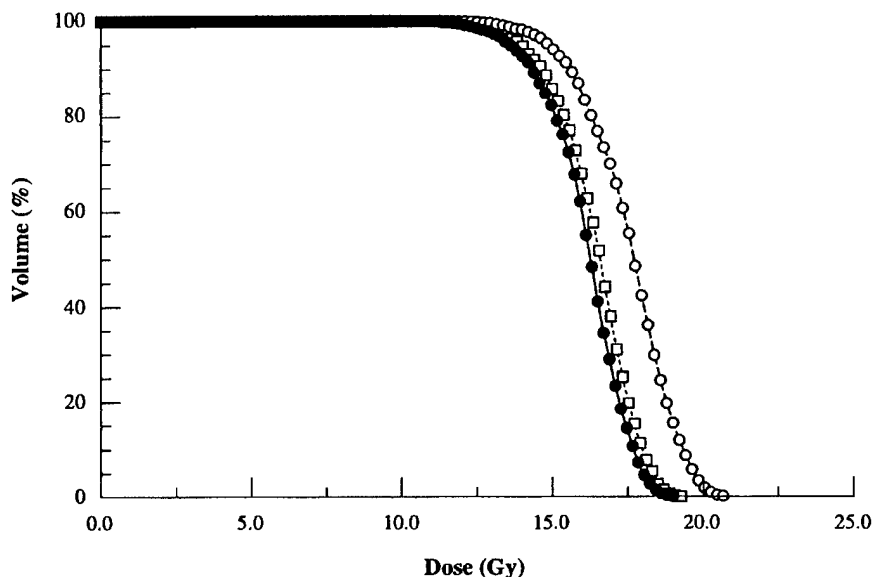


Figure 5. Dose volume histograms for the GTV in figure 3. Full circles are obtained using a CT phantom consisting of air, tissue and bone of variable density with dose calculated for each material. Open circles are obtained using the same phantom with dose converted to tissue using the stopping power ratios of tissue to bone or tissue to air. Open squares are obtained using a phantom consisting of only tissue of variable density.

density configurations for the IMRT case shown in figure 3. In figure 4(a), the dose distribution was calculated using tissue with unit density and air. This phantom should not show any heterogeneity effect due to the change in tissue (or bone) densities. In figure 4(b), the dose distribution was calculated using air and tissue with variable density converted from the CT data. This is similar to the phantom used by the Corvus system. In figure 4(c), the dose distribution was calculated with air, unit density tissue and 10 g cm^{-3} density bone. For comparison, the dose distribution calculated using air, tissue and bone with proper densities converted from the CT data is shown in each figure. The isodose curves were computed by normalizing the dose values to the prescribed target dose. The differences in the isodose lines in figure 4(a) and (b) are small (2–3%). This is also clearly shown in figure 5 for the target DVHs. The difference between dose to tissue and dose to bone would be about 3.5% for soft bone and about 10% for hard bone (Siebers *et al* 2000) if converted using the stopping power ratios for tissue to bone (or soft bone) at these beam qualities, assuming the same electron energy fluence. Clearly, such conversion is not equivalent to performing the Monte Carlo simulation using a water (or tissue) phantom with variable mass (or electron) density. It is known that electron backscattering from the high atomic number materials may perturb the dose in tissue near the tissue–bone interface. This effect is less significant when dose values are averaged over course scoring volumes (0.3–0.4 cm voxels). In figure 4(c), the density of bone was artificially increased to 10 g cm^{-3} which caused significant attenuation of the beams and therefore altered the doses behind the bones. The effects on the surface doses are smaller than for the high dose regions. The maximum dose for the artificially high-density bone geometry is about 15% lower than that for the phantom with normal material density.

Although Monte Carlo dose calculations are time-consuming it is possible to use Monte Carlo calculated dose distributions to verify the IMRT treatment plans in order to detect any cases where the FSPB dose calculation algorithm as implemented in Corvus may fail to predict the dose perturbation effect near inhomogeneities. Monte Carlo simulation may also be used directly for IMRT beamlet distribution calculation as a practical solution to this problem. Our experiences show that a factor of two to three more Monte Carlo particle histories are needed for an IMRT treatment simulation compared with a conventional photon treatment simulation to achieve the same statistical uncertainty. This is because more monitor units are needed to deliver intensity modulated photon fields; more particles will be simulated in a Monte Carlo calculation but many of them will be stopped by the MLC leaves. Therefore, the CPU time per photon history for an IMRT simulation is less than that for a conventional field. Using the existing computing power (8 CPUs) of the Corvus system, the calculation time for a typical 'inverse plan' would be increased from the current 0.5–1 h to 2–4 h with two Monte Carlo calculations. The pre-optimization dose calculation will provide the beamlet distributions for the optimization process, which take into account the effect of the accelerator head scatter and inhomogeneous anatomy of the patient. The post-optimization dose calculation will include the effects due to leaf leakage, leaf scatter and photon backscatter into the monitor chamber after the sequence of MLC leaf movement and jaw positions has been generated. Further studies are under way on a Monte Carlo dose calculation based inverse planning system (Pawlicki *et al* 1999, Ma *et al* 2000).

5. Summary

We have implemented a Monte Carlo system for routine radiotherapy treatment planning dose calculations. In our previous publications we have shown that Monte Carlo simulations agreed with measurements to within 2% for various clinical beam set-ups in homogeneous and heterogeneous phantoms. Based on these results, we have moved one step nearer to using the Monte Carlo simulations to verify the IMRT dose distributions computed by the Corvus system, which employs a FSPB algorithm for beamlet dose calculations, assuming that the Monte Carlo simulations are accurate at the 2% level for patient phantoms built from CT data.

Our results showed that the FSPB algorithm was adequate for most of the IMRT cases where the target was not immediately adjacent to the critical structures. However, the FSPB algorithm may not accurately predict the dose distributions in and near inhomogeneities in some cases. The dose in the target volume calculated by the Corvus system differed from the Monte Carlo results by more than 5%, while the dose to the critical organ differed by more than 20% of the prescribed target dose for a few cases. This suggests that, for such cases, more accurate dose calculation algorithms than that currently implemented in Corvus should be used for intensity-modulated radiotherapy treatment planning.

Acknowledgments

We would like to acknowledge Varian Oncology Systems, Palo Alto, CA, for providing detailed information on the Varian Clinac linear accelerators and Nomos Corp., Sewickley, PA, for the inverse-planning system. We would like to thank our colleagues, Sam Brain, Todd Koumrian, Behrooz Tofighrad and Michael Luxton, for help with the computers and software support. We are grateful to Dr Iwan Kawrakow for the DOSXYZ_{SH} program to plot isodose distributions, and to Jinsheng Li and Michael Luxton for modifications to the program to display structures of interest and to compare two isodose distributions on the same plot.

This investigation was supported in part by grants CA78331 from the NIH, BC971292 from the DOD, Seed Cycle 1 from the RSNA Research and Education Fund, and a consortium agreement with the NumeriX, LLC.

References

- AAPM 1983 AAPM TG-21, A protocol for the determination of absorbed dose from high-energy photons and electrons *Med. Phys.* **10** 741
- Bielajew A F and Rogers D W O 1988 Variance-reduction techniques *Monte Carlo Transport of Electrons and Photons* ed T M Jenkins, W R Nelson, A Rindi, A E Nahum and D W O Rogers (New York: Plenum) pp 407-19
- Boesecke R, Doll J, Bauer B, Schlegel W, Pastyr O and Lorenz M 1988 Treatment planning for conformation therapy using a multileaf collimator *Strahlenther. Onkol.* **164** 151-4
- Boyer A L, Geis P B, Grant W, Kendall R and Carol M 1997 Modulated-beam conformal therapy for head and neck tumors *Int. J. Radiat. Oncol. Biol. Phys.* **39** 227-36
- Boyer A L, Xing L, Ma C-M, Curran B, Hill R, Holmes T and Bleier A 1999 Theoretical consideration of monitor unit calculations for intensity modulated beam treatment planning (abstract) *Med. Phys.* **26** 187-95
- Boyer A L, Xing L, Ma L and Forster K 1998 Verification and delivery of head and neck intensity modulated radiotherapy *Med. Phys.* **25** A200-1
- Brahme A 1988 Optimal setting of multileaf collimators in stationary beam radiation therapy *Strahlenther. Onkol.* **164** 343-50
- Brewster L, Mohan R, Mageras G, Burman C, Leibel S and Fuks Z 1995 Three dimensional conformal treatment planning with multileaf collimators *Int. J. Radiat. Oncol. Biol. Phys.* **33** 1081-89
- Chui C S, LoSasso T and Spirou S 1994 Dose calculations for photon beams with intensity modulation generated by dynamic jaw or multileaf collimators *Med. Phys.* **21** 1237-43
- Convery D J and Rosenbloom M E 1992 The generation of intensity-modulated fields for conformal radiotherapy by dynamic collimation *Phys. Med. Biol.* **37** 1359-74
- Convery D J and Webb S 1997 Calculation of the distribution of head-scattered radiation in dynamically-collimated MLC fields *Proc. 12th Int. Conf. on the Use of Computers in Radiation Therapy (Salt Lake City, UT)* pp 350-3
- Cunningham J R and Battista J J 1995 Calculation of dose distributions for x-ray therapy *Phys. Canada* **51** 190-218
- DeMarco J J, Solberg T D and Smathers J B 1998 A CT-based Monte Carlo simulation tool for dosimetry planning and analysis *Med. Phys.* **25** 1-11
- Fraass B A, McShan D L, Kessler M L, Matrone G M, Lewis J D and Weaver T A 1995 A computer-controlled conformal radiotherapy system. I: overview *Int. J. Radiat. Oncol. Biol. Phys.* **33** 1139-57
- Holmes T M, Bleier A, Carol M, Curran B, DeNisi J, Hill R, Kania A, Lalonde R, Larson L and Sternick E 1998 The Corvus dose model revealed (abstract) *Med. Phys.* **25** 144
- Holmes T M, Bleier A, Carol M, Curran B, Kania A, Lalonde R, Larson L and Sternick E 1997 The effect of MLC leakage on the calculation and delivery of intensity modulated radiotherapy (abstract) *Med. Phys.* **24** 997
- Hounsfield A R 1998 Monitor chamber backscatter for intensity modulated radiation therapy using multileaf collimators *Phys. Med. Biol.* **43** 445-54
- ICRU 1984 Radiation dosimetry: stopping powers for electrons and positrons *ICRU Report 37* (Bethesda, MD: ICRU)
- Kapur A, Ma C-M, Mok E and Findley D 1997 Characterization of small field electron beams for radiotherapy using Monte Carlo simulations *Proc. 12th Int. Conf. on the Use of Computers in Radiation Therapy (Salt Lake City, UT)* pp 157-8
- Kapur A, Ma C-M, Mok E, Findley D and Boyer A L 1998 Monte Carlo calculations of clinical electron beam output factors *Phys. Med. Biol.* **43** 3479-94
- Kutcher G J, Mageras G S and Leibel S A 1995 Control, correction and modeling of set-up errors and organ motion *Semin. Radiat. Oncol.* **5** 134-45
- Leibel S A, Kutcher G J and Mohan R *et al* 1992 Three-dimensional conformal radiation therapy at the Memorial Sloan-Kettering Cancer Center *Semin. Radiat. Oncol.* **2** 274-89
- Ling C C *et al* 1996 Conformal radiation treatment of prostate cancer using inversely-planned intensity-modulated photon beams produced with dynamic multileaf collimation *Int. J. Radiat. Oncol. Biol. Phys.* **35** 730-41
- LoSasso T, Chui C S, Kutcher G J, Leibel S A, Fuks Z and Ling C C 1993 The use of multileaf collimators for conformal radiotherapy of carcinomas of the prostate and nasopharynx *Int. J. Radiat. Oncol. Biol. Phys.* **25** 161-70
- Ma C-M 1998 Characterization of computer simulated radiotherapy beams for Monte Carlo treatment planning *Radiat. Phys. Chem.* **53** 329-44

- Ma C-M, Mok E, Kapur A and Findley D 1997 Improvement of small-field electron beam dosimetry by Monte Carlo simulations *Proc. 12th Int. Conf. on the Use of Computers in Radiation Therapy (Salt Lake City, UT)* pp 159–62
- Ma C-M, Mok E, Kapur A, Pawlicki T A, Findley D, Brain S, Forster K and Boyer A L 1999 Clinical implementation of a Monte Carlo treatment planning system for radiotherapy *Med. Phys.* **26** 2133–43
- Ma C-M, Pawlicki P, Lee M C, Jiang S B, Li J S, Deng J, Yi B, Mok E and Boyer A L 2000 Energy- and intensity-modulated electron beams for radiotherapy *Phys. Med. Biol.* **45** 2293–311
- Ma C-M, Reckwerdt P, Holmes M, Rogers D W O and Geiser B 1995 DOSXYZ users manual *National Research Council Report PIRS-0509(B)* (Ottawa: NCRC)
- Mackie T R, Holmes T W, Reckwerdt P J and Yang J 1995 Tomotherapy: optimized planning and delivery of radiation therapy *Int. J. Imaging Syst. Technol.* **6** 43–55
- Mackie T R, Reckwerdt P, McNutt T, Gehring M and Sanders C 1996 Photon beam dose calculations *Teletherapy: Present and Future* ed T R Mackie and J R Palta (Madison, WI: Advanced Medical Publishing) pp 103–35
- Mackie T R, Reckwerdt P and Papanikolaou N 1995 3-D photon beam algorithms *3-D Radiation Treatment Planning and Conformal Therapy* ed J A Purdy and B Emami (Madison, WI: Medical Physics Publishing) pp 201–22
- Mackie T R *et al* 1994 The OMEGA project: comparison among EGS4 electron beam simulation, 3D Fermi-eyges calculations and dose measurements *Proc. 11th Int. Conf. on the Use of Computers in Radiation Therapy (Manchester, UK)* pp 152–3
- Mageras G S *et al* 1994 Initial clinical experience with computer-controlled conformal radiotherapy using the MM50 microtron *Int. J. Radiat. Oncol. Biol. Phys.* **30** 971–8
- McShan D L, Fraass B A, Kessler M L, Matrone G M, Lewis J D and Weaver T A 1995 A computer-controlled conformal radiotherapy system. II: sequence processor *Int. J. Radiat. Oncol. Biol. Phys.* **33** 1159–72
- Mohan R 1997 Why Monte Carlo? *Proc. 12th Int. Conf. on the Use of Computers in Radiation Therapy (Salt Lake City, UT)* pp 16–18
- Nelson R, Hirayama H and Rogers D W O 1985 The EGS4 code system *Stanford Linear Accelerator Center Report SLAC-265* (Stanford, CA: SLAC)
- Oldham M and Webb S 1997 Intensity-modulated radiotherapy by means of static tomotherapy: a planning and verification study *Med. Phys.* **24** 827–36
- Pawlicki T A, Jiang S B, Deng J, Li J S and Ma C-M 1999 Monte Carlo calculated beamlets for photon beam inverse planning (abstract) *Med. Phys.* **26** 1064–5
- Powlis W D, Smith A, Cheng E *et al* 1993 Initiation of multileaf collimator conformal radiation therapy *Int. J. Radiat. Oncol. Biol. Phys.* **25** 171–9
- Rogers D W O and Bielajew A F 1990 Monte Carlo techniques of electrons and photons for radiation dosimetry *Dosimetry of Ionizing Radiation* vol 3, ed K Kase, B E Bjarnagard and F H Attix (New York: Academic) pp 427–539
- Rogers D W O, Faddegon B A, Ding G X, Ma C M, Wei J S and Mackie T R 1995a BEAM: a Monte Carlo code to simulate radiotherapy treatment units *Med. Phys.* **22** 503–25
- Rogers D W O, Ma C M, Ding G X and Walters B 1995b BEAM users manual *National Research Council Report PIRS-0509(A)* (Ottawa: NRC)
- Siebers J V, Keall P J, Nahum A E and Mohan R 2000 Converting absorbed dose to medium to absorbed dose to water for Monte Carlo based photon beam dose calculations *Phys. Med. Biol.* **45** 983–95
- Wang L, Chui C and Lovelock M 1998 A patient-specific Monte Carlo dose-calculation method for photon beams *Med. Phys.* **25** 867–78
- Wang X, Spirou S, LoSasso T, Stein J, Chui C and Mohan R 1996 Dosimetric verification of intensity modulated fields *Med. Phys.* **23** 317–28
- Wong J W and Purdy J A 1990 On the methods of inhomogeneity corrections for photon transport *Med. Phys.* **17** 807–14
- Webb S 1992 Optimization by simulated annealing of three-dimensional conformal treatment planning for radiation fields defined by multi-leaf collimator: II. Inclusion of two-dimensional modulation of x-ray intensity *Phys. Med. Biol.* **37** 1689–704
- 1997 *The Physics of Conformal Radiotherapy: Advances in Technology* (Bristol: Institute of Physics Publishing)
- Xing L, Curran B, Hill R, Holmes T, Ma L, Forster K and Boyer A L 1999 Dosimetric verification of a commercial inverse treatment planning system *Phys. Med. Biol.* **44** 463–78
- Yu C X, Symons J M, Du M N, Martinez A A and Wong J W 1995 A method for implementing dynamic photon beam intensity modulation using independent jaws and multileaf collimators *Phys. Med. Biol.* **40** 769–87

Monte Carlo characterization of clinical electron beams in transverse magnetic fields

Michael C Lee and Chang-Ming Ma

Department of Radiation Oncology, Stanford University School of Medicine, Stanford, CA 94305, USA

Received 16 May 2000

Abstract. Monte Carlo simulations were employed to study the characteristics of the electron beams of a clinical linear accelerator in the presence of 1.5 and 3.0 T transverse magnetic fields and to assess the possibility of using magnetic fields in conjunction with modulated electron radiation therapy (MERT). The starting depth of the magnetic field was varied over several centimetres. It was found that peak doses of as much as 2.7 times the surface dose could be achieved with a 1.5 T magnetic field. The magnetic field was shown to reduce the 80% and 20% dose drop-off distance by 50% to 80%. The distance between the 80% dose levels of the pseudo-Bragg peak induced by the magnetic field was found to be extremely narrow, generally less than 1 cm. However, by modulating the energy and intensity of the electron fields while simultaneously moving the magnetic field, a homogeneous dose distribution with low surface dose and a sharp dose fall-off was generated. Heterogeneities are shown to change the effective range of the electron beams, but not eliminate the advantages of a sharp depth-dose drop-off or high peak-to-surface dose ratio. This suggests the applicability of MERT with magnetic fields in heterogeneous media. The results of this study demonstrate the ability to use magnetic fields in MERT to produce highly desirable dose distributions.

1. Introduction

The current trend in radiation therapy towards conformal techniques requires the ability to deposit high dose to a given target region, while sparing surrounding normal tissue. Depth-dose distributions approaching the ideal of a step function are available from the use of protons, heavy ions and exotic particles such as π mesons. However, at present, these treatment modalities are of greatly restricted use due to the extreme expense and technical complexity of the accelerator systems. In contrast, an electron linear accelerator may cost a factor of a hundred less than a proton accelerator, and be orders of magnitude more compact; electron accelerators are thus found in most radiation therapy centres. Furthermore, while photon beam intensity-modulated radiation therapy (IMRT) allows effectively arbitrary dose distributions, the requirement of several centimetres of tissue for electron build-up makes IMRT of shallow tumours difficult. Thus, at present, electron beams hold many advantages for the treatment of shallow tumours such as those in the breast and head and neck.

Additionally, a recent Monte Carlo investigation (Ma *et al* 2000b) into modulated electron beam radiation therapy (MERT) has shown that the use of non-uniform intensity profiles and multiple electron beam energies will allow highly conformal dose delivery to shallow targets. Conformity is achieved laterally via an electron multileaf collimator (Lee *et al* 2000a, b) and in the depth direction by means of energy and intensity modulation. This has been

shown to be particularly useful in treatment of the intact breast. MERT would avoid both the problems of dose delivery to the contralateral breast and the small, very high-dose regions in the lung.

Unfortunately, while electron beams exhibit rapid drops in depth-dose distributions relative to photon beams, the distance between the end of the therapeutically useful range and the practical range of the electrons may still be of the order of centimetres. Thus, while MERT delivers a highly conformal dose to the target, because of the low density of the lung MERT exposes much of the lung to low doses of radiation (less than 50% of the overall maximum.) The biological impact of this low-dose region is as yet unclear; however, it is likely that the clinical outcome will improve if the lung dose is reduced. It is thus of paramount importance to investigate methods that may allow improved depth-dose distributions from electron beams.

Numerous studies have been performed to examine the possibility of using magnetic fields to tailor the dose distributions from electron beams. Two general methods for two distinct purposes have been proposed: magnetic fields directed along the axis of the beam (longitudinal) for lateral confinement of penumbras and stability in the presence of inhomogeneities (Weinhous *et al* 1985, Bielajew 1993), and fields directed orthogonally to the beam (transverse) to reduce the dose penumbra in the depth direction. In this work, only the effects of transverse magnetic fields are considered, as the primary goal is restriction of electron penetration. Transverse fields were suggested by Sempert (1960) and early Monte Carlo studies were performed by Shih (1975), demonstrating the ability to create a sharp depth-dose drop-off. Experimental investigation ensued, including work by Whitmire *et al* (1977), who conducted experiments with 22 and 28 MeV beams in 1 T fields. Nath and Schulz (1978) performed experimental investigations using 2.05 T transverse magnetic fields to increase the dose peak and sharpen the dose drop-off of an electron beam of less than 50 MeV. Further work has explored the effect of inhomogeneities (Paliwal *et al* 1978, Whitmire *et al* 1978). Recent interest in Monte Carlo investigations has been revived by the work of Nardi and Barnea (1999), using the ITS/ACCEPTM system to demonstrate the use of modern Monte Carlo techniques to simulate monoenergetic electron beams in a magnetic field positioned at a fixed depth.

This work aims to use Monte Carlo simulations to investigate the effects of transverse magnetic fields on clinical electron beams, and to examine the possibility of combining this technique with MERT. In particular, the effect of different field strengths and field locations is examined. The changes in dose distributions are quantified with a focus on the effect on surface dose and the dose fall-off. A modified system of MERT is presented in which magnetic fields are used in conjunction with intensity modulation to generate highly conformal dose regions with low surface dose and rapid depth-dose fall-off. The effect of heterogeneities on the dose distribution is also described.

2. Materials and methods

2.1. Principles and theory

When an electron enters a magnetic field, it immediately begins to travel in a curved path as dictated by the Lorentz force and eventually exits the field after moving along a semicircular path. If energy loss is included, then the particle will spiral towards smaller and smaller radii. By this action, an electron can be caused to deposit much of its energy in a localized region. In particular, the electron penetration into the field is approximately restricted to less than a distance defined by the radius of gyration, r_g .

In the limit of constant energy (small step size Δl), in the presence of a magnetic field defined by \vec{B} , a particle direction vector \vec{v}_0 is replaced with (Nelson *et al* 1985)

$$\vec{v} = \vec{B}(\vec{v}_0 \cdot \vec{B}) + [\vec{v}_0 - \vec{B}(\vec{v}_0 \cdot \vec{B})] \cos \frac{\Delta l}{r_g} - \vec{v}_0 \times \vec{B} \sin \frac{\Delta l}{r_g} \quad (1)$$

As Monte Carlo simulated transport occurs in short, discrete steps, this equation is particularly relevant to this study.

It has been shown by Bielajew (1993) that the synchrotron radiation due to the bending of electron paths at the energies of interest is trivial: of the order of 0.1–1 eV additional stopping power. Thus, both this added stopping power and synchrotron photon dose deposition are taken to be zero in this study.

One may generate a simple mathematical description of the expected effect of the magnetic fields on depth-dose distributions, before any Monte Carlo simulations are performed. Putting the unperturbed depth-dose profile in a vector \vec{x} and the depth-dose profile in a magnetic field in a vector \vec{b} , there exists a transformation matrix U such that

$$U\vec{x} = \vec{b} \quad (2)$$

with U upper triangular with columns that sum to unity. The effect of operating on \vec{x} with U is that below some row of \vec{x} , that is, beyond a given depth, there is a 'folding back' of energy deposition, such that some portion of the energy that would otherwise be deposited at greater depths will now be deposited earlier. However, because the overall energy of the system must be conserved, the columns of the transformation matrix U must have unit sum. Additionally, the magnetic field cannot cause electrons to deposit energy further downstream than they otherwise would, hence the upper-diagonal nature of the matrix. It will be seen the effect of the magnetic field is a function of the incident energy (spectrum), the depth the magnetic field begins at, and the strength of the field. In principle, if such a function could be derived, the effects of magnetic fields could be computed very rapidly. However, for the purposes of this work, such analytical formulations are considered only to anticipate the form of the depth-dose distributions that will be generated by Monte Carlo simulations.

2.2. Monte Carlo simulations

Note that in all subsequent sections, for brevity and clarity, the term 'beam' will be used to describe the incident flux of electrons, i.e. the electron beam, while 'field' will refer to the magnetic field.

Source-parameter descriptions of electron beams were obtained according to a procedure described elsewhere (Kapur *et al* 1998, Jiang *et al* 2000, Lee *et al* 2000c) and summarized here. Electron beam simulations of a Varian Clinac 2100C (Varian Oncology Systems, Palo Alto, CA) were performed using the EGS4/BEAM user code, (Nelson *et al* 1985, Rogers *et al* 1995) using vendor supplied geometries. The simulation code and geometry employed have been previously shown to provide agreement with measured data of better than 2% in transverse profiles and depth-dose curves for the three nominal energies simulated: 6, 12 and 20 MeV (Kapur *et al* 1998). Phase space files were obtained above the last scraper of electron applicators. Source-parameter files were then obtained by using the BEAMDP program (Ma and Rogers 1997) and used in all future dose calculations. The four-source model used in this study is described in detail in Jiang *et al* (2000). The source-parameter files have also been shown to agree with the measured data to better than 2% in depth-dose and profiles (Lee *et al* 2000c).

The macro package for electromagnetic transport developed by Bielajew (1987, 1993) were implemented into the EGS4/MCDOSE code (Ma *et al* 2000a). The three-dimensional

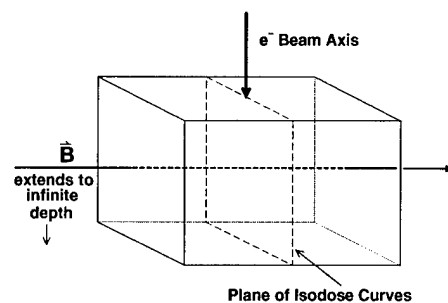


Figure 1. The geometry of the simulated system. The magnetic field vector is orthogonal to the electron beam axis, and is normal to the plane shown in the isodose curves. As shown, the direction of electron deflection is out of the page. The magnetic field region is a semi-infinite slab, i.e. all points below a given depth are assigned the same magnetic field vector.

dose distributions were examined using STATDOSE (McGowan *et al* 1996). Verification of the implementation was performed by computing longitudinal magnetic fields for 20 MeV electrons, as per Bielajew (1993) and 15 MeV monoenergetic beam in fields of varying magnitude, as per Nardi and Barnea (1999) using ITS/ACCEPTM. The agreement was better than 2% in all cases.

Pencil beams were simulated by restricting the particles to a single initial track. Specifically, a monoenergetic parallel beam was used, with a vanishing aperture size. The voxel geometry employed for these calculations was $1 \times 1 \times 1 \text{ mm}^3$. The narrow beams were simulated by using the source-parameter file for a $6 \times 6 \text{ cm}^2$ applicator and transporting particles through a $3 \times 3 \text{ cm}^2$ Cerrobend cut-out before entering the phantom. The $10 \times 10 \text{ cm}^2$ open fields were simulated with the appropriate source-parameter file, with the last scraper included in the MCDOSE simulation. The voxels for the narrow and broad fields were 2 mm in the depth direction, 4 mm in the axis orthogonal to the beam and magnetic field and 10 mm in the direction of the magnetic field. When the effects of inhomogeneities were considered, specific voxels in the phantom were converted to either air, or ICRP standard bone. In all cases, the nominal source-to-surface distance (SSD), defined from the photon target to the phantom surface) was 100 cm.

In all cases, the magnetic field was directed orthogonally to the electron beam axis, and normal to the plane shown in the isodose curves. The geometry is shown in figure 1.

All Monte Carlo simulations were performed on various elements of a suite of 22 Pentium Pro (200 MHz) and 10 Pentium III (450 MHz) CPUs, all running EGS4, BEAM and MCDOSE under the Linux operating system. All simulations utilized an electron cut-off of 0.7 MeV total energy and a photon cut-off of 10 keV, below which all remaining energy was deposited on the spot. PRESTA extensions were employed for step length calculations (Bielajew and Rogers 1987). In general, it was found that 10×10^6 electron histories were sufficient to provide a statistical error of less than 1% (1σ). The overall speed of calculation was reduced by approximately 50% relative to an identical simulation with no magnetic field in place.

2.3. Optimization

A one-dimensional optimization routine was implemented to examine the feasibility of combining fields such that the narrow dose peaks were spread out to several centimetres.

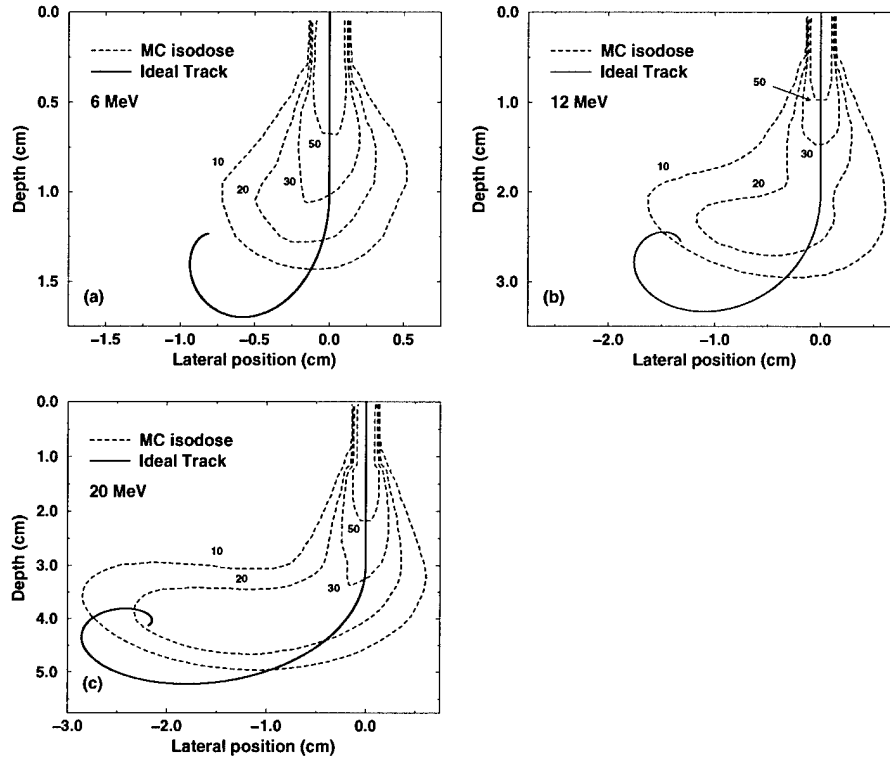


Figure 2. The theoretically derived track of an unscattered electron passing through water in the presence of a 1.5 T magnetic field, overlaid on isodose curves computed using the Monte Carlo method for a pencil beam: (a) 6 MeV with magnetic field beginning at 1 cm depth, (b) 12 MeV at 2 cm depth, (c) 20 MeV at 3 cm depth.

The dose at a given depth in the combined beam, D_{tot} was taken to be a linear combination of the dose at that depth of the individual beams. That is, for n different field/beam combinations

$$D_{\text{tot}}(z) = \sum_{i=1}^n x_i \cdot D_i(z). \quad (3)$$

Each beam i is given a weight x_i , which is determined based on the planned dose profile. To determine the weights $\vec{x} = (x_1, x_2, \dots, x_n)$, depth-dose curves were extracted from the $10 \times 10 \text{ cm}^2$ fields described earlier and each curve placed in the columns of a matrix \mathbf{A} . The desired depth-dose distribution was placed in a column vector \vec{b} and the system

$$\mathbf{A}\vec{x} \approx \vec{b} \quad (4)$$

was solved in a least-squares sense under non-negativity constraints. The method of solution utilized is described in detail in Lawson and Hanson (1974).

3. Results and discussion

The basic characteristics of electron beams in magnetic fields are explored in section 3.1 and section 3.2 by examining isodose curves and depth-dose curves. This demonstrates the

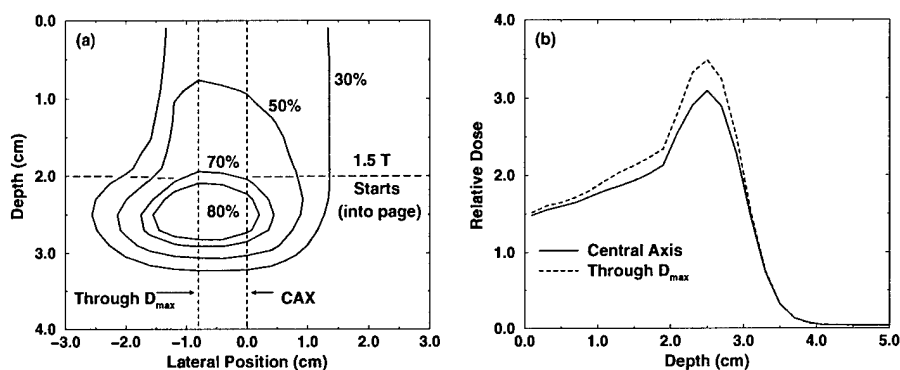


Figure 3. (a) Isodose curves for a 12 MeV electron beam collimated by a $6 \times 6 \text{ cm}^2$ applicator with a $3 \times 3 \text{ cm}^2$ Cerrobend cut-out in the presence of a 1.5 T magnetic field. Dotted lines represent the central axis and the ray passing through the dose maximum. The magnetic field is directed into the page. (b) The corresponding depth-dose curves for the central axis and the ray passing through the D_{max} .

general principles of electron beam therapy with magnetic fields, and provides evidence for the viability of the Monte Carlo transport code. Parameters for describing the depth-dose curves are presented in section 3.3 and the relevance of these parameters to MERT is discussed. An example of the application of MERT techniques to electron beams in magnetic fields is then given in section 3.4. Practical considerations important to actual application of magnetic field MERT are presented in sections 3.5 and 3.6.

3.1. Pencil beams and narrow beams

Monte Carlo calculations were performed in which electrons were constrained to travel down the same initial axis, i.e. a pencil beam. The resultant isodose curves are shown in figure 2. These figures clearly show the curvature of the electron beam dose distribution generally along the expected track. By superposition of many pencil beams along the lateral axis, it is clear that Bragg-peak-like dose peaks can be constructed.

Narrow fields, defined by $3 \times 3 \text{ cm}^2$ Cerrobend cut-outs on $6 \times 6 \text{ cm}^2$ applicators, were also simulated. What is apparent is that there is a significant shift of the dose peak off the central axis, as seen in figure 3. These data are presented primarily as a demonstration of the effects of the magnetic field, i.e. the curvature of the beam and the formation of a dose peak. However, it is difficult to make any definitive statements regarding depth-dose distributions because of the lack of equilibrium, as discussed below.

3.2. Broad beams

3.2.1. Electronic equilibrium. In the $3 \times 3 \text{ cm}^2$ narrow beams and the pencil beams, a state of lateral disequilibrium exists such that along any given axis, many times more particles are removed from the axis by the magnetic field than are replaced, as seen by the displacement of the dose peak in figure 3. In the limit of infinitely broad beams, there is equilibrium along any ray parallel to the beam axis. This is also true in the central region of broad, finite beams. This can be observed by computing the integral dose along a central axis of an unperturbed beam which is inherently large enough for equilibrium to exist. If lateral equilibrium exists, then the total energy deposited along this axis should not change when a magnetic field is applied.

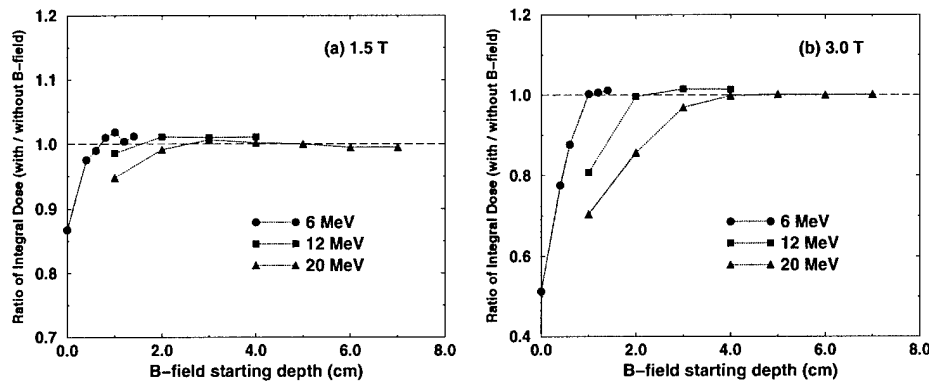


Figure 4. The ratio of energy deposited in the central axis voxels in the presence of a magnetic field to the energy deposited in a field-free system. This ratio is shown as a function of the magnetic field starting depth: (a) 1.5 T magnetic field, (b) 3.0 T.

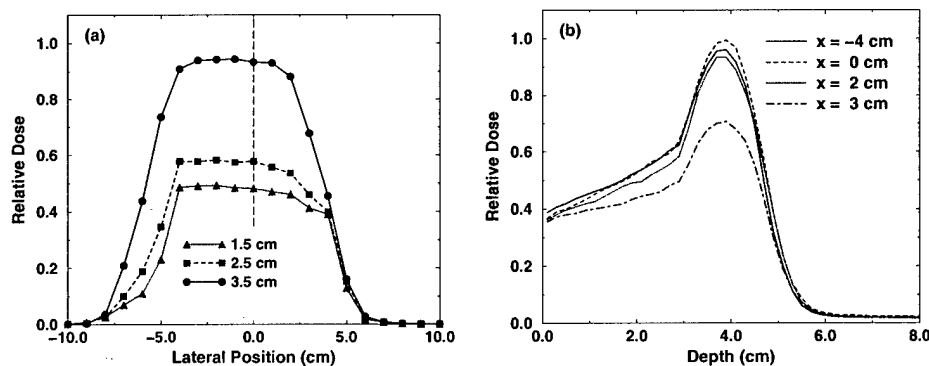


Figure 5. (a) Lateral dose profile for a 20 MeV beam in the presence of a 1.5 T magnetic field beginning at 3 cm depth. The axis being profiled is orthogonal to both the beam axis and the magnetic field. Shown are the profiles at 1.5, 2.5 and 3.5 cm depths. (b) Depth-dose curves for a 12 MeV beam in the presence of a 1.5 T magnetic field beginning at 3 cm depth. Shown are the central axis, and axes at -4, 0, 2 and 3 cm, where the positive direction is defined by $\vec{v} \times \vec{B}$ where \vec{v} is the original beam direction.

The Monte Carlo simulations suggest that for the energies investigated, a $10 \times 10 \text{ cm}^2$ beam is sufficiently broad to overcome the disequilibrium caused by the magnetic fields. As seen in figure 4, when the ratio of the energy deposited along the central axis in the magnetic field to the energy deposited in the zero-field case is less than unity, there is a net flow of electrons out of the field. This is in fact not an issue of lateral equilibrium in the standard sense, but a danger of using high-strength magnetic fields at shallow depths. What is occurring is that the field is strong enough that high-energy electrons are directed back towards the surface, and the primary beam actually exits the phantom via the front surface. Clearly, this situation is highly undesirable from both a treatment and radiation safety standpoint, and it is important to use a parameter such as the integral dose ratio to appreciate the minimum safe depth for a magnetic field. As expected, this depth is shallower at higher field strengths, as more electrons are turned back towards the surface. At 1.5 T, the minimum safe field depths are 0.4, <1 and

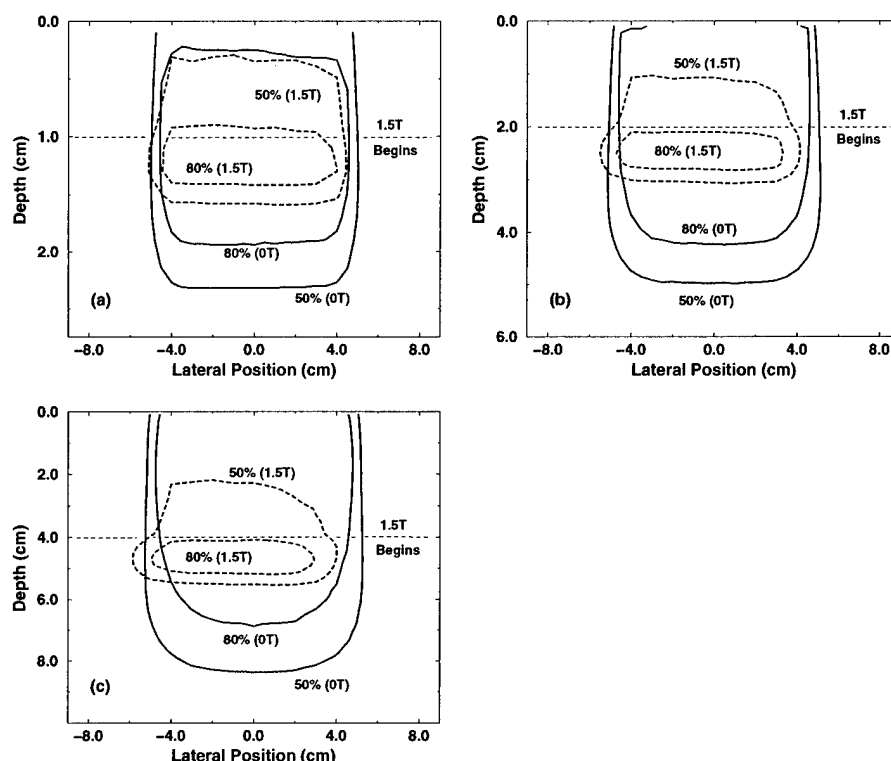


Figure 6. The 80% and 50% isodose curves for $10 \times 10 \text{ cm}^2$ fields. Both the zero-magnetic field case and the curves with a 1.5 T magnetic field directed out of the page are shown: (a) 6 MeV with magnetic field starting at 1 cm depth, (b) 12 MeV at 2 cm, (c) 20 MeV at 4 cm.

1 cm for 6, 12 and 20 MeV respectively. At 3.0 T, the depths are 1, 2 and 3 cm at 6, 12 and 20 MeV. Note that some points have values slightly greater than unity ($\sim 1\%$ higher.) This is partially due to the photon dose: if a magnetic field causes increased electron interactions near the surface, the photon dose curve is shifted towards the surface. Thus, relatively more photon dose will be deposited in the phantom in this case than in the field-free case, in which the photons exiting the phantom retain more energy. This effect in conjunction with statistical uncertainty leads to the slightly higher values.

Once the problem of beam loss is resolved, the original issue of lateral equilibrium can be considered. Evidence for the uniformity of the field is provided by examining the lateral dose profiles, as shown in figure 5(a). These profiles are taken along the axis orthogonal to both the magnetic field and original beam axis. It is seen that within the 7 cm region from -4.5 to 2.5 cm (each voxel was 1 cm in width), the dose was homogeneous to within 5.8% of the average dose in that region. Off-axis depth-dose curves are shown in figure 5(b). Here, the variations in the depth-dose curves caused by moving off of the central axis are comparable with those in open unperturbed $10 \times 10 \text{ cm}^2$ fields while within the equilibrium region (-4.5 to 2.5 cm), but it is clear that there is a rapid drop at 3 cm, where the electron dose has been shifted strongly in the positive direction, as shown. It is noted, however, that even at that position, there still exists a noticeable dose peak and dose drop-off.

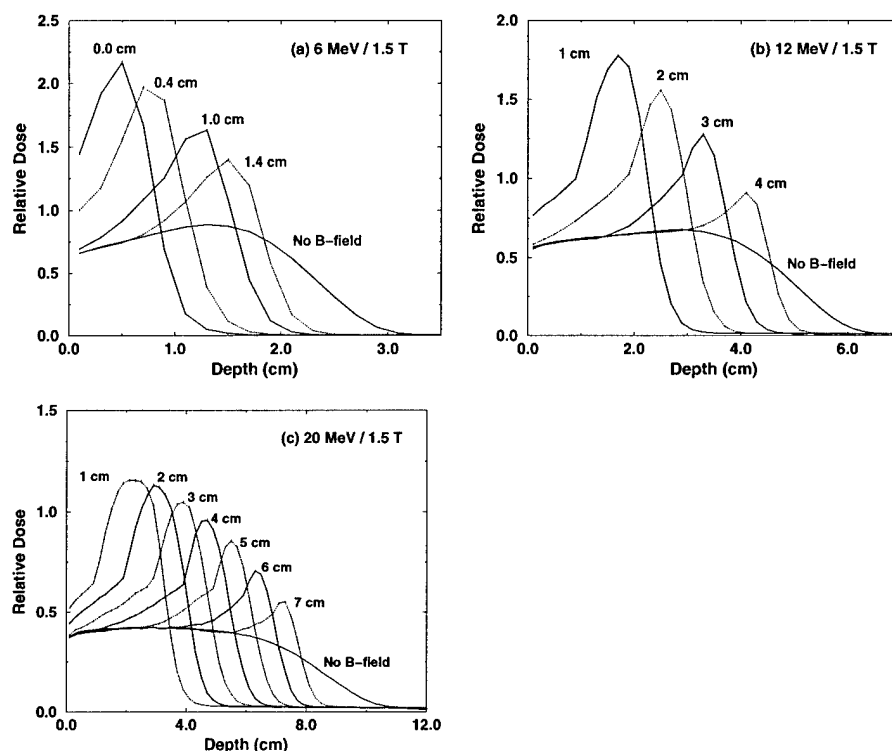


Figure 7. Central axis depth-dose curves for electron beams in the presence of a 1.5 T magnetic field. For each energy, the depth-dose curves are shown for different magnetic field starting depths. The vertical axis represents absolute dose in arbitrary units: (a) 6 MeV, (b) 12 MeV, (c) 20 MeV.

3.3. Dose profile parameters

Having thus established the electronic equilibrium of these systems, it is possible to examine the central-axis dose profiles. Isodose curves for $10 \times 10 \text{ cm}^2$ fields are shown in figure 6. Profiles along the central axis are displayed for 6, 12 and 20 MeV electron beams with the magnetic field positioned at several depths in figure 7 (1.5 T) and figure 8 (3.0 T). These broad electron fields were then characterized by consideration of the following parameters, defined graphically in figure 9:

d_B = the depth at which the magnetic field begins

$d_{80/80}$ = the width of the region bounded below by the 80% dose level

$d_{80/20}$ = the distance between the deepest 80% and the 20% dose levels

$R_{p/\text{eff}}$ = effective practical range, found by extrapolation of the drop-off region

SSF = surface sparing factor, defined by the ratio $D_{\text{max}}^{\text{voxel}} / D_{\text{surface}}^{\text{voxel}}$.

The values of $d_{80/80}$, $d_{80/20}$ and SSF for selected beam and field combinations, as well as the no magnetic field case, are shown in table 1 and are discussed in greater detail in the following sections.

3.3.1. Relationship between field strength and dose curves. Monte Carlo simulations were performed in which the magnetic field position was fixed but the field strength was varied.

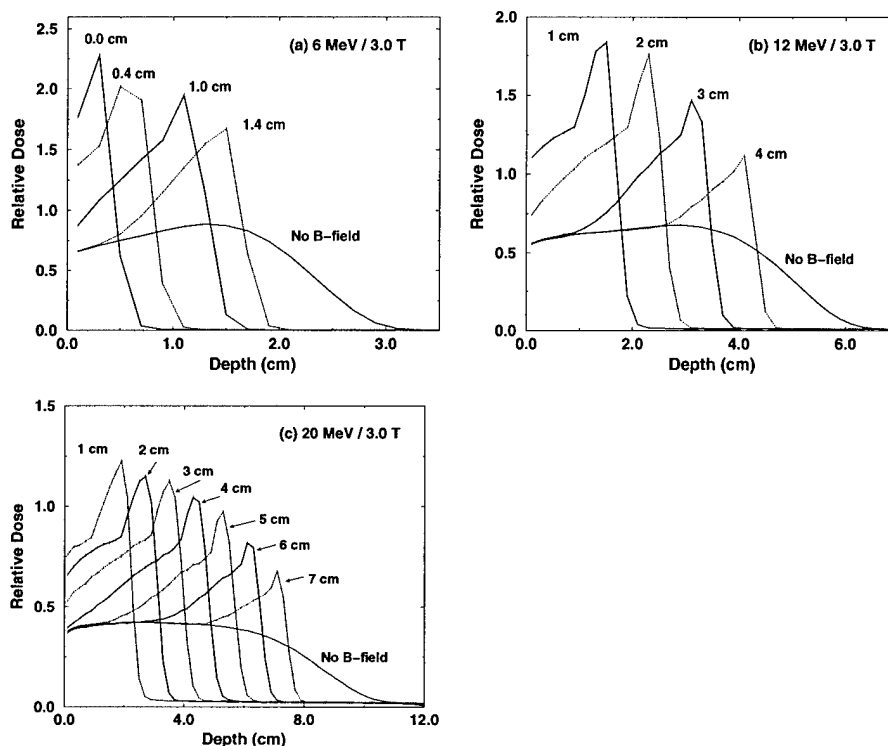


Figure 8. Central axis depth-dose curves for electron beams in the presence of a 3.0 T magnetic field. For each energy, the depth-dose curves are shown for different magnetic field starting depths. The vertical axis represents absolute dose in arbitrary units: (a) 6 MeV, (b) 12 MeV, (c) 20 MeV.

The effect of the changes on $d_{80/20}$ and SSF are shown in figure 10. As expected, the distance between the 80% and 20% dose falls with increasing field strength. While the simple Lorentz force equation may suggest a linear relationship, due to energy straggling and particle scattering, a more complex asymptotic relationship is observed. At approximately 1.5 T, the gains from increasing the magnetic field appear to be minimal.

The SSF shows a sigmoidal behaviour, with a period of rapid increase in SSF between 0.75 and 1.5 T, then a reduction in SSF at higher field strengths. This reduction occurs when the radius of gyration of the electron is too small. In those instances, instead of travelling in a spiral, the electron completes an approximate half-circle and exits the field at some angle, thus depositing dose at depths shallower than the magnetic field.

On the basis of these results, a field strength of 1.5 T was chosen as the primary field of interest. It is noted that the newest generation of interventional magnetic resonance imaging systems produce fields of this magnitude. Generally, simulations were also performed at 3.0 T to illustrate in detail the effects of changing magnetic field strengths.

3.3.2. $d_{80/80}$ —therapeutic range. The value of $d_{80/80}$ was taken as a measure of the portion of the beam that is clinically useful. Values for selected magnetic field positions are shown in table 1. This region is extremely narrow in all cases, with a maximum value of 1.7 cm for a 20 MeV beam with a 1.5 T field beginning at 1 cm depth. As a result, taken as is, these

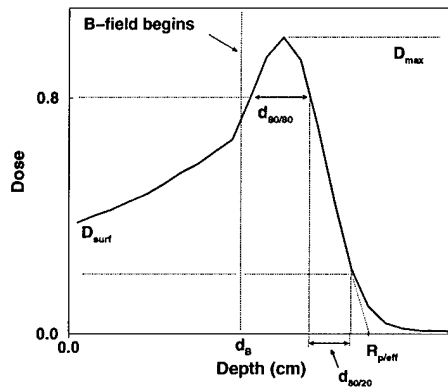


Figure 9. The parameters used to describe the depth-dose curves. $d_{80/80}$ is the distance between the two 80% isodose levels, $d_{80/20}$ is the distance between the deepest 80% and the 20% dose levels, d_B is the depth at which the magnetic field begins (it is taken to continue to infinite depth), D_{surf} and D_{max} are taken as approximate measures of the dose maximum and minimum along the axis, and are used to calculate the surface sparing factor (SSF).

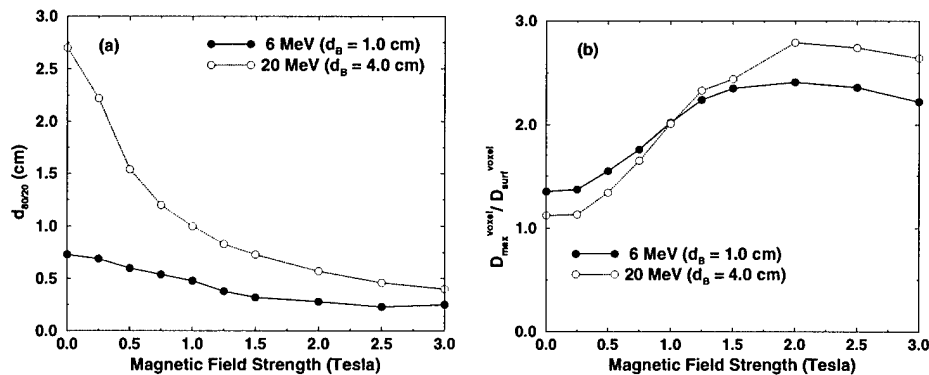


Figure 10. The effects of changing the magnetic field strength was assessed by fixing the field position and incident energy, and observing the effects on two key parameters: (a) the value of $d_{80/20}$ for 6 and 20 MeV at 1.0 and 4.0 cm depth respectively; (b) the ratio of peak to surface dose, SSF, for 6 and 20 MeV at 1.0 and 4.0 cm depth respectively.

irradiation geometries are of limited clinical value. However, this limitation may be overcome using the modified MERT techniques described in section 3.4.

3.3.3. $d_{80/20}$ —dose fall-off. The value of $d_{80/20}$, the width of the 80–20 ‘penumbra’ in the depth direction, is a measure of the ability of the magnetic field to improve the dose drop-off, one of the primary goals of using magnetic fields. It was found that with a 3.0 T magnetic field, $d_{80/20}$ was largely invariant as the depth of the magnetic field was changed, as seen in table 1. The Monte Carlo results show an average $d_{80/20}$ of 2.1 mm at 6 MeV, 2.7 mm at 12 MeV and 3.5 mm at 20 MeV. For comparison, note that without a magnetic field, the $d_{80/20}$ values are 7.3 mm for 6 MeV, 14 mm for 12 MeV and 27 mm for 20 MeV. This indicates a reduction in the drop-off distance of between 71% for 6 MeV to 87% at 20 MeV.

Table 1. Summary of beam parameters for selected electron beams at 1.5 and 3.0 T. Parameters are defined in section 3.3 and are given along the central axis.

Energy (MeV)	\vec{B} -field starting depth (cm)	$\ \vec{B}\ = 1.5 \text{ T}$			$\ \vec{B}\ = 3.0 \text{ T}$		
		$d_{80/80}$ (cm)	$d_{80/20}$ (cm)	SSF	$d_{80/80}$ (cm)	$d_{80/20}$ (cm)	SSF
6	0.0	0.46 [†]	0.32 [†]	1.50 [†]	0.24 [†]	0.17 [†]	1.28 [†]
	1.0	0.49	0.32	2.35	0.32	0.25	2.22
12	1.0	0.84	0.47	2.31	0.53 [†]	0.27 [†]	1.66 [†]
	2.0	0.71	0.51	2.66	0.46	0.27	2.37
	3.0	0.67	0.49	2.25	0.67	0.28	2.62
	4.0	0.93	0.38	1.64	0.73	0.27	2.01
20	1.0	1.66 [†]	0.66 [†]	2.22 [†]	0.91 [†]	0.32 [†]	1.61 [†]
	2.0	1.39	0.72	2.55	0.92 [†]	0.35 [†]	1.74 [†]
	3.0	1.20	0.74	2.71	0.82	0.36	2.12
	4.0	1.06	0.76	2.57	0.76	0.40	2.64
	5.0	0.93	0.72	2.27	0.62	0.37	2.63
	6.0	0.96	0.65	1.88	0.95	0.34	2.19
	7.0	1.19	0.58	1.47	0.84	0.34	1.81
6	None	1.66	0.73	1.35	1.66	0.73	1.35
12	None	4.22	1.40	1.21	4.22	1.40	1.21
20	None	6.96	2.70	1.12	6.96	2.70	1.12

The error on doses (and on all derived values shown above) was in all cases $<1\%$ (1σ) of the maximum dose in the volume.

[†] Lateral disequilibrium. Total energy deposited along central axis with \vec{B} -field differs from the unperturbed case by more than 5%. See discussion in section 3.3.

At 1.5 T, the $d_{80/20}$ for the 6 MeV beam is nearly constant at 3.3 mm. However, as seen in table 1, there is a noticeable peak in the $d_{80/20}$ values for 12 and 20 MeV. The rise in $d_{80/20}$ is due to the increased scattering at lower electron energies. As the magnetic fields are positioned deeper in the phantom, the spectrum of the electrons caught in the magnetic field is shifted towards lower energies and the increased scattering at these energies results in a scattering towards greater depths. However, as the magnetic field moves beyond this peak value (2 cm at 12 MeV and 4 cm at 20 MeV), the energies (~ 8 MeV) are too low for the electrons to escape very far from the magnetically defined track.

In the context of MERT, regardless of how many fields are directed along the same port, the $d_{80/20}$ of the combined field will be the $d_{80/20}$ of the deepest penetrating field, given a minimal contribution from the bremsstrahlung tail. Thus, before any combined fields are simulated, there is an *a priori* expectation that combined fields will preserve the rapid dose fall-off seen with the individual fields.

3.3.4. $R_{p/eff}$ —depth of maximum penetration. The third parameter by which the fields were characterized was the effective practical range. This is similar to the standard dosimetric practical range R_p in that it is defined by the intersection of the zero dose level and a linear extrapolation of the dose fall-off region. Physically, $R_{p/eff}$ represents the maximum penetration of electrons in the medium in the presence of the magnetic field. Thus, the distance $R_{p/eff} - d_B$ represents the distance required by the magnetic field to turn the highest-energy electrons back towards the surface.

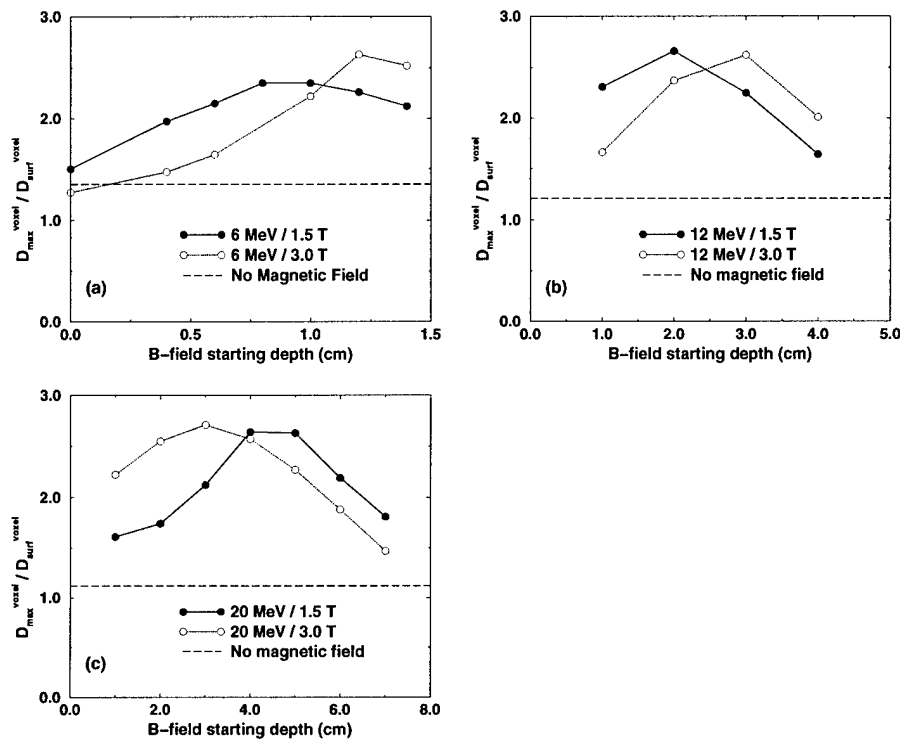


Figure 11. The surface sparing factor (SSF), defined as the ratio ($D_{\text{max}}^{\text{voxel}} / D_{\text{surf}}^{\text{voxel}}$). A higher SSF value suggests lower skin dose for a given target dose. The SSF is shown as a function of magnetic field placement: (a) 6 MeV, (b) 12 MeV, (c) 20 MeV.

As electron energy scales approximately linearly with depth and r_g scales linearly with energy, it follows that the distance between the start of the magnetic field and the effective practical range, $R_{p/\text{eff}} - d_B$, should scale linearly with d_B . Indeed, this was the case as is shown in table 1.

3.3.5. SSF—surface sparing factor. The surface sparing factor is a unitless parameter defined as the ratio of the dose maximum to the dose to a voxel at the surface (i.e. the average dose delivered to the first 2 mm of depth.) However, a high surface sparing factor does not immediately suggest that a high dose may be delivered to a target at several centimetres depth while avoiding a high skin dose. As described above, the dose peak may extend only several millimetres in the depth direction, and would almost certainly not be clinically useful as a single field. Combining fields inevitably leads to a reduced SSF, as will be seen later. Thus it is crucial that the beams that will be used in a magnetic-MERT system exhibit a high starting SSF, before combination with other fields.

As seen in figure 11, at each energy, there is a unique starting depth for the magnetic field that results in a maximal SSF. At 6 MeV, the SSF increases as the magnetic field is moved deeper until a maximum occurs between 0.8 and 0.9 cm at 1.5 T and 1.2 cm at 3.0 T. At 12 MeV, this depth was 1.0 cm at 1.5 T, or 2.0 cm at 3.0 T, and at 20 MeV, this depth was 3 cm at 1.5 T and 4.0 cm at 3.0 T. The existence of a maximal value is related to several factors. The SSF

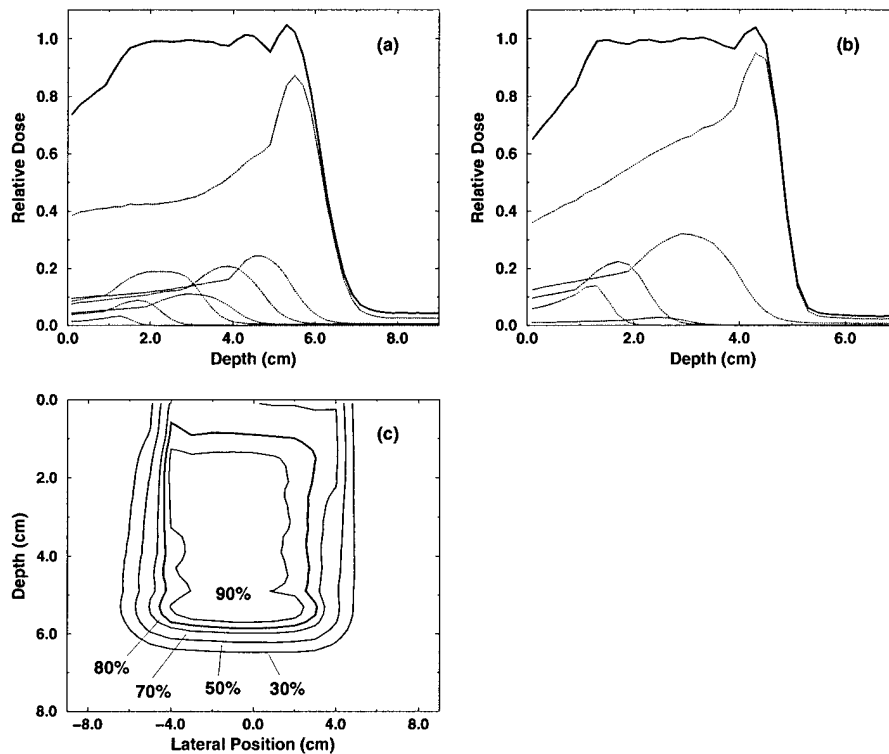


Figure 12. Central-axis depth-dose curves demonstrating how linear combinations of $10 \times 10 \text{ cm}^2$ electron beams in magnetic fields, with different intensities and magnetic field placements, can be used to create homogeneous dose distributions. Note that both the SSF ($D_{\text{max}}^{\text{voxel}}/D_{\text{surf}}^{\text{voxel}}$) and $d_{80/20}$ are significantly improved relative to a field-free situation: (a) 1.5 T only, (b) 1.5 T and 3.0 T, (c) isodose curves for the 1.5 T optimization.

drops dramatically when the magnetic field is introduced at shallower depths, an effect related not so much to the formation of a dose peak as the deposition of energy at the surface. These cases correspond to those which, as discussed earlier, lack electronic equilibrium as electrons exit the beam through the front surface of the phantom. At greater depths, electrons are at a lower energy and so are confined to smaller regions, thus resulting in an increased dose peak. This is offset by the fact that at deeper depths a greater percentage of the energy has already been deposited.

3.4. Combined fields

As seen when examining the depth-dose profiles, the depths at which these magnetically perturbed electron beams are therapeutically useful spans a limited range. Defining a prescription dose of 80% of the dose maximum, the width of the therapeutic region is given by $d_{80/80}$ and can be less than 1 cm, as seen in table 1 and section 3.3.2. Clinical targets are often significantly larger and so a method is required to create wider dose peaks. A similar problem is encountered in proton beam therapy, in which case a system of variable beam attenuation based on a range modulation wheel may be used to create a 'spread-out Bragg peak' of arbitrary

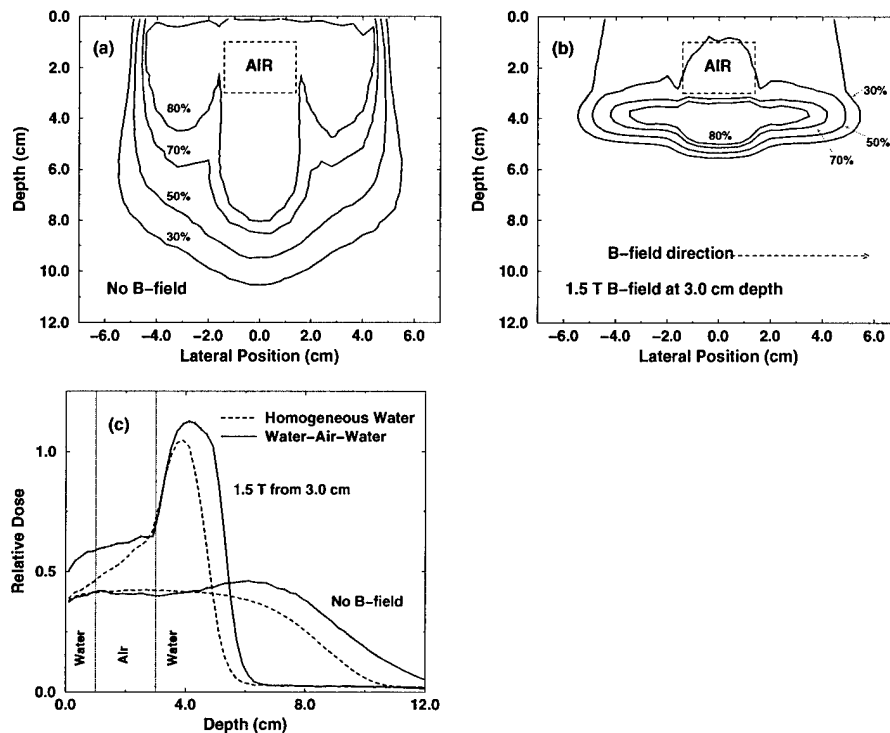


Figure 13. The effect of an air cavity heterogeneities on dose distributions with and without magnetic fields. Note that the heterogeneities do not change the shape of the depth-dose curve significantly when magnetic fields are applied. The direction of electron deflection here is into the page. The heterogeneity extends infinitely into and out of the page. (a) Isodose curves without magnetic field, (b) with 1.5 T magnetic field from 3 cm (directly after the air cavity), (c) corresponding central-axis depth-dose curves. The vertical axis represents absolute dose in arbitrary units.

width. However, for electron beams, any material in the beam path would significantly distort the field shape by causing additional scattering and also risk the production of bremsstrahlung photons in the case of high-Z materials. However, the general principle of beam modulation remains valid, and suggests the use of modulated electron radiation therapy.

Previous discussions of MERT have considered the use of fields with non-uniform energies and intensity distributions. Here, the technique is extended to the use of multiple magnetic field positions, i.e. a single port may include a 20 MeV field with a magnetic field beginning at 3.0 cm depth for a certain number of monitor units, and then another 20 MeV field with the magnetic field located at a depth of 5.0 cm delivered down the same axis, etc. It is instructive to compare this methodology with the more familiar method used in proton beam therapy. In that system, physical blocks of different thicknesses are used to shift the Bragg peak to different depths, and intensity modulation is provided by allowing the beam to dwell on a given modulator for a variable time period. In this case, the only difference is the means of moving the pseudo-Bragg peak, that is, by moving the magnetic field. Beam intensity is modulated simply by changing the number of monitor units delivered with the magnetic field at a given position. It was believed that, as with the proton beam, useful fields can be constructed while maintaining the desirable depth-dose drop-off and low skin dose.

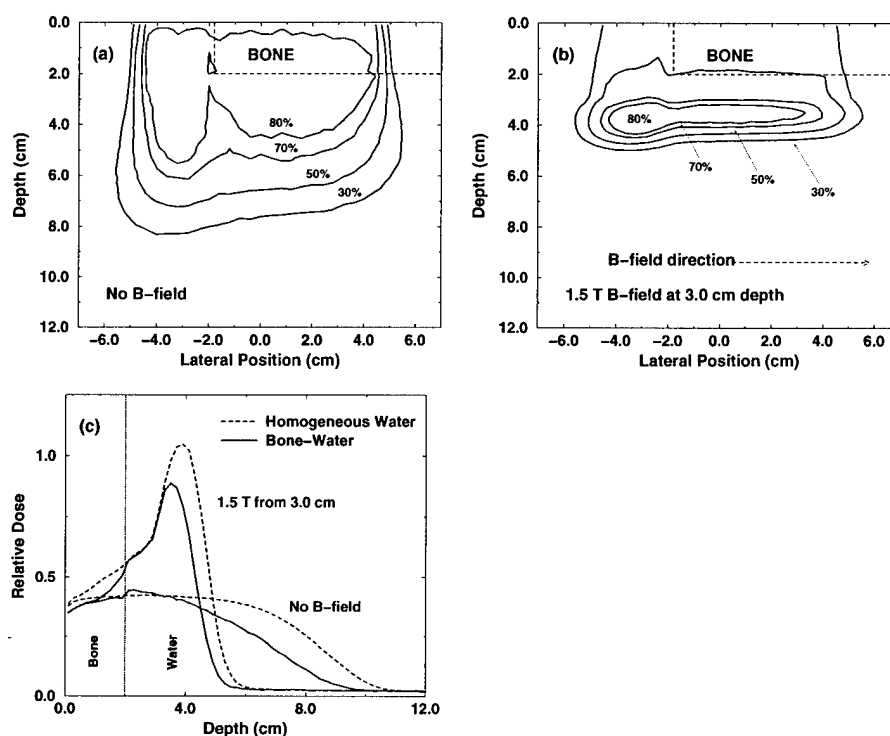


Figure 14. The effect of a bone heterogeneity on dose distributions with and without magnetic fields. The direction of electron deflection here is into the page. The heterogeneity extends infinitely into and out of the page. (a) Isodose curves without magnetic field, (b) with 1.5 T magnetic field from 3 cm, (c) corresponding central-axis depth-dose curves. The vertical axis represents relative dose.

A simple one-dimensional optimization routine was utilized to generate two fields. In one case, a target profile was generated where the dose would rise linearly from 50% at the surface (relative to the maximum along the profiled axis) to 100% at 1.0 cm, then drop to zero at 6.2 cm. The optimized solution was solved numerically, and a linear combination of the 1.5 T fields was generated to match the target values in a least-squares sense. The results are shown in figure 12(a). Using the terminology from section 3.3, the width of the treatment region, $d_{80/80}$, was found to be 5.0 cm, followed by a $d_{80/20}$ drop-off of 0.77 cm. Between the depths of 1.6 cm and 5.6 cm, the dose was homogeneous to within $\pm 5.4\%$ of the average dose. The corresponding isodose curves for this situation are shown in figure 12(c).

A second target profile was also constructed, again rising linearly from 50% at the surface to 100% at 1.0 cm, but then falling to zero dose at a depth of 4.8 cm. In this case, both 1.5 T and 3.0 T magnetic fields were permitted. The results are shown in figure 12(b), with a $d_{80/80}$ of 3.7 cm and a $d_{80/20}$ of 0.43 cm. Between 1.2 cm and 4.6 cm depth, the dose was homogeneous to within $\pm 4.5\%$ of the average dose.

It is noted that to achieve the same target coverage as in figure 12(a) without magnetic fields, a 20 MeV beam would have to be used. Recall that the $d_{80/20}$ for a single 20 MeV beam with a magnetic field is 2.7 cm, or 250% of the $d_{80/20}$ for the 1.5 T field case. Additionally, the surface dose would be higher by approximately 10% of the dose maximum. Similarly,

for figure 12(b), a 12 MeV beam would be used, with a $d_{80/20}$ of nearly 10 times that of the magnetic field case, with a significantly higher surface dose as well. MERT techniques may improve the dose homogeneity within the target region, but cannot improve the depth-dose fall-off.

The small dose inhomogeneities, in particular small peaks near the end of the treatment field, are caused by the limited dataset. The optimization was restricted to setting the magnetic field at the fixed depths used in this study. A full-scale optimization routine would allow the standard non-uniform intensities, in addition to computing optimal magnetic field placements for each segment, with the ability to choose the field placement along a continuum or among a closely spaced set of discrete depths.

Certainly, a real magnetic field/beam profile optimization would have to occur at a minimum in \mathbb{R}^2 , thus accounting for the lateral shift seen in figure 5(a). In an engineering sense, reversing the magnetic field direction is likely to be trivial, and this possibility must also be accounted for. The mathematical and physical nature of this optimization scheme is beyond the scope of this work, but further discussion of practical issues involved in optimization and treatment planning is presented in section 3.6.2.

3.5. Inhomogeneities

The presence of shallow heterogeneities located between the surface and the magnetic field was also investigated. Slabs of bone and air cavities were simulated by replacing the water of some of the voxels with air or ICRP standard bone. The goal was to observe the effect of the changes in electron energy spectra caused by passage through heterogeneous media on the parameters discussed in section 3.3.

The isodose curves with an air cavity, both with and without magnetic fields, are shown in figures 13(a) and 13(b). The corresponding depth-dose curves are shown in figure 13(c). The results of the simulations with a 3 cm slab of bone at the surface are shown in figure 14.

Note that the goal of these simulations differs from previous experimental work, such as that of Paliwal *et al* (1978). In that work, the authors used a magnetic field gradient such that the dose distribution with the inhomogeneity did not differ significantly from the dose distribution without the inhomogeneity. Here, the dose distributions differ radically between the heterogeneous media with the magnetic field and the homogeneous media with no field. Instead, the primary point of interest is that the general *form* of the depth-dose distributions is preserved; that is, a dose peak followed by a sharp dose drop-off with a favourable SSF. Given this, then even in the presence of inhomogeneities treatment fields can be constructed by using the modulation techniques described earlier.

As shown in figure 13(c), with an air cavity present, there is a trivial (1 mm) decrease in the $d_{80/20}$ and a decrease in the SSF from 2.7 to 2.2. With a bone slab, there was no change in $d_{80/20}$ and a drop in SSF from 2.7 to 2.5. Thus, even if the beam passes through inhomogeneities before entering the magnetic field, the advantages of magnetic fields are still preserved. Certainly, with an inhomogeneity present, additional fields may be necessary to cover the entire target region. However, it has been shown elsewhere (Ma *et al* 2000b) that the non-uniform intensity profiles used in MERT can provide highly conformal coverage of a target in the presence of heterogeneities. Based on these results, it is concluded that MERT combined with the techniques shown in the previous section, will exhibit the conformal coverage of MERT with the added ability to reduce surface dose and dose to distal structures, even in inhomogeneous media.

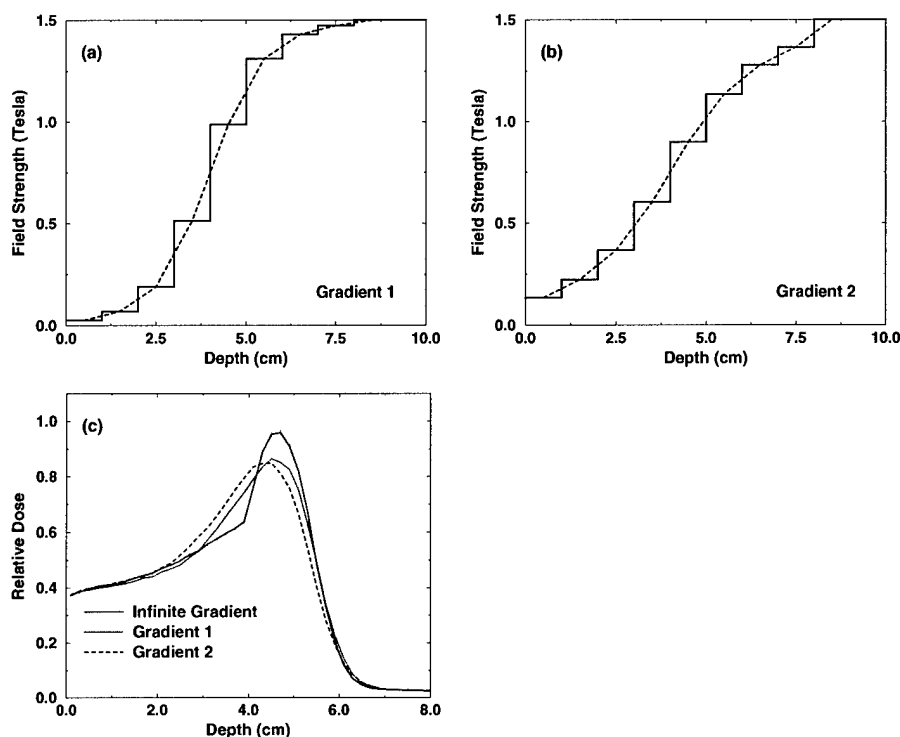


Figure 15. The effect of finite magnetic field gradients on central-axis depth-dose curves. Gradients are displayed as magnetic field strength as a function of depth: (a) gradient 1, (b) gradient 2. (c) The corresponding depth-dose curves with the infinite gradient included for comparison. The vertical axis represents relative dose.

3.6. Practical considerations

3.6.1. Field gradients. For the simulations described thus far, the structure of the magnetic fields have been taken to be a step function, i.e. the field gradient is infinite. However, this cannot be the case in any real system. Similarly, the field strength outside the primary region is typically non-zero, as low-strength fringe fields will inevitably fill the remaining space. Nardi and Barnea (1999) demonstrated that for a 15 MeV monoenergetic beam in a 3.0 T field, the difference between the infinite and finite gradient ($d\|\vec{B}\|/dz \approx 1.25 \text{ T cm}^{-1}$) was not significant. The difference in $d_{80/80}$ was 1 mm while the SSF dropped from 2.43 to 2.27. As demonstrated above, $d_{80/80}$ can be made largely irrelevant by combining fields. Thus, this section focuses on the effects of finite gradients on $d_{80/20}$ and SSF.

To explore the effects of finite gradients and fringe fields, two magnetic fields were constructed with gradients shown in figures 15(a) and 15(b). Considering the semilinear region centred around 4 cm, gradient 1 rises with $d\|\vec{B}\|/dz \approx 0.4 \text{ T cm}^{-1}$ while gradient 2 rises at $\sim 0.2 \text{ T cm}^{-1}$. The resulting central axis dose profiles are shown in figure 15(c), compared with the 20 MeV 4 cm field case (4 cm corresponds to the 50% field level in the gradients.) It can be seen that the $d_{80/20}$ drop-off increases by less than 0.5 mm with gradient 1 (the steeper gradient), and less than 1.5 mm with gradient 2. While this is considered to be an adverse effect, these $d_{80/20}$ values still represent 70.3% and 67.0% improvements over

the zero-field case. The peak dose value was also seen to be diminished while surface dose remained relatively constant. The SSF when the field was defined by a step function was 2.57. With gradient 1 this was reduced to 2.31, and with gradient 2 it was reduced to 2.26. Again, this is undesirable, but the SSF is still more than twice that of the 20 MeV zero-field system.

Thus, it is concluded that while sharper gradients are clearly superior to slower gradients, even an unrealistically 'poor' field of only 0.2 T cm^{-1} still presents significant advantages over the zero-field case.

3.6.2. Other considerations. It is clear that the largest hurdles in the implementation of magnetic fields are not theoretical issues, but rather are of a much more practical nature. In particular, the effect of fringe fields on the electronic equipment of the accelerator and the stability of the electron beam as it travels through the treatment head. This must be investigated thoroughly before any clinical implementation can occur.

Additionally, the use of magnetic fields at multiple depths for different segments of an intensity modulated field requires high-precision computer control. It is feasible that linking the electron-specific MLC to be used in MERT (Lee *et al* 2000a, b) and a magnetic field system to the same controller will allow such delivery to occur. Thus, for example, a single 'step' of a step-and-shoot type algorithm may represent the motion of the leaves to a new pattern as well as motion of the magnetic field to a new position. This would of course necessitate significant changes in the entire treatment planning system. For example, a beamlet-based beam profile optimization routine must have precalculated beamlets not only for different energies, but different field positions (see section 3.4). The leaf sequence algorithm must be extended to also compute the necessary movement of the magnetic field. As has been shown elsewhere (Lee *et al* 2000c), the background dose can rise significantly if too many field segments are used, so the treatment planning system must balance the background dose with trying to achieve maximum conformity. Finally, the issue of magnetic field verification is created, which does not lend itself to as straightforward a solution as leaf sequence verification.

A simplification of the system could conceivably utilize magnetic fields simply as a way of restricting dose to an organ at risk. For example, in an anterior-posterior directed MERT-based breast treatment (Ma *et al* 2000b), the magnetic field could be aligned along the base of the chest wall. This will not improve homogeneity in the breast or reduce skin dose, but will restrict dose to the lung. The advantages of this would have to be compared with the potential dose boost to the distal end of the target structures.

4. Conclusion

It has been demonstrated that transverse magnetic fields can be used effectively to create dose distributions with sharp depth-dose fall-offs and a favourable ratio of peak-to-surface dose. The depth-dose distribution from such a field was qualitatively observed to resemble the Bragg peak seen in proton therapy. The position and size of this peak varied as function of electron energy, field strength and field position. Generally, this peak exhibited only a very narrow therapeutic range, and so a method of broadening this peak was necessary. It was demonstrated that a modified form of MERT could be employed to generate a clinically useful field. The energy and intensity of the electron beam, as well as the position of the magnetic field were varied, thus creating a homogeneous dose distribution several centimetres in depth, while retaining the desired dose fall-off and low surface dose. This could be accomplished with constant magnetic field strength or variable field strength. It was further shown that the primary effect of heterogeneities is to shift the position of the dose peak, but to have minimal effect on the dose

fall-off distance. The effect of magnetic field gradients was seen to adversely affect the drop-off and surface sparing, but only moderately. Nonetheless, it is clear that the sharper gradients are preferred. With recent improvements in the development of compact high-strength magnetic fields, higher- T_c superconductors, the development of variance reduction techniques and rapid Monte Carlo electron dose calculation systems and faster computer systems, it is anticipated that the use of magnetic fields will rapidly become practically feasible. Thus it is concluded that when combined with the emerging modality of MERT, magnetic fields allow significant improvements in dose conformity in the depth direction.

Acknowledgments

We would like to thank our colleagues at Stanford for helpful comments and discussion on this work: Art Boyer, Gary Luxton, Steve Jiang, Todd Pawlicki, Jinsheng Li and Jun Deng. Algorithms for transport in a magnetic field were adapted from Alex Bielajew (University of Michigan) as included in the standard EGS4 distribution. This work was supported in part by grants BC971292 from the US Department of Defense, CA78331 from the NIH, and NIH training grant 5T32GM08294-11.

References

- Bielajew A F 1987 Electron transport in \vec{E} and \vec{B} fields *Monte Carlo Transport of Electrons and Photons* ed T E Jenkins *et al* (New York: Plenum) pp 421–34
- 1993 The effect of strong longitudinal magnetic fields on dose deposition from electron and photon beams *Med. Phys.* **20** 1171–9
- Bielajew A F and Rogers D W O 1987 PRESTA—the parameter reduced electron step algorithm for electron Monte Carlo transport *Nucl. Instrum. Methods B* **18** 165–81
- Jiang S B, Kapur A and Ma C-M 2000 Electron beam modelling and commissioning for Monte Carlo treatment planning *Med. Phys.* **27** 180–91
- Kapur A, Ma C-M, Mok E C, Findley D O and Boyer A L 1998 Monte Carlo calculations of electron beam output factors for a medical linear accelerator *Phys. Med. Biol.* **43** 3479–94
- Lawson C L and Hanson R J 1974 *Solving Least Squares Problems* (Englewood Cliffs, NJ: Prentice-Hall)
- Lee M C, Jiang S B and Ma C-M 2000a Monte Carlo and experimental investigations of multileaf collimated electron beams for modulated electron radiotherapy *Med. Phys.* **27** accepted
- Lee M C, Jiang S B, Yi B and Ma C-M 2000b Monte Carlo simulations of multileaf collimated electrons *Proc. 13th Int. Conf. on the Use of Computers in Radiation Therapy* ed W Schlegel and T Bortfeld (Heidelberg: Springer) pp 126–8
- Lee M C, Kapur A, Jiang S B and Ma C-M 2000c Characterization of electron beams for modulated electron beam radiotherapy *Proc. World Congress on Medical Physics and Biomedical Engineering (23–28 July, 2000)* (CD-ROM)
- Ma C-M, Li J S, Pawlicki T, Jiang S B and Deng J 2000a MCDOSE—a Monte Carlo dose calculation tool for radiation therapy treatment planning *Proc. 13th Int. Conf. on the Use of Computers in Radiation Therapy* ed W Schlegel and T Bortfeld (Heidelberg: Springer) pp 123–5
- Ma C-M, Pawlicki T, Lee M C, Jiang S B, Li J, Deng J, Yi B, Mok E, Luxton G and Boyer A L 2000b Energy- and intensity-modulated electron beams for radiotherapy *Phys. Med. Biol.* **45** 2293–311
- Ma C-M and Rogers D W O 1997 BEAMDP users manual *National Research Council of Canada Report PIRS-0509c* (Ottawa: NRC)
- McGowan H C E, Faddegon B A and Ma C-M 1996 STATDOSE for 3D distributions *National Research Council of Canada Report PIRS-0509f* (Ottawa: NRC)
- Nardi E and Barnea G 1999 Electron beam therapy with transverse magnetic fields *Med. Phys.* **26** 967–73
- Nath R and Schulz R J 1978 Modification of electron-beam dose distribution by transverse magnetic fields *Med. Phys.* **5** 226–30
- Nelson W R, Hirayama H and Rogers D W O 1985 The EGS4 code system *SLAC Report 265* (Stanford, CA: Stanford Linear Accelerator Center)

- Paliwal B R, Wiley A L, Wessels B W and Choi M C 1978 Magnetic field modification of electron-beam dose distributions in inhomogeneous media *Med. Phys.* **5** 404-8
- Rogers D W O, Faddegon B A, Ding G X and Ma C-M 1995 BEAM: a Monte Carlo code to simulate radiotherapy treatment units *Med. Phys.* **22** 503-24
- Sempert M 1960 New developments in high-energy electron beam therapy with the 35 MeV Brown Boveri betatron *Radiology* **74** 105-7
- Shih C C 1975 High energy electron radiotherapy in a magnetic field *Med. Phys.* **2** 9-13
- Weinhous M S, Nath R and Schulz R J 1985 Enhancement of electron beam dose distributions by longitudinal magnetic fields: Monte Carlo simulations and magnet system optimization *Med. Phys.* **12** 598-603
- Whitmire D P, Bernard D L, Peterson M D and Purdy J A 1977 Magnetic enhancement of electron-dose distribution in a phantom *Med. Phys.* **4** 127-31
- 1978 Magnetic enhancement of electron-dose distribution in tissue and lung phantoms *Med. Phys.* **5** 409-17